Universidad de Sevilla
Escuela Técnica Superior de Ingeniería

Experimental and Numerical Studies on Microfluidic Systems

A dissertation presented by
Ahmed Said Mohamed Ismail,
to Department of Aerospace Engineering and Fluid Mechanics
in fulfillment of the requirements for the degree of
Doctor of Philosophy
in the subject of Mechanical Engineering and Industrial Organization.

supervised by
Dr. Miguel A. Herrada Gutiérrez
and
Dr. J.M. López-Herrera Sánchez

Sevilla, April 2016.

Universidad de Sevilla
Escuela Técnica Superior de Ingeniería

Experimental and Numerical Studies on Microfluidic Systems

Memoria realizada por
Ahmed Said Mohamed Ismail,
presentada ante el Departamento de Ingeniería Aerospacial y Mecánica de Fluidos de la Universidad de Sevilla
para optar al grado de Doctor de filosofía en Ingeniería Mecánica y de Organización Industrial.

Dirigida por
Dr. Miguel A. Herrada Gutiérrez
y
Dr. J.M. López-Herrera Sánchez

Sevilla, Abril 2016.

Acknowledgements

I would like to express my sincere gratitude to my advisors: Dr. Miguel A. Herrada Gutiérrez and Dr.J.M. López-Herrera Sánchez for the continuous support of my Ph.D study and related research, for their patience, motivation, immense knowledge and for being there every time I knock their door during these past four years. Also to my tutor Dr. Alfonso M. Gañán Calvo for giving me the opportunity to be part of his research group, for his guidance, and for many insightful discussions. I learned a lot from them and I hope that our collaboration continue in the future.

My sincere thanks also goes to Dr. Joan Rosell-Llompart, and Dr. Alfonso Castrejón-Pita, who provided me with the opportunity to join their team as intern, and who gave access to the laboratory and research facilities at Universidad Rovira i Virgili and University of Oxford. Without they precious support it would not have been possible to conduct this research.

Also, thanks to the Ministry of Economy and Competitiveness of Spain for making this study possible by providing the financial support.

My gratitude also goes to my fellow labmates: Luis, Paco and Irene for sharing thoughts and for having interesting discussions. I thank also Beatriz and Dory for their help in solving Administrative problems.

My thanks goes also to my family: my brother and my sisters and especially to my parents for being such a big source of supporting and encouragement without both of you I couldn't be here. Finally, thanks to my beloved wife for supporting me spiritually.

Abstract

The work presented in this thesis can be summarized as a compilation of five different and comprehensive studies in the field of microfluidic flows, related to the formation of jets, drops and bubbles; where the surface tension plays a major role. The topics studied are classified in chapters where the problem formulation, procedures, and results are individually presented.

Chapter 2 is devoted to understand the evolution of Newtonian capillary jets and to study the instability transition of viscoelastic jets under axisymmetric perturbations. A mathematical model has been used to determine the parameter conditions for which the convective to absolute instability transition takes place, playing special attention to the role played by unrelaxed elastic axial stress. Chapter 3 presents results of a numerical study of rivulets in microchannels in order to characterize stable and unstable regimes. The theoretical frame work and stability analysis are presented in detail. It was found that a basic flow can become unstable when that quantity exceeds a certain critical value, while the rest of governing parameters remain constant. Chapter 4 discuses a ubiquitous process in science and technology - the dissolution of microbubbles. As in the previous chapters, detailed theoretical and numerical approaches are developed from scratch, culminating in a set of carefully performed experiments. Numerical and experimental results agree well and complement each other.

We move then onto Chapter 5 which studies the electrical disruption of pendant liquid drops. The focus of the study here is the behaviour of suddenly electrified pendant droplets in dielectric liquid. Supported by numerical and experimental results, we argue that the viscosity of the surrounding fluid is responsible for the development of more complex jetting processes such as what is called splashing in which the tip of the cone explodes onto a mushroom-like structure, and splitting regimes. Moreover, when the cone evolves into one of these modes they do it in a way that is dependent on the large scale properties such as the initial droplet size and on the applied voltage - contrary to the well-established (universal) mechanisms encountered in the tip streaming mode. Finally, Chapter 6 presents a series of one-to-one numerical and experimental runs with excellent agreement of a novel way of producing drops that are significantly smaller than the nozzle from which they

emerge. A very detailed discussion of the experimental rig is presented, including the important parameters to be taken in account, such as the meniscus formed at the nozzle and the deformation of the nozzle plate during the driving pressure pulses. Finally, a predictive scaling law of the produced droplet size was obtained.

Contents

Chapter 1

Introduction

Any review of the literature on the microfluidic systems related to capillary jets, droplets and bubbles will reveal in short their interest and relevance. For instance, a recent quick search in the SCOPUS database has returned 39605 items when the word searched is "microfluidic". If this search is combined with "jet", "droplet" or "bubble" the figures of found items is still enormous; 1568, 8132 and 3253, respectively. These large figures are just a reflect of the great importance in many technological applications of such systems.

Capillary jets can be found in an enormous variety of processes of interest in very diverse fields, such as pharmacy, biotechnology, industrial and chemical engineering, or the food and agriculture industry. Typically in these fields the objective is to use the capillary threads as a mid-stage step on the production of solid fibers. A variety of physico-chemistry processes can be used to solidify the produced liquid threads before their breakup. In this way, that sub-millimeter artificial fibers for the textile industry can be obtained[1]. Note that the world production of textile fibers alone has increased from about 24 million metric tons in 1975 to nearly 90 million tons in

2014, and the percentage of artificial fibers rose from around 50% in 1975 to nearly 75% in 2014.

Formation of drops is involved in many applications as for example, DNA arraying, the printing of electronics and biomaterials, drug delivery, inkjet printing, automatic pipetting of fluids and manufacture of particles. While, microbubbles are used in drug delivery, biofilm removal and membrane cleaning, also they are used as a contrast medium in images in medical diagnostics.

In this thesis, experimental and numerical studies have been carried out in order to investigate diverse aspects of jets, drops and bubbles in micro/nano scale. Since these fields are too broad, we have limited the aim of the present thesis to,

1. The study of viscoelastic jets. In particular we will perform the spatiotemporal stability of viscoelastic jets subject to unrelaxed axial stress.

2. The study of the capillary instability of rivulets in order to control the production of fibers and microdroplets/microbubbles, respectively, by performing stability analysis of base (zeroth) solutions.

3. The study of the dissolution of gaseous bubbles ascending through a liquid media. The analysis is either numerical and experimental.

4. The study of the liquid-liquid electrical dispersion problem. This issue was also studied experimentally and numerically.

5. The study of "drop on demand" generator based in a novel collapsing technique.

Note that the first item could be categorized as related to capillary jets while the rest falls in the generic field of droplet systems except item three which is related to

bubble systems. Our general goal in these studies is to identify all governing parameters in order to gain a full control of the systems. This can only be gotten by the complete comprehension of the physics behind the diverse systems. In what follows in this introductory chapter, we will expose briefly the most remarking aspects of state-of-art of these micofluidic systems.

1.1 Production and dissolution of microbubbles

Many different techniques have been proposed for the production of microbubbles. One of these techniques is the injection of gas through a micronozzle in a bath of liquid (see fig.1.1 (a)) [2]. The pore size of the nozzle affects on the size of the bubble but another factor has more significant effect on the bubble's size which is the ratio of the surface energy of the nozzle to the surface tension of the liquid. Higher surface energy means that smaller bubble could be produced. If the gas is injected in a liquid stream parallel to the nozzle, this is called Co-flowing system (see fig.1.1 (b)) [3]. Another technique is the flow focusing, in this technique the pinching between the gas and the liquid streams occurs after an orifice located in front of the needle gas. Two configurations are used. Axisymmetric configuration illustrated in Fig.1.1 (c) and planar configuration illustrated in Fig.1.1 (d). The axisymmetric configuration has been proposed by Alfonso Gañan et al [4]. In this work, derived scaling laws are providing the bubble size. The scaling comes from a balance between the local time derivative and convection terms of the inviscid Navier-Stokes equations [5]. The planar configuration was introduced by Garstecki et al [6]. Both configurations cover different ranges of Reynolds numbers and they can work on the Stokes and inertial regimes, respectively. Fig.1.1 (e) shows the

T-junction geometry which could be considered the most popular configuration to produce microbubbles. It was presented as a microfluidic device by Thorsen et al [7] to generate emulsions, then Gunther et al [8] used it to produce microbubbles. In this technique a stream of gas is introduced into a stream of liquid by using T-junction, the pinching happens due to the large stresses on the interface between the two streams. Recently, the role of swirl to generate small mono-disperse bubbles has been investigated. A 3D simulation model of an axisymetric T-junction showed that the size of the bubbles are smaller than bubbles produced in the absence of swirl [9]. A variation of the T-junction technique has been proposed by M. A. Herrada et al (see Fig.1.1 (f)) [10]. In the new technique, a gas stream is injected into a liquid stream moving in a channel through T-junction, the gas adheres to a strip of hydrophobic material posted on the bottom surface of the channel forming a rivulet. This rivulet breaks up into monodisperse microbubbles due to a capillary instability developed at the rivulet. This technique could also be used to produce microdroplets by posting a hydrophilic material strip rather than the hydrophobic one. En chapter 3 a numerical analysis was realized to get a deeper insight on the capillary instability of rivulet in order to control the production of microbubbles or microdroplets by using Herrada's T-junction.

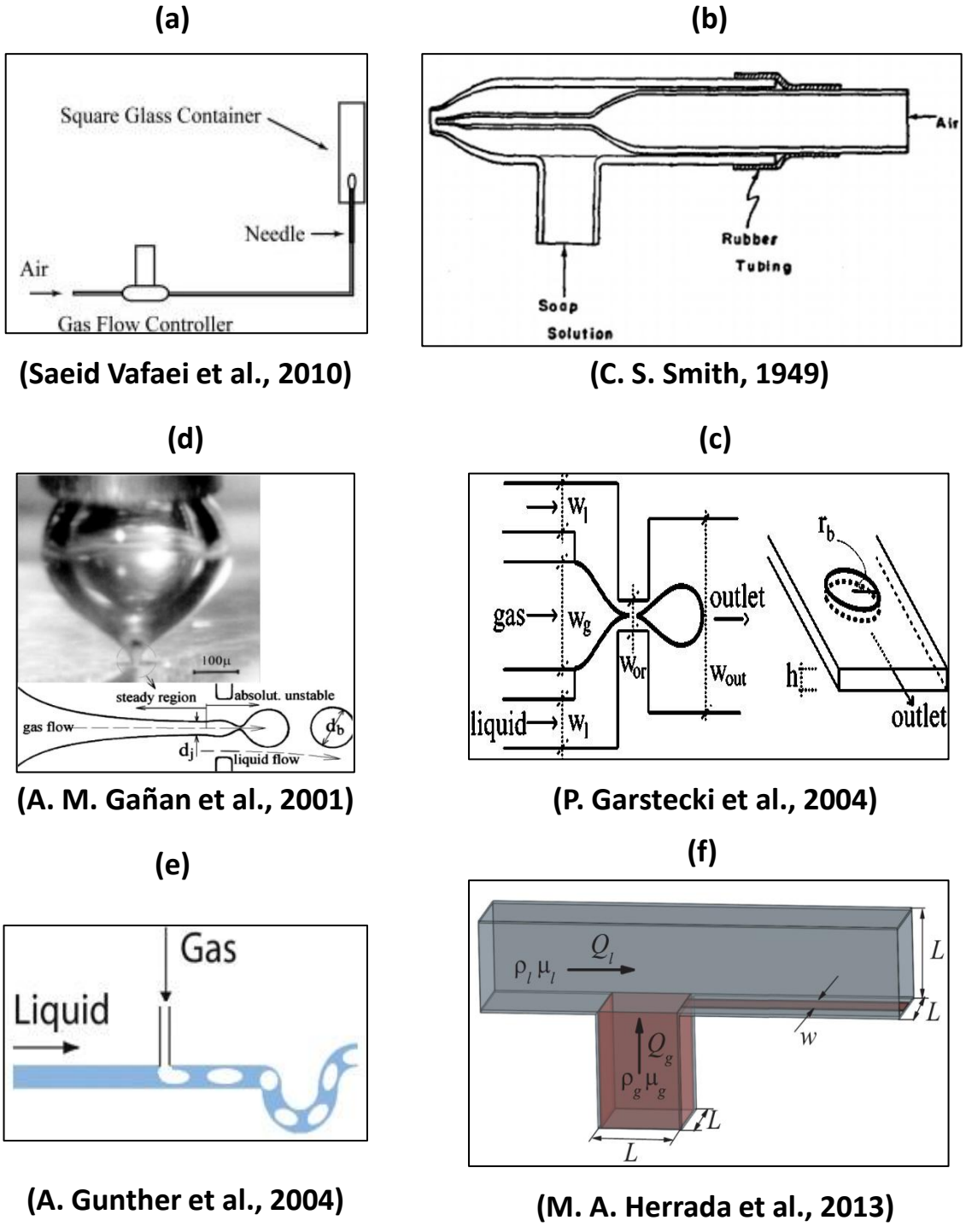

Figure 1.1: Methods to produce microbubbles.

The evolution of gas bubbles in a liquid under buoyancy forces is a multifaceted multi-phase problem: it does not only involve the obvious fluid mechanical phenomena that can be mapped by the associated Reynolds and Weber numbers[11, 12, 13], size distribution, and number concentration[14], but also comprises the complex kinetics around the exchange of gases and vapors between the liquid and the bubble, and the heterogeneous distributions of such constituents in both liquid and gas domains[15, 16, 17, 18]. There is a set of quite generic applications where gas exchange is, among the many different aspects that one may entertain in the problem of rising bubbles, the principal target factor to score performance. For example, in the petroleum industry, the number of wells demanding gas injection for oil recovery is soaring[19]. In this case, the high pressures and extreme conditions inside the well or oil bed promotes gas dissolution even at very low diffusivities[20]. On the other hand, CO_2 sequestration by injection in water reservoirs (excluding deep submarine injection in liquid phase), or the aeration of tanks or lakes demands a careful choice of bubble size as a function of injection depth to achieve optimal performance (total gas dissolution before the gas reaches the liquid surface)[21]. The same demand applies to micro algae cultivation tanks or bioreactors. To assess the dissolution process in realistic conditions, the Rising Bubble Apparatus (RBA) is a customary instrument[22, 20]. In this device, used to measure what is called the minimum miscibility pressure, the evolution of the gas bubble is monitored by a video camera fixed to a rail parallel to the path of the rising bubble. The work in chapter 4 is motivated by the problem of gas injection into an aqueous environment (waste water, bioreactors, aquaculture, etc.) in the form of small bubbles.

1.2 Production of microdroplets

There are many techniques to produce microdroplets. The methods to produce microdroplets from large diameter could be grouped in two main categories according to the energy source: hydrodynamic jetting and electrohydrodynamic jetting.

1.2.1 Hydrodynamic jetting

One of the hydrodynamic jetting methods is the flow focusing (FF) which is not used only to produce microbubbles but also to produce microdroplets. The formation of microdroplets could be done in FF technique by introducing the liquid from the internal tube and the gas from the external one. Figure 1.2 shows the flow pattern in FF. The energy source is the pressure drop applied to the flow focusing gas, which draw a liquid jet much more smaller than the orifice size. The jet's behavior is characterized by the dimensionless Weber, Reynolds and Capillary numbers which are defined as follow:

$$We = \rho Q^2/\pi^2 R^3 \sigma, \tag{1.1}$$

$$Re = \rho Q/\pi R \mu, \tag{1.2}$$

$$Ca = We/Re, \tag{1.3}$$

being ρ is the liquid density, Q is the liquid flow rate, R is jet's radius, μ is the dynamic viscosity, and σ is the surface tension. The jet separates downstream to monodisperse droplets due to Rayleigh instability.

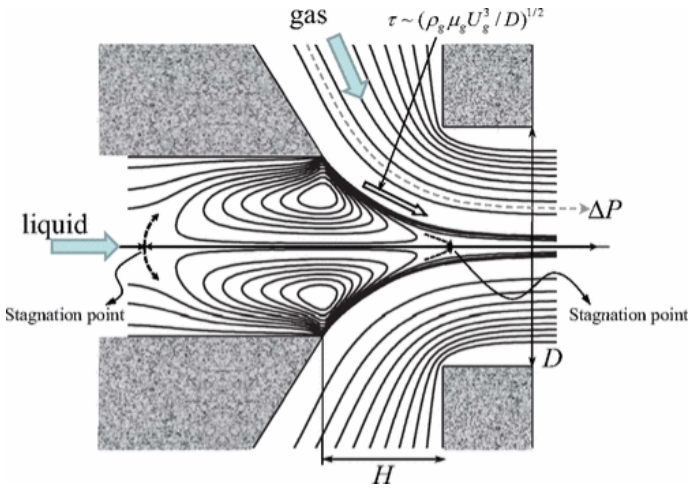

Figure 1.2: Flow pattern in FF technique (Alfonso M. Gañán-Calvo, 2009).

Another hydrodynamic jetting method called flow blurring (FB) has been been developed by Alfonso gañan [23]. The configuration of FB is very similar to FF. The only difference is the value of $\psi = H/D$ (see fig. 1.3 (a)). At $\psi > 0.25$, the liquid flow follows the FF pattern, but if $\psi < 0.25$ a back-flow pattern leads to small-scale perturbation (see fig. 1.3 (b)). The gas flow turns to be radial and perpendicular to the symmetry axis. Due to the circulation of the flow at the feed tube, a stagnation point is created between the feed mouth and the exit orifice. Accordingly, very small jets are produced at the tube exit, which breaks to polydisperse droplets. The final droplet diameter distribution is governed by the dimensionless numbers ψ, We_D, Oh_D, and GLR which are defined as follow:

$$We_D = \rho_g U_g^2 D/2\sigma, \tag{1.4}$$

$$Oh_D = \mu/(\rho_l \sigma D)^{1/2}, \tag{1.5}$$

$$GLR = m_g/m_l, \tag{1.6}$$

being $\rho_g, \rho_l, U_g, D, m_g$, and m_l are gas density, liquid density, gas velocity, nozzle diameter, mass flow rate of gas, and mass flow rate of liquid respectively.

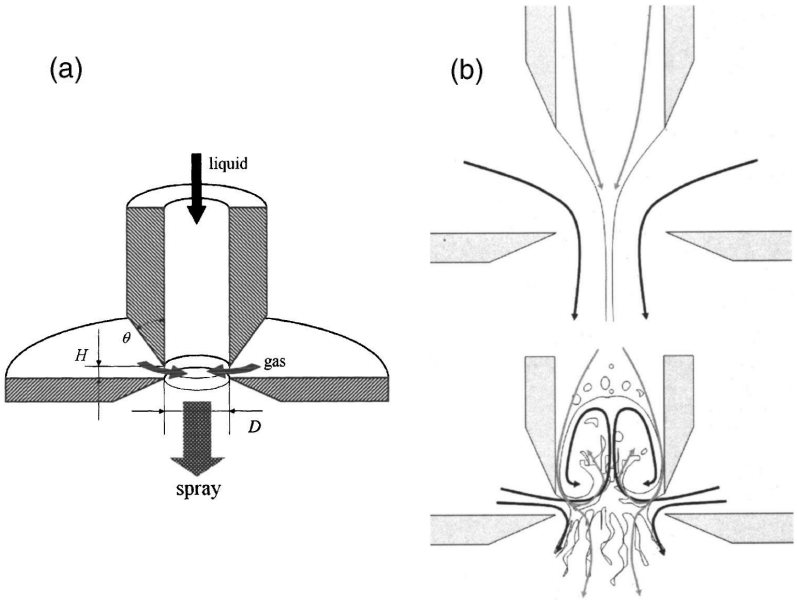

Figure 1.3: Configuration difference between FF an FB (Gañán-Calvo, 2005).

1.2.2 Electrohydrodynamic jetting

One important method to produce very small and monodisperse droplets is the cone-jet electrospraying (ES) which is known also as Taylor's cone [24, 25]. The idea of this method is to apply an electric field to liquid meniscus. Then charges accumulates on the interface producing Maxwell stresses which is proportional to the permittivity of vacuum. The meniscus stretches and forms a conical shape when a balance occur between pressure drop across the interface, the surface tension and Maxwell

stresses. Subsequently, a microjet is emitted from its tip for a voltage difference above the critical (see fig 1.4 (a)). The microjet breaks up downstream producing the droplets. Voltage difference is the energy source in ES which is analog to pressure drop in FF. In electrohydrodynamic jetting, another dimensionless numbers appear, which are electric Bond number, relative permittivity, and dimensionless electrical conductivity as:

$$B_e = \varepsilon_i E^2 R/\sigma, \tag{1.7}$$

$$\beta = \varepsilon_i/\varepsilon_o, \tag{1.8}$$

$$K_d = K(\rho R^3/\sigma\varepsilon_o^2)^{1/2}, \tag{1.9}$$

being K and ε_i are conductivity and permittivity of liquid, E is the electric field, and ε_o is the permittivity of the ambient.

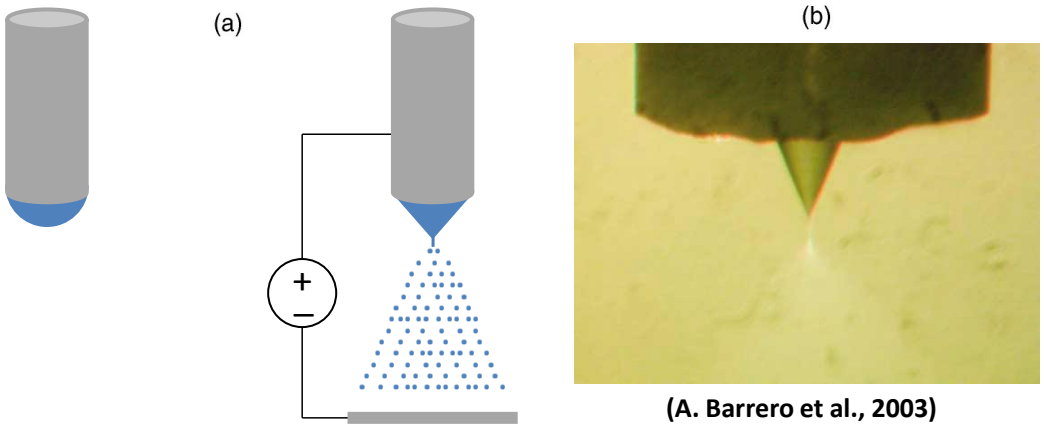

Figure 1.4: (a) Electospraying in air ambient, (b)Electrospraying in liquid ambient.

The droplets produced are charged so, electrospraying has been applied widely in mass spectrometry of large biomolecules. Electrohydrodynamic jetting is not only useful to spray liquids in gas ambient but also into another liquid (see fig 1.4 (b)). Liquid-Liquid dispersion is an essential step in many industrial processes nowadays. It is part, for example, of applications like the encapsulation of drugs or food additives or the obtention of micro(nanometric)-range emulsions. Electrical forces have been proven as an efficient dispersion mechanism. Watanabe *et al.* [26] produced water-in-oil emulsions by applying a potential difference higher than the critical voltage of emulsification. Their method was based on counteract surface tension forces by means of electrical forces. They introduced a large quantity of additives in the dispersed phase so that the electrical conductivity of continuous-phase liquid were smaller than that of the dispersed-phase liquid. Sato and coworkers[27] used the Inversed Electrostatic Spraying (IES) to disperse a dielectric liquid in a conducting liquid medium. The IES is the technique introduced by Tsouris *et al.* [28] to disperse a gas into an outer conducting medium by means of electrical fields. In this technique the dispersed phase is injected continuously through an electrified, in most cases metallic, needle. A grounded electrode is located downstream in the bath chamber in order to create an intense enough electric field. Some improvements of this technique can be found in the literature. More intense electric fields (resulting in smaller droplets) can be obtained by covering the metallic capillary nozzle with an insulating material up to the needle's tip[29]. Tsouris *et al.*[30] illustrated that a conical tip sharpened capillary and negative polarity provide better pumping, spraying and mixing. Gneist & Bart[31] used a high frequency AC power supply. There was no effect of viscosity of dispersed phase on spraying process for viscosities up to 100 mPa.s. In most of the aforementioned examples the droplet dispersion

occurs within the electrified dripping regime[32]. Experimental and numerical study was conducted in chapter 5 to explore new modes of electrohydrodynamic jetting in liquid-liquid dispersion.

1.2.3 Other methods to produce droplets

Another method called drop-on-demand (DOD) ink jet printing, to produce drops, is used widely in applications like printing [33], fabrication of transistors [34] and biochip arraying [35]. There are two DOD technologies that predominate in ink jet industry: piezo and thermal ink jet (TIJ). Piezo technology was developed by Zoltan in 1972 [36] and by Kyser and Sears in 1976 [37]. In this technology, a capillary tube made of glass is bonded to piezoelectric transducer (see fig. 1.5 (a)). The transducer receives an electric signal to produce pressure wave. The wave squeezes or relaxes the tube so, a drop of the same order of the tube size can be ejected from the nozzle by selecting the suitable voltage pulse. The great deal of this method is to get the correct shape of the waveform, amplitude and duration of the voltage pulse. Thermal ink jet (TIJ) was developed separately by Canon [38] and Hewlett-Packard [39]. The idea of this method is to use the expansion of vapor bubble formed on a heating element near to the nozzle exit in order to eject a drop from the nozzle (see fig. 1.5 (b)). One of the most important goals of many scientist is to reduce the volume of the generated drop, in order to increase the resolution in printing and to reduce the consumption of ink. So, we have conducted numerical and experimental study en chapter 6 to have a better control on a novel technique to produce drop on demand.

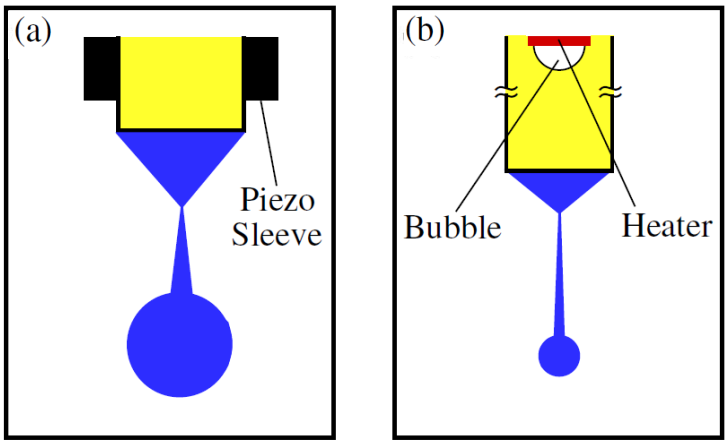

Figure 1.5: Piezo and thermal ink jet technologies, (Basaran, 2002).

1.3 Formation of capillary jet

Capillary jets are produced by exerting intense axial forces to overcome the resistance offered by viscosity and surface tension. In the simplest example of ejection through a nozzle or spinneret, a strong pressure drop must be applied to the feeding capillary and the ambient to provide the liquid with kinetic energy sufficient to create the interface. In flow-focusing and electrospray (electrospinning) [40], an outer stream and electric field, respectively, stretch a liquid meniscus until a thin jet tapers from its very tip. In the case of viscoelastic jets, an intense axial elastic tension is generated in the ligament at the ejection point. Viscoelastic material exhibits both viscous and elastic behaviour when a force is applied to it. So, it forms a longer jet than other fluids. If no further stretching occurs, the tension decays at a rate that decreases as elasticity increases [41, 42, 43]. For high enough elasticity, the axial tension survives downstream over distances much longer than the jet's diameter. Most experiments with viscoelastic jets are conducted for a relatively high elasticity,

so that its effects can be clearly appreciated. In this case, the axial tension becomes a fundamental term in the analysis of the stability of non-Newtonian jets.

If the unperturbed state is subject to unrelaxed axial elastic tension, then the nonlinear terms of the rheological model contribute to the linearized equations, and therefore the results depend on the specific model even in the linear regime. The Oldroyd-B constitutive equation [44] provides reasonably accurate predictions for viscoelastic liquids under certain conditions. Specifically, it can describe both the linear and nonlinear evolution of the so-called Boger liquids [45]. These liquids are dilute polymer solutions in solvents with a sufficiently high viscosity for elastic stresses to be measurable. They exhibit a constant viscosity (shear thinning can be neglected) over a wide range of shear rates, so that the elastic effects can be separated from the viscous ones. Goren and Gottlieb [41] analyzed the temporal linear stability of the axisymmetric mode in an Oldroyd-B capillary jet. They showed that the growth rate decreases as the axial tension increases, although there is always a range of wave numbers for which the mode is unstable. Ruo et al. [42] extended that analysis to non-axisymmetric perturbations in the presence of an unbounded inviscid gas. They also concluded that the axial stress plays a stabilizing role (these results must be reviewed because the effects of the unrelaxed tension were not accounted for correctly in the boundary conditions at the free surface). The stability analysis of annular liquid sheets also leads to the same conclusion [46].

Neither the temporal nor the spatial stability analysis can predict whether steady jetting will occur in an experimental realization. For that purpose, the convective-to-absolute instability transition must be determined from a spatiotemporal analysis [47]. If the jet is convectively unstable, an unperturbed cylindrical ligament forms next to the discharge orifice, while growing surface waves deform and eventually

pinch the interface downstream. On the contrary, absolute instability implies that perturbations travel both downstream and upstream over the jet's surface, preventing steady jetting. The convective-to-absolute instability transition has been analyzed in relaxed capillary jets exclusively [48]. In line with the temporal analysis results [41, 42, 46], one concludes that elasticity plays a destabilizing role, fostering absolute instability at the expense of the convective one. This result was subsequently extended to electrified jets [49].

1.4 Objectives and document structure

Through this thesis we pretend to study some problems aspects to produce fibers, drops and bubbles. Our objective is to study all the parameters that govern those problems in order to control the production process in efficient manner.

In chapter 2, a numerical model has been developed to do a stability analysis for an Oldroyd-B capillary jet subject to unrelaxed axial stress. Our purpose is to determine the convective to absolute instability transition. By this mean, a better control can be made on the production of fibers of viscoelastic materials.

In chapter 3, stability analysis of rivulet in mirochannel has been realized by using numerical model. The objective is to characterize the stable and unstable regimes. This study helps us to get a better knowledge of the limits where we can produce drops or bubbles using T-junction technique.

In chapter 4, our target is to obtain a reliable model to predict the evolution of a bubble of gas that slowly dissolves in an open environment, and whose size is sufficiently small to remain spherical –even subject to its buoyant rise through the surrounding liquid. In particular, our interest focuses on the total dissolution

time and distance traveled by the evolving microbubble, with the idea to make that distance traveled as close as possible to the distance from the bubble source to the free surface of the liquid: in principle, this would allow an optimal dispersion of the gas throughout the liquid column, with minimal gas loses at the free liquid surface.

In chapter 5, the objective is to study all parameters that govern the problem of the electrical disruption of pendant liquid drops in another liquid. For this purpose, a broad series of experiments have been done. Also, a numerical code was used in this study. The results reveal new modes in liquid-liquid dispersion and determine the limits of the production of micro-droplets in another liquid.

In chapter 6, experimental and numerical studies have been achieved on a novel technique to produce drop on demand. The target is to control the different parameters affecting on the production process and to use the experimental and numerical results to obtain a predictive scaling law for the droplet size.

The results in chapter 2, 3 and 4 have been published in the following articles:

- A. Said Mohamed, M. A. Herrada, and A. M. Gañán-Calvo and J. M. Montanero, "Convective-to-absolute instability transition in a viscoelastic capillary jet subject to unrelaxed axial elastic tension" Physical Review E, 92, 023006, August 2015.

- A. Said Mohamed, Miguel A. Herrada, J.M. López-Herrera and Alfonso M. Gañán-Calvo, "Isothermal dissolution of small rising bubbles in a low viscosity liquid" Chemical Engineering and Processing, 85:136-144, November 2014.

- Miguel A. Herrada, A.S. Mohamed, José M. Montanero and A.M. Gañán-Calvo "Stability of a rivulet flowing in a microchannel" International Journal of Multiphase Flow, 69:1-7, October 2014.

Chapter 2

Instability transition in a viscoelastic capillary jet

2.1 Introduction

Many practical applications involve the formation and controlled breakup of viscoelastic laminar jets. Elasticity alters fundamentally the evolution of the capillary jet not only in the ultimate nonlinear stage of its breakup, but also in the initial linear regime. It is well-known that the growth rates characterizing the linear instability of a *relaxed* (zero axial elastic tension) capillary jet are greater than their counterparts in the Newtonian case [50, 51, 52]. Therefore, elasticity plays a destabilizing role for vanishing axial tension in the unperturbed state. Interestingly, these predictions are independent of the form of the viscoelastic constitutive equation. If the axial tension of the base solution vanishes, all nonlinear terms in the constitutive relationship are eliminated after linearization, which leads to the general linear viscoelastic Jeffreys model [52].

The theoretical results mentioned above clearly contrast with most experimental observations, which repeatedly show that elasticity stabilizes the produced jets, delaying considerably their breakup [53] (a feature exploited in the industrial production of polymeric fibers). It has been argued that this discrepancy is due to the inability of the linear stability analysis to provide relevant information about the jet disintegration process. Although it is obvious that linear predictions cannot be extrapolated beyond the very first stage of the thread breakup, there is yet another effect that may also explain the lack of agreement between the linear stability predictions and the experiments: the jet's axial elastic tension [41, 42, 46].

In this chapter, we will conduct a spatiotemporal linear stability analysis of the Navier-Stokes equations for an Oldroyd-B capillary jet subject to unrelaxed axial stress. We will determine the parameter conditions for which the convective-to-absolute instability transition takes place, paying special attention to the role played by the unrelaxed elastic axial stress.

2.2 Mathematical model

In this section, we present the mathematical model with abbreviated expressions, while the expanded equations can be found in the next section. Consider a cylindrical jet of radius R and density ρ moving in the axial direction at the uniform velocity V. The properties of the outer medium are such that its dynamical effects on the jet can be neglected. Due to the smallness of the jet, the gravity effects are neglected too. In what follows, we shall make all the variables dimensionless using the radius R, velocity V, convective time R/V, and dynamic pressure ρV^2 as the characteristic length, velocity, time, and pressure, respectively. The jet rheological behavior is

described with the Oldroyd-B model [54]:

$$(1 + \lambda \mathsf{G})\, \tau_{ik} = 2Re^{-1}(1 + \beta \mathsf{G}) D_{ik} \ , \tag{2.1}$$

where $\mathsf{G}[\mathsf{A}]$ is the upper convected derivative operator, $\mathbf{D}$ the strain rate tensor, $\boldsymbol{\tau}$ is the extra stress tensor, Re=$\rho V R/\mu$ the Reynolds number, and μ the Newtonian (solvent) viscosity. The model also involves the stress and strain relaxation times λ and β. These parameters are also referred to as the Deborah number and the (dimensionless) retardation time, respectively.

The jet evolution is calculated from the conservation equations of mass and momentum:

$$\boldsymbol{\nabla} \cdot \mathbf{v} = 0 \ , \quad \frac{d\mathbf{v}}{dt} = -\boldsymbol{\nabla} p + \boldsymbol{\nabla} \cdot \boldsymbol{\tau} \ , \tag{2.2}$$

where $\mathbf{v}(\mathbf{r}, t) \equiv v_r(\mathbf{r}, t)\ \mathbf{e_r} + v_\theta(\mathbf{r}, t)\ \mathbf{e}_\theta + v_z(\mathbf{r}, t)\ \mathbf{e_z}$ and $p(\mathbf{r}, t)$ stand for the velocity and pressure fields in a cylindrical coordinate system $(\mathbf{e_r}, \mathbf{e}_\theta, \mathbf{e_z})$ whose z-axis is the jet's axis. These equations must be solved with the boundary conditions at the jet's free surface; namely, the kinematic compatibility condition and zero total stress on that surface:

$$\frac{dF}{dt} = 0 \ , \quad -p + \mathbf{n} \cdot \boldsymbol{\tau} \cdot \mathbf{n} = We^{-1} \boldsymbol{\nabla} \cdot \mathbf{n} \ , \quad \mathbf{t_1} \cdot \boldsymbol{\tau} \cdot \mathbf{n} = \mathbf{t_2} \cdot \boldsymbol{\tau} \cdot \mathbf{n} = 0 \ , \tag{2.3}$$

where $F(\mathbf{r}, t) \equiv f(\theta, z; t) - r$, f is the distance of the free surface element from the z-axis, $\mathbf{n}$, $\mathbf{t_1}$, and $\mathbf{t}_2$ are the normal and two tangential unit vectors to the free surface, respectively, $We = \rho V^2 R/\gamma$ the Weber number, and γ the surface tension. The governing equations are completed with the regularity conditions at the jet axis.

We restrict our analysis to the axisymmetric mode because it becomes dominant

for small Weber numbers, the parameter region where the convective-to-absolute instability transition is expected. In this case, one proposes the following dependence for the stress and hydrodynamic fields, and the interface position:

$$\boldsymbol{\tau}(r,z;t) = We^{-1}\tau_0\ \mathbf{e_z}\mathbf{e_z} + \varepsilon\ \hat{\boldsymbol{\tau}}(r)e^{i(kz-\omega t)} + \text{c.c.}\ , \tag{2.4}$$

$$\mathbf{v}(r,z;t) = V\mathbf{e_z} + \varepsilon\ \{\hat{v}_r(r)\mathbf{e_r}, \hat{v}_z(r)\mathbf{e_z}\}e^{i(kz-\omega t)} + \text{c.c.}\ , \tag{2.5}$$

$$p(r,z;t) - We^{-1} = \varepsilon\ \hat{p}(r)e^{i(kz-\omega t)} + \text{c.c.}\ , \tag{2.6}$$

$$f(z,t) - 1 = \varepsilon\ \hat{f}e^{i(kz-\omega t)} + \text{c.c.}\ , \tag{2.7}$$

where $k = k_r + ik_i$ is the axial wave number, and $\omega = \omega_r + i\omega_i$ the corresponding frequency. The parameter τ_0 represents the unrelaxed axial stress of the base solution in terms of the capillary pressure γ/R. If one introduces the expansions (2.4)–(2.7) into the governing equations (2.1)–(2.3), and retains terms up to the order ε, then a homogeneous system of linear equations is obtained for the perturbed fields $\{\hat{\boldsymbol{\tau}},\hat{v}_r,\hat{v}_z,\hat{p},\hat{f}\}$. These equations are discretized by expanding the fields in terms of truncated Chebyshev series [55]. The solvability condition of the resulting system of algebraic equations leads to the dispersion relation $D(\lambda,\beta,Re,We,\tau_0;k,\omega) = 0$.

The critical Weber numbers We* corresponding to the convective-to-absolute instability transition are determined by a spatiotemporal analysis of that dispersion relation. They are obtained as those for which Brigg's pinch condition [56, 47] is satisfied. This condition establishes that there must be at least one pinching of a k^+ and a k^- spatial branch with $\omega_i = 0$, where the k^+ is the path of $D = 0$ in the complex k plane which moves into the $k_i > 0$ half-plane as ω_i increases, while the k^- branch always remains in the $k_i < 0$ half-plane as ω_i increases.

2.3 Governing equations and numerical method

The Oldroyd-B model [Eq. (2.1)] can be written as

$$\begin{aligned} \boldsymbol{\tau} + \lambda \left[\frac{\partial \boldsymbol{\tau}}{\partial t} + (\mathbf{v}\cdot\boldsymbol{\nabla})\boldsymbol{\tau} - (\boldsymbol{\nabla}\mathbf{v})^{\mathrm{T}}\cdot\boldsymbol{\tau} - \boldsymbol{\tau}\cdot\boldsymbol{\nabla}\mathbf{v} \right] = \\ 2Re^{-1}\mathbf{D} + 2Re^{-1}\beta \left[\frac{\partial \boldsymbol{D}}{\partial t} + (\mathbf{v}\cdot\boldsymbol{\nabla})\boldsymbol{D} - (\boldsymbol{\nabla}\mathbf{v})^{\mathrm{T}}\cdot\boldsymbol{D} - \boldsymbol{D}\cdot\boldsymbol{\nabla}\mathbf{v} \right], \end{aligned} \tag{2.8}$$

where $\mathbf{D} = 1/2\ (\boldsymbol{\nabla}\mathbf{v} + (\boldsymbol{\nabla}\mathbf{v})^{\mathrm{T}})$ is the strain rate tensor, and $\boldsymbol{\nabla}\mathbf{v} = \partial v_j/\partial x_i$ the velocity gradient tensor. The mass and momentum conservation equations [Eqs. (2.2)] for an axisymmetric flow are

$$\frac{1}{r}\frac{\partial}{\partial r}(rv_r) + \frac{\partial v_z}{\partial z} = 0, \tag{2.9}$$

$$\frac{\partial v_r}{\partial t} + v_r\frac{\partial v_r}{\partial r} + v_z\frac{\partial v_r}{\partial z} = -\frac{\partial p}{\partial r} + \frac{1}{r}\frac{\partial}{\partial r}(r\tau_{rr}) + \frac{\partial \tau_{zr}}{\partial z} - \frac{\tau_{\theta\theta}}{r}, \tag{2.10}$$

$$\frac{\partial v_z}{\partial t} + v_r\frac{\partial v_z}{\partial r} + v_z\frac{\partial v_z}{\partial z} = -\frac{\partial p}{\partial z} + \frac{1}{r}\frac{\partial}{\partial r}(r\tau_{rz}) + \frac{\partial \tau_{zz}}{\partial z}, \tag{2.11}$$

while the boundary conditions at the free surface $r = f(z,t)$ [Eqs. (2.3)] are

$$\frac{\partial F}{\partial t} + v_r\frac{\partial F}{\partial r} + v_z\frac{\partial F}{\partial z} = 0, \tag{2.12}$$

$$-p + \frac{\tau_{rr} - 2f_z\tau_{rz} + f_z^2\tau_{zz}}{1+f_z^2} = -We^{-1}\frac{1+f_z^2 - ff_{zz}}{f(1+f_z^2)^{3/2}}, \tag{2.13}$$

$$\frac{\tau_{rz} - f_z(\tau_{zz} - \tau_{rr} + f_z\tau_{rz})}{1+f_z^2} = 0. \tag{2.14}$$

In the above equations, $f_z = df/dz$ and $f_{zz} = d^2f/dz^2$. The regularity conditions

$$\frac{\partial p}{\partial r} = 0, \quad v_r = 0, \quad \frac{\partial v_z}{\partial r} = 0, \tag{2.15}$$

at the jet axis $r = 0$ complete the set of governing equations.

The linearization of the hydrodynamic equations (2.8)–(2.11) yields

$$\hat{\boldsymbol{\tau}} = \alpha_1 \begin{bmatrix} 2\dfrac{d\hat{v}_r}{dr} & 0 & ik\hat{v}_r + \dfrac{d\hat{v}_z}{dr} \\ 0 & 2\dfrac{\hat{v}_r}{r} & 0 \\ ik\hat{v}_r + \dfrac{d\hat{v}_z}{dr} & 0 & 2ik\hat{v}_z \end{bmatrix} + ik\alpha_2 \begin{bmatrix} 0 & 0 & \hat{v}_r \\ 0 & 0 & 0 \\ \hat{v}_r & 0 & 2\hat{v}_z \end{bmatrix}, \tag{2.16}$$

$$\frac{1}{r}\frac{d}{dr}(r\hat{v}_r) + \frac{d\hat{v}_z}{dz} = 0, \tag{2.17}$$

$$i(k-\omega)\hat{v}_r = -\frac{d\hat{p}}{dr} + \frac{d\hat{\tau}_{rr}}{dr} + ik\hat{\tau}_{zr} + \frac{\hat{\tau}_{rr} - \hat{\tau}_{\theta\theta}}{r}, \tag{2.18}$$

$$i(k-\omega)\hat{v}_z = -ik\hat{p} + \frac{d\hat{\tau}_{rz}}{dr} + ik\hat{\tau}_{zz} + \frac{\hat{\tau}_{rz}}{r}, \tag{2.19}$$

where α_1 and α_2 are given by the expressions

$$\alpha_1 = Re^{-1}\frac{1 - i\beta(\omega - k)}{1 - i\lambda(\omega - k)}, \quad \alpha_2 = \frac{\lambda\, We^{-1}\tau_0}{1 - i\lambda(\omega - k)}. \tag{2.20}$$

The linear boundary conditions at the free surface $r = 1$ [Eqs. (2.12)–(2.14)] are

$$\hat{f} = i\frac{\hat{v}_r}{\omega - k}, \quad -\hat{p} + \hat{\tau}_{rr} = We^{-1}(1 - k^2)\hat{f}, \quad \hat{\tau}_{rz} - We^{-1}\tau_0 ik\hat{f} = 0, \tag{2.21}$$

while the regularity conditions at $r = 0$ lead to

$$\hat{v}_r = 0, \quad \frac{d\hat{v}_z}{dr} = 0, \quad \frac{d\hat{p}}{dr} = 0. \tag{2.22}$$

Use was made of the Chebyshev spectral collocation technique [57] to discretize Eqs. (2.16)–(2.22). This technique is based on the approach developed by Khorrami [57] for the stability analysis of swirling flows in pipes. The fields are expanded in

terms of a truncated Chebyshev series, which accumulates the grid points in the vicinity of the free surface, where larger gradients of the hydrodynamic fields are expected. The expansion must exactly satisfy the boundary conditions, which leads to an eigenvalue problem. We used the MATLAB subroutine EIGS to calculate the spectrum of eigenvalues and eigenfunctions. Spurious eigenvalues can be ruled out by comparing the computed spectra obtained for different values of the number of collocation points.

2.4 Results

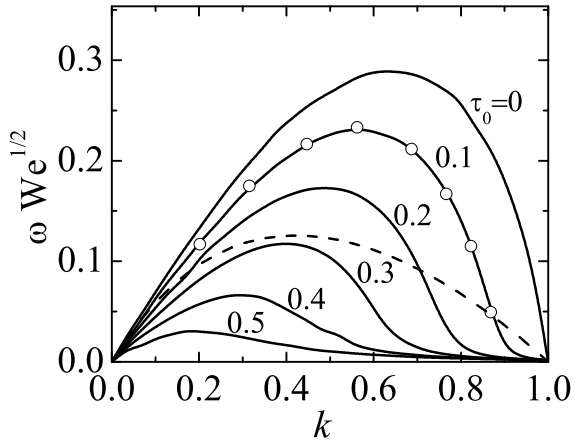

Figure 2.1: Temporal growth rate ω as a function of the (real) wave number k for $\lambda = 100$, $\beta = 10$, $Re = 0.2083$, and $We = 0.03125$. The circles correspond to the solution obtained by Goren and Gottlieb [41] for $\tau_0 = 0.1$. The dashed line is the solution for a Newtonian jet ($\lambda = \beta = \tau_0 = 0$).

Figure 2.1 shows the temporal growth rate ω as a function of the (real) wave number k for different values of the unrelaxed axial stress. That quantity was approximately calculated by applying Gaster's theorem [58] to the corresponding spatial branches. As can be observed, our solution for $\tau_0 = 0.1$ perfectly matches that

obtained by Goren and Gottlieb [41]. The unrelaxed stress stabilizes the viscoelastic jet reducing the growth rate of the capillary mode over the interval $0 \leq k \leq 1$. This effect has also been observed for other values of the governing parameters. This occurs because elastic stresses originated by the polymer stretching increase the liquid extensional viscosity. The comparison with the Newtonian case allows one to appreciate the competition between the destabilizing effect of viscoelasticity [48], and the stabilizing role played by the unrelaxed stress [41]. In fact, the growth rates are larger than their Newtonian counterparts for small enough unrelaxed stresses, while the contrary occurs for large values of this parameter. This last result partially justifies the experimental observations without resorting to the failure of the linear analysis during the jet breakup.

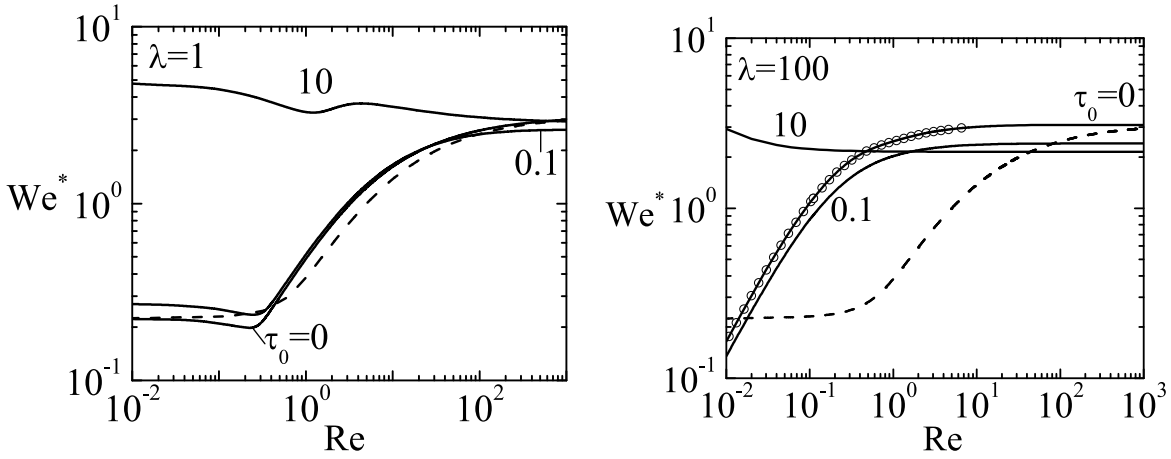

Figure 2.2: Critical Weber number We* as a function of the Reynolds number Re for $\lambda = 1$ and 100, and $\tau_0 = 0, 0.1$, and 10. The dashed lines correspond to the critical Weber number for a Newtonian jet [59]. The symbols for $\lambda = 100$ and $\tau_0 = 0$ correspond to the analytical solution for relaxed jets [48].

Now, we analyze the dependence of the critical Weber number with respect to the Reynolds and Deborah numbers, as well as the unrelaxed axial stress. We

restrict ourselves to the case $\beta = 0$ because this parameter takes very small values in most experiments with polymeric solutions. Figure 2.2 shows the critical Weber number as a function of the Reynolds number for two values of the Deborah number, $\lambda = 1$ and 100, and three values of the unrelaxed axial stress, $\tau_0 = 0, 0.1$, and 10. The numerical results perfectly match the analytical solution [48] for $\tau_0 = 0$ and $\lambda = 100$, which shows the accuracy of our numerical approach. The figure also shows the convective-to-absolute instability transition curve for a Newtonian jet ($\lambda = \tau_0 = 0$) [59]. As showed by by Montanero and Gañán-Calvo [48], elasticity enhances the absolute instability in a relaxed ($\tau_0 = 0$) capillary jet over most part of the analyzed interval of the Reynolds number. The unrelaxed tension only stabilizes the liquid thread for sufficiently large Deborah and Reynolds numbers. It must be noted that the limit $Re \to 0$ must be taken with caution, because the effects of the outer medium cannot be neglected in that case even for very small density and viscosity ratios.

The stabilizing effect of the unrelaxed tension can be clearly appreciated in Fig. 2.3, where the dependency of the critical Weber number upon $\hat{\tau}_0 = \tau_0 / We$ is shown. This latter quantity is the unrelaxed axial stress in terms of the dynamic pressure ρV^2 (instead of the capillary pressure γ/R). Contrary to what one might expect from the temporal analysis, the critical Weber number increases with $\hat{\tau}_0$ for $\lambda = 1$. In this case, the axial stress favors the upstream climbing of unstable capillary waves (absolute instability), while reducing their growth factors. For $\lambda = 10$ and 100, the transitional Weber number decreases as the unrelaxed stress increases until a turning point is reached. That point results from the crossover of two solution branches. Only the dominant branch (i.e., that with the highest Weber number) is plotted in the figure. This crossover corresponds to the existence of a double pinching

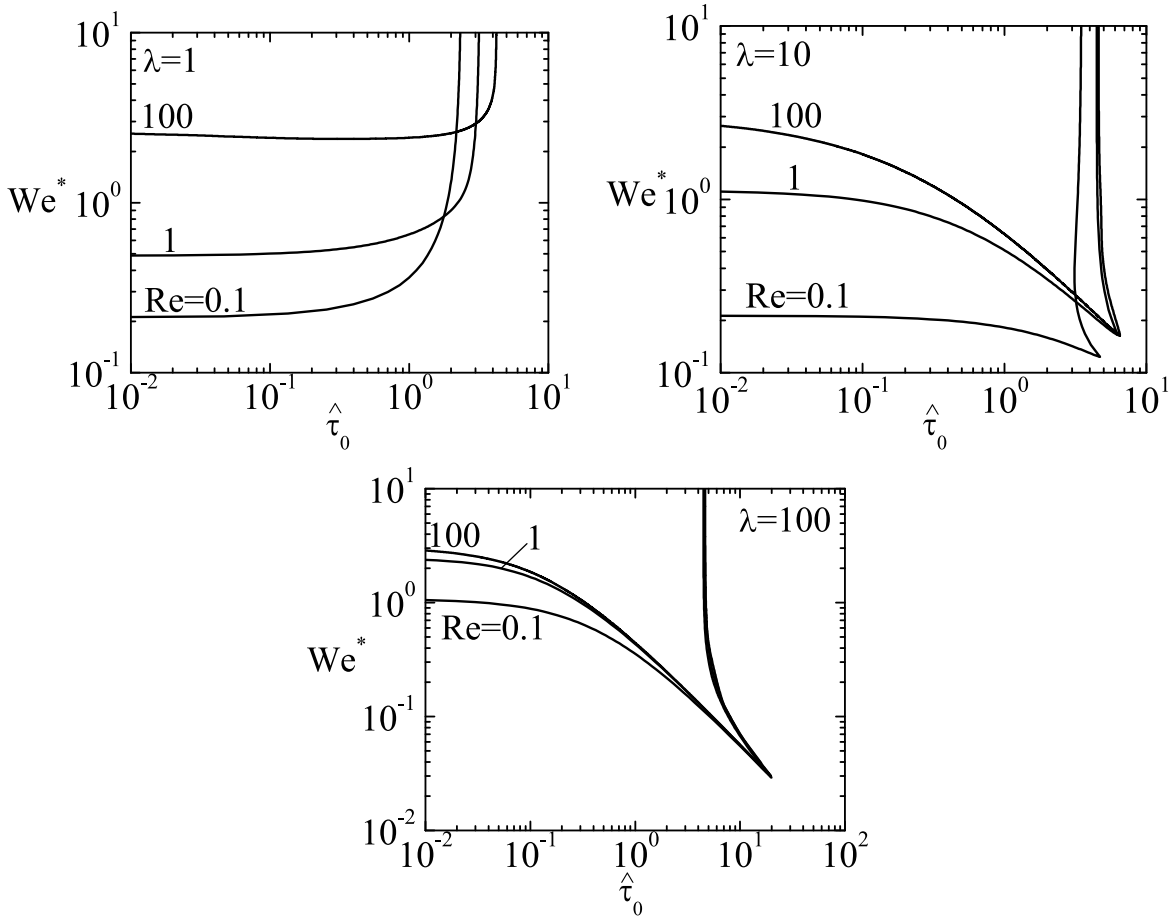

Figure 2.3: Critical Weber number We* as a function of the unrelaxed axial tension $\hat{\tau}_0$ for Re=0.1,1, and 100, and $\lambda = 1, 10$, and 100.

verifying Brigg's condition, a phenomenon also observed in compound capillary jets [60]. Figure 2.4 illustrates this peculiar situation for the case $\{We = 0.164$, Re=1, $\lambda = 10$, $\tau_0 = 1.04\}$, where one can observe how two saddle points "couple each other" through one of the spatial branches. This circumstance has a purely mathematical character, because it corresponds to a convective-to-absolute transition that could not be distinguished from others experimentally.

The dominant solution branch for large axial stresses leads to a threshold of this

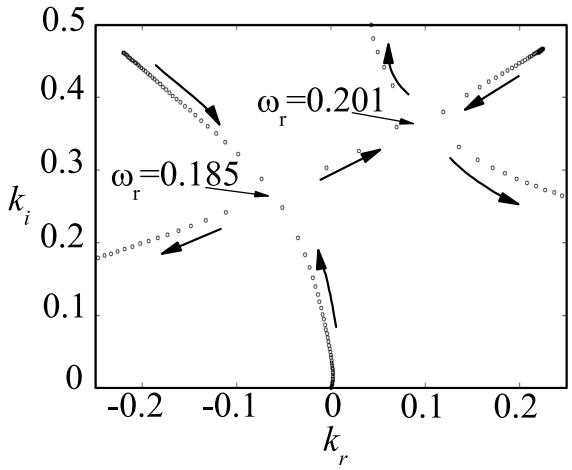

Figure 2.4: Double pinching with zero growth rate for We=0.164, Re=1, $\lambda = 10$, and $\tau_0 = 1.04$. The symbols correspond to spatial branches with $\omega_i = 0$. The arrows indicate the direction in which ω_r increases.

quantity above which the viscoelastic jet becomes absolutely unstable independently of the Weber number. This critical value is $\hat{\tau}_0 \simeq 4.63$ for sufficiently large Reynolds and/or Deborah numbers. This conclusion can also be drawn from Fig. 2.5, where the curves already plotted in Fig. 2.3 have been organized in a different manner. The existence of such a critical unrelaxed stress can be interpreted in the following way. The speed at which growing waves travel over unrelaxed viscoelastic jets increases with the elastic axial stress [61]. One may expect that if this stress, measured in terms of the dynamic (convective) pressure, exceeds a certain threshold, then the jet will fail to sweep downstream those waves (absolute instability). Therefore, the reduction of both the growth rates and the critical Weber numbers due to the unrelaxed stress is not contradictory but reasonable.

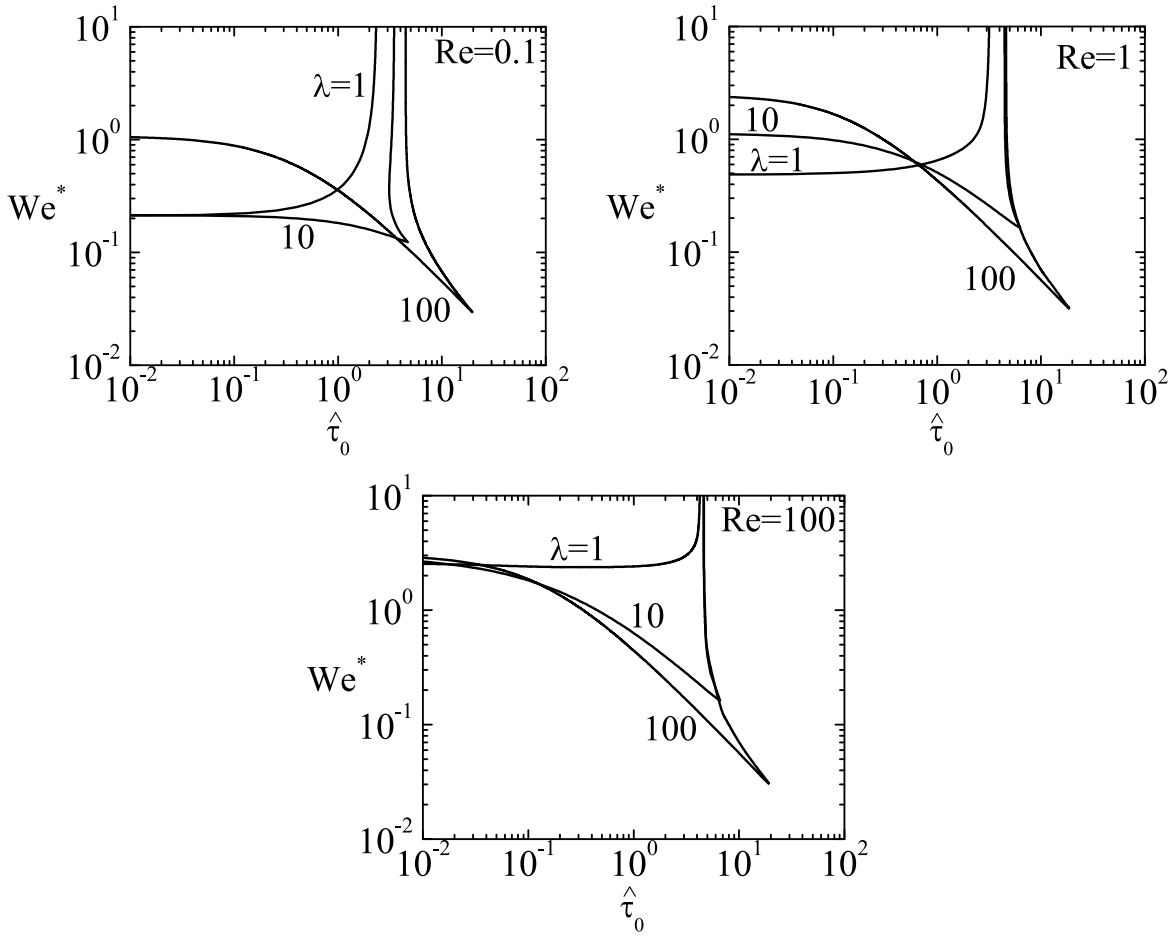

Figure 2.5: Critical Weber number We* as a function of $\hat{\tau}_0$ for $\lambda = 1, 10$ and 100, and Re=0.1,1 and 100.

2.5 Conclusions

To conclude, we have examined the convective-to-absolute instability transition under axisymmetric perturbations in an Olroyd-B capillary jet subject to unrelaxed axial stress. There is a critical Weber number below which the jet becomes absolutely unstable. The unrelaxed stress destabilizes the viscoelastic jet for small values of the Deborah number. For higher values of this parameter a more complex scenario

arises. The transitional Weber number decreases as the unrelaxed stress increases until two solution branches cross each other. The dominant branch for large axial stresses yields a threshold value of this quantity above which the viscoelastic jet becomes absolutely unstable independently of the Weber number. This threshold takes a universal value for sufficiently large Reynolds and Deborah numbers. It is well-known that the unrelaxed axial stress in a viscoelastic jet increases the speed at which capillary waves move over the jet's surface [61]. This effect allows one to understand why the axial stress may favor absolute instability while reducing the growth rates.

The linear stability analysis for Newtonian capillary jets provides valuable predictions that can be extended to the nonlinear regime. For this reason, the convective-to-absolute instability transition calculated with the linearized Navier-Stokes equations has been successfully linked to the jetting-to-dripping transition (see, e.g., [62, 63, 64]). On the contrary, polymers are significantly stretched by the growth of axisymmetric perturbations in a viscoelastic jet, which alters drastically the nonlinear behavior of this system [53]. A natural question is whether the convective-to-absolute instability transition for linear perturbations in a viscoelastic capillary jet corresponds to a true jetting-to-dripping transition. In fact, one may expect the absolute instability to manifest itself as sustained oscillations over the viscoelastic jet, rather than as the appearance of a dripping-like, beads-on-a-string, or blistering mode.

Most Boger liquids are manufactured by dissolving polymer solutes in water, and thus the capillary jets are characterized by Reynolds numbers (based on the solvent viscosity) on the order of or greater than unity. Previous results for Newtonian liquids indicate that the effect of an outer gaseous medium can be neglected except

in the limit of vanishing Reynolds numbers. Therefore, this approximation is also expected to hold in most experimental realizations with viscoelastic liquids.

Chapter 3

Stability of a rivulet in a microchannel

3.1 Introduction

When a jet touches and sticks to a solid wall, it forms a rivulet. This fluid configuration plays an important role in a number of industrial applications. Here, we just mention some examples. The interfacial shear caused by the overlying gas in heat exchangers significantly affects the performance of these devices. Rivulets driven by the shear force exerted by the surrounding air are frequently considered when studying the icing of aircraft components. When gravity is the driving force, the rivulet flow is exploited in trickle bed reactors and structured packings. Rivulets are also formed to producing coated surfaces for varied applications. In this case, one may be interested either in the formation of very uniform coatings or in the generation of certain fluid patterns. While in the former case the aim is to quench the instability mechanisms, unstable shapes are exploited in the latter one to producing

the desired pattern. Owing to the Rayleigh capillary instability [65], Newtonian laminar jets break up into streams of droplets whose diameters commensurate with that of the precursor jet. In this way, relatively monodisperse collections of droplets can be obtained from jetting realizations to build, for instance, functional materials for health care and pharmacy [66]. On the other hand, polydisperse sprays can be produced from the breakage of liquid ligaments when turbulence sets in [67].

Fluid rivulets can be produced in microfluidic devices by printing micrometer hydrophilic/hydrophobic stripes on the channel surface. A number of methods can be used for this purpose, including vapor deposition through grids, elastomer stamps, domain formation in Langmuir-Blodgett monolayers, and photolithography of amphiphilic monolayers. These chemical ducts can only be created if the contact angles characterizing the lyophilic and lyophobic surfaces verify certain conditions [68]. The use of chemical ducts in microfluidics prevents from clogging by solute particles, such as colloids or large bio-polymers, which constitutes an important advantage. Based on this idea, Herrada et al. [10] have recently proposed a microfluidic technique to produce quasi-monodisperse collections of microbubbles in a controlled manner. In this technique, a gaseous stream is injected through a T-junction into a channel transporting a liquid current. A hydrophobic strip is printed on one of the channel surfaces, and thus the gas stream forms a rivulet over that strip. If the rivulet is convectively unstable [47], it breaks up downstream due to a capillary pearling instability, which leads to a quasi-monodisperse collection of microbubbles that can be much smaller than the channel size. For the sake of illustration, Fig. 3.1 shows numerical simulations of the fluid configuration analyzed by Herrada et al. [10]. Image (a) corresponds to the case in which the gaseous rivulet does not form, while images (b) and (c) show a convectively unstable and stable rivulet, respectively.

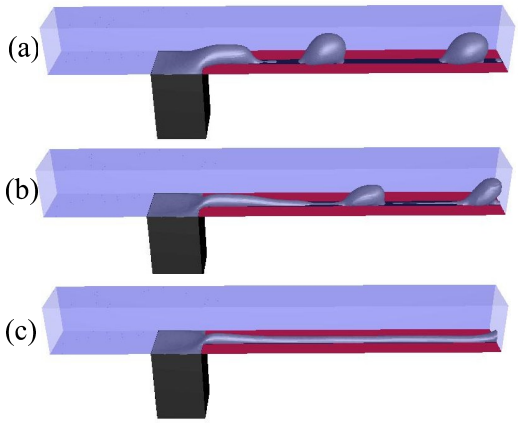

Figure 3.1: Flow snapshots for an air-ethanol rivulet [10]. The images correspond to three different regimes depending on the gas Q_g and liquid Q_l flow rates: (a) bubbling ($Q_g = 3.6$ ml/h and $Q_l = 36$ ml/h), (b) convectively unstable rivulet ($Q_g = 1.8$ ml/h and $Q_l = 72$ ml/h), and (c) stable rivulet ($Q_g = 0.09$ ml/h and $Q_l = 72$ ml/h).

The linear stability of liquid rivulets has been frequently studied over the last two decades. It crucially depends on the behavior of the triple contact lines [69]. If they are allowed to move, the rivulet suffers from pearling instability in any case (analogously to what happens in jets). If they are perfectly pinned, then a static rivulet is unconditionally stable for an unperturbed contact angle lower than 90°, while there is a range of unstable wavenumbers if the contact angle exceeds that threshold. These results were originally obtained for an infinite rivulet resting on a flat surface [70, 71], and subsequently extended to more complex equilibrium configurations, such as rivulets of finite length [72, 68] or rivulets lying on substrates of varied shapes [73].

The stability of flowing rivulets with anchored contact lines has also been considered by several authors. The lubrication and thin-film approximations have been

used to calculate the basic flows driven not only by the gravitational force [74, 75] but also by other factors, such as a prescribed uniform transverse shear stress at its free surface [76]. Under those approximations, rivulets flowing over a vertical plane [77] and under a sloping plate [78] have proved to be stable as long as their triple contact lines are fixed. Weiland and Davis [79] have shown that shallow rivulets with pinned contact lines flowing down over a vertical surface become unstable if the driving force exceeds a critical value which increases as the Reynolds number decreases. Koplik et al. [80] studied the stability of nano-rivulets driven by gravity from both the linear stability analysis of the Navier-Stokes equations and molecular dynamics simulations. The configurations analyzed were stable if and only if the contact angle was lower than 90°.

Linear stability analysis provides quantitative predictions for the size of the droplets resulting from the rivulet breakup. Diez et al. [81] have found that the distance between the drops that form during the nonlinear evolution is essentially determined by the wavelengths predicted by the linear approximation. Herrada et al. [10] have also shown a good agreement between the droplet size obtained from the linear stability analysis and the simulations of the full Naver-Stokes equations.

Several authors have studied the rivulet's stability by determining when it is energetically favorable for the rivulet to break up into sub-rivulets. Schmuki and Laso [82] found that this is the case for thin rivulets on a sloping plate under certain conditions. The combined action of a body force and a uniform longitudinal shear stress have been examined from the energy approach too [83, 84, 85, 86]. For instance, Wilson and Duffy [85] determined the conditions for which a thin rivulet on a inclined substrate and in the presence of a prescribed uniform longitudinal shear stress splits into sub-rivulets. It must be noted that it is not clear how lin-

ear stability analysis results compare with those derived from the energy method, because small disturbances are not necessarily capable of destabilizing equilibrium states corresponding to local energy minima.

In this chapter, we will extend the analysis of the rivulet's stability by considering both gas and liquid rivulets, and by extending the explored parameter region. The new results show that fluid rivulets can be unstable for contact angles smaller than 90° too. Contrarily to what one might expect, the maximum growth factor exhibits a non-monotonic dependence with respect to the Reynolds number, so that there are intervals of that parameter where the rivulet becomes unstable. As will be explained, this implies that a certain basic flow can become unstable when viscosity increases while the rest of governing parameters remain constant.

3.1.1 The governing equations

Consider an infinite rivulet of density ρ_1 and viscosity μ_1 moving over a strip of width w (Fig. 3.2). The rivulet coflows with an outer stream of density ρ_2 and viscosity μ_2 within a quadrangular channel whose side length is L. The interface surface tension is σ. We assume that the triple contact lines perfectly anchor to the straight lines delimiting the strip. Owing to the rivulet's micrometer size, gravity effects are negligible. Under this condition, the contact angle θ_{s0} formed by the unperturbed free surface and the strip univocally determines the rivulet's shape. Both the rivulet and the coflowing stream are driven by a constant pressure gradient $\mathcal{P}$. The rivulet's average velocity W_1 is a function of the above mentioned parameters. In what follows, all the quantities are made dimensionless using $R \equiv w/2$, W_1, and $\rho_1 W_1^2$ as the characteristic length, velocity, and pressure, respectively.

The velocity $\mathbf{v}^{(j)}(\mathbf{r};t) = U^{(j)}(r,\theta,z;t)\mathbf{e_r} + V^{(j)}(r,\theta,z;t)\mathbf{e}_\theta + W^{(j)}(r,\theta,z;t)\mathbf{e_z}$ and pressure $P^{(j)}(r,\theta,z;t)$ fields are described in terms of the cylindrical coordinate system $(\mathbf{e_r},\mathbf{e}_\theta,\mathbf{e_z})$. The z axis of this coordinate system is parallel to the rivulet, and the origin is located at the center of the rivulet base. Here, the superscripts $j = 1$ and 2 refer to the rivulet and coflowing stream domains, respectively. The rivulet equilibrium shape and the free surface oscillations are characterized by the functions $F_0(\theta)$ and $F(\theta,z;t)$, respectively. These functions measure the distance between a surface element and the z axis (Fig. 3.2).

The above quantities are calculated from the (incompressible) Navier-Stokes equations

$$\frac{(rU^{(j)})_r}{r} + \frac{V_\theta^{(j)}}{r} + W_z^{(j)} = 0, \tag{3.1}$$

$$\rho^{\delta_{j2}}\left(U_t^{(j)} + U^{(j)}U_r^{(j)} + \frac{V^{(j)}}{r}U_\theta^{(j)} + W^{(j)}U_z^{(j)} - \frac{V^{(j)2}}{r}\right) = -P_r^{(j)} + \frac{\mu^{\delta_{j2}}}{Re}\left[\frac{(rU_r^{(j)})_r}{r} + \frac{U_{\theta\theta}^{(j)}}{r^2} + U_{zz}^{(j)} - \frac{U^{(j)}}{r^2} - \frac{2V_\theta^{(j)}}{r^2}\right], \tag{3.2}$$

$$\rho^{\delta_{j2}}\left(V_t^{(j)} + U^{(j)}V_r^{(j)} + \frac{V^{(j)}}{r}V_\theta^{(j)} + W^{(j)}V_z^{(j)} + \frac{U^{(j)}V^{(j)}}{r}\right) = -\frac{P_\theta^{(j)}}{r} + \frac{\mu^{\delta_{j2}}}{Re}\left[\frac{(rV_r^{(j)})_r}{r} + \frac{V_{\theta\theta}^{(j)}}{r^2} + V_{zz}^{(j)} - \frac{V^{(j)}}{r^2} + \frac{2U_\theta^{(j)}}{r^2}\right], \tag{3.3}$$

$$\rho^{\delta_{j2}}\left(W_t^{(j)} + U^{(j)}W_r^{(j)} + \frac{V^{(j)}}{r}W_\theta^{(j)} + W^{(j)}W_z^{(j)}\right) = -P_z^{(j)} + \frac{\mu^{\delta_{j2}}}{Re}\left[\frac{(rW_r^{(j)})_r}{r} + \frac{W_{\theta\theta}^{(j)}}{r^2} + W_{zz}^{(j)}\right], \tag{3.4}$$

where $\rho \equiv \rho_2/\rho_1$, $\mu \equiv \mu_2/\mu_1$, δ_{ij} is the Kronecker delta, the subscripts stand for the partial derivative with respect to the corresponding variable, and $Re \equiv \rho_1 W_1 R/\mu_1$ is the Reynolds number. Equations (3.1)-(3.4) are integrated considering the kinematic compatibility

$$F_t - U^{(j)} + \frac{F_\theta}{F} V^{(j)} + F_z W^{(j)} = 0, \tag{3.5}$$

and the equilibrium of both normal and tangential stresses

$$P^{(1)} + \mathbf{n} \cdot \tau^{(\mathbf{1})} \cdot \mathbf{n} = P^{(2)} + \mathbf{n} \cdot \tau^{(\mathbf{2})} \cdot \mathbf{n} + We^{-1} \nabla \cdot \mathbf{n}, \tag{3.6}$$

$$\mathbf{t_1} \cdot \tau^{(\mathbf{1})} \cdot \mathbf{n} = \mathbf{t_1} \cdot \tau^{(\mathbf{2})} \cdot \mathbf{n}, \tag{3.7}$$

$$\mathbf{t_2} \cdot \tau^{(\mathbf{1})} \cdot \mathbf{n} = \mathbf{t_2} \cdot \tau^{(\mathbf{2})} \cdot \mathbf{n}, \tag{3.8}$$

at the free surface position $r = F(\theta, z; t)$. Here, $\tau^{(\mathbf{1})} = Re^{-1}\epsilon^{(\mathbf{1})}$ and $\tau^{(\mathbf{2})} = \mu Re^{-1}\epsilon^{(\mathbf{2})}$ stand for the viscous stress tensor on the rivulet and coflowing stream sides of the interface, respectively, while $\epsilon^{(\mathbf{1})}$ and $\epsilon^{(\mathbf{2})}$ are the corresponding values of the strain rate tensor. In addition, $\mathbf{n}$, $\mathbf{t_1}$, and $\mathbf{t_2}$ are the normal and two orthogonal tangential unit vectors with respect to the free surface, respectively, whilst $We \equiv \rho_1 W_1^2 R/\sigma$ is the Weber number. The anchorage condition $F(0, z; t) = 1$ is imposed at the edge of the strip, while non-slip conditions are prescribed at the solid surfaces. Finally, symmetry conditions are set over the plane $\theta = \pi/2$. The solution $\{\mathbf{v}^{(j)}(\mathbf{r}; t)$, $P^{(j)}(\mathbf{r}; t)$, $F(\theta, z; t)\}$ of the governing equations is therefore obtained in terms of ratio L/R and the contact angle θ_{s0} characterizing the geometry, the fluid properties ρ and μ, and the Reynolds Re and Weber We numbers.

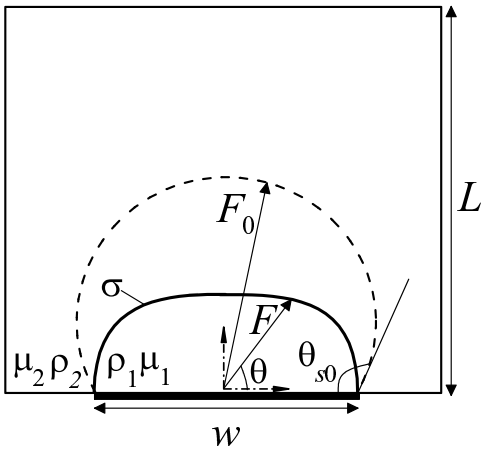

Figure 3.2: Sketch of a cross section of the fluid configuration considered. The dashed (solid) line represents the unperturbed (perturbed) rivulet shape.

3.1.2 Basic flow

The basic solution of the problem described above is the parallel flow $\mathbf{v_0}^{(j)} = W_0^{(j)}(r,\theta)\mathbf{e_z}$ and $P_0^{(j)} = \hat{P}_0^{(j)} - \mathcal{P}z$, where $\hat{P}_0^{(1)} = 1$ and $\hat{P}_0^{(2)} = 0$ are the pressures at the section $z = 0$ on both sides of the circular interface

$$F_0(\theta) = (1 + \cot^2\theta_{s0}\sin^2\theta)^{1/2} - \cot\theta_{s0}\sin\theta\ . \tag{3.9}$$

The functions $W_0^{(j)}(r,\theta)$ verify the Poisson equations

$$-\mathcal{P}Re = \mu^{\delta_{j2}}\left[\frac{(rW_{0r}^{(j)})_r}{r} + \frac{W_{0\theta\theta}^{(j)}}{r^2}\right] \tag{3.10}$$

for the rivulet and coflowing stream domains. Both the velocity and tangential stresses are continuous functions across the interface, i.e.,

$$W_0^{(1)}(F_0,\theta) = W_0^{(2)}(F_0,\theta), \tag{3.11}$$

$$a^{-1}W_{0r}^{(1)}(F_0,\theta) + b(aF_0)^{-1}W_{0\theta}^{(1)}(F_0,\theta) = \mu\left[a^{-1}W_{0r}^{(2)}(F_0,\theta) + b(aF_0)^{-1}W_{0\theta}^{(2)}(F_0,\theta)\right], \tag{3.12}$$

where $a = \sqrt{1+b^2}$, $b = -F_0'/F_0$, and the prime denotes the derivative with respect to θ. The velocity vanishes at the solid walls, and is a symmetric function with respect to the plane $\theta = \pi/2$. Because of the linear character of the problem, the product $\mathcal{P}Re$ in Eq. (3.10) is a function of the parameters $\{L, \theta_{s0}, \mu\}$ governing the basic flow.

3.1.3 Linear perturbations

In order to study the stability of the above basic flow, we consider the infinitesimal perturbations

$$\{\tilde{u}^{(j)}, \tilde{v}^{(j)}, \tilde{w}^{(j)}, \tilde{p}^{(j)}\}(r,\theta,z;t) = \{u^{(j)}, v^{(j)}, w^{(j)}, p^{(j)}\}(r,\theta)\exp\left[i(kz-\Omega t)\right] \ , \tag{3.13}$$

where k and $\Omega = \Omega_r + i\Omega_i$ are the axial (real) wavenumber and frequency, respectively. The interface position is also perturbed in the form

$$F(\theta,z;t) = F_0\left\{1 + f(\theta)\exp\left[i(kz-\Omega t)\right]\right\} \ , \tag{3.14}$$

where $f(\theta) \ll 1$ is the amplitude of the perturbation. The unit vector normal to the interface is perturbed accordingly:

$$\mathbf{n} = \mathbf{n}_0 + \tilde{\mathbf{n}}, \quad \tilde{\mathbf{n}} = \mathbf{n}^* \exp\left[i(kz - \Omega t)\right], \quad \mathbf{n}^* = \left(\frac{bf'}{a^3}\mathbf{e_r} - \frac{f'}{a^3}\mathbf{e}_\theta - \frac{fikF_0}{a}\mathbf{e_z}\right), \tag{3.15}$$

and $\mathbf{n}_0$ is the unit vector perpendicular to the unperturbed interface shape.

If one introduces the basic flow and perturbations into the incompressible Navier-Stokes equations (3.1)-(3.4), and neglects nonlinear terms, one gets

$$ikw^{(j)} + v_\theta^{(j)}/r + (ru^{(j)})_r/r = 0, \tag{3.16}$$

$$\Omega^{*(j)}u^{(j)} + \rho^{-\delta_{j2}}p_r^{(j)} - \left(\frac{\mu}{\rho}\right)^{\delta_{j2}}\frac{1}{Re}\left(\hat{\nabla}^2 u^{(j)} - \frac{u^{(j)}}{r^2} - \frac{2}{r^2}v_\theta^{(j)}\right) = 0, \tag{3.17}$$

$$\Omega^{*(j)}v^{(j)} + \rho^{-\delta_{j2}}\frac{1}{r}p_\theta^{(j)} - \left(\frac{\mu}{\rho}\right)^{\delta_{j2}}\frac{1}{Re}\left(\hat{\nabla}^2 v^{(j)} - \frac{v^{(j)}}{r^2} + \frac{2}{r^2}u_\theta^{(j)}\right) = 0, \tag{3.18}$$

$$\Omega^{*(j)}w^{(j)} + W_{0r}^{(j)}u^{(j)} + \frac{1}{r}W_{0\theta}^{(j)}v^{(j)} + \rho^{-\delta_{j2}}ikp^{(j)} - \left(\frac{\mu}{\rho}\right)^{\delta_{j2}}\frac{1}{Re}\hat{\nabla}^2 w^{(j)} = 0, \tag{3.19}$$

where $\Omega^{*(j)} = (-i\Omega + ikW_0^{(j)})$, $\hat{\nabla}^2 = \partial^2/\partial r^2 + r^{-1}\partial/\partial r - k^2 + r^{-2}\partial^2/\partial\theta^2$.

Equations (3.16)-(3.19) must be solved subject to the following boundary conditions. At the unperturbed interface position $r = F_0(\theta)$, the kinematic compatibility condition verifies,

$$i\Omega f F_0 - ikfF_0W_0^{(1)} + u^{(1)} = 0, \tag{3.20}$$

the velocity field is continuous,

$$u^{(1)} = u^{(2)}, \quad v^{(1)} = v^{(2)}, \quad w^{(1)} + F_0 f W_{0r}^{(1)} = w^{(2)} + F_0 f W_{0r}^{(2)}, \tag{3.21}$$

and the stresses on both sides of the interface are balanced,

$$\tau_{t1}^{(1)} = \mu\tau_{t1}^{(2)}, \quad \tau_{t2}^{(1)} = \mu\tau_{t2}^{(2)}, \quad p^{(1)} - p^{(2)} - Re^{-1}(\tau_n^{(1)} - \mu\tau_n^{(2)}) = We^{-1}\nabla\cdot\mathbf{n}^*, \tag{3.22}$$

$$\begin{aligned}\tau_{t1}^{(j)} &= \frac{1}{F_0^3 a^2}\Big(a_1 v^{(j)} - 2F_0F_0'v_\theta^{(j)} - a_1F_0v_r^{(j)} + 2F_0^2F_0'u_r^{(j)} - a_1u_\theta^{(j)} \\ &\quad -2F_0F_0'u - ikfaa_3\Big),\end{aligned} \tag{3.23}$$

$$\begin{aligned}\tau_{t2}^{(j)} &= \frac{1}{F_0^4 a^3}\Big(-F_0'a_2w_\theta^{(j)} + a_2F_0^2w_r^{(j)} + F_0^2a_2iku^{(j)} - F_0F_0'a_2ikv^{(j)} \\ &\quad +fa_4 - f'a_3\Big),\end{aligned} \tag{3.24}$$

$$\begin{aligned}\tau_n^{(j)} &= \frac{2}{F_0^3 a^2}\Big(F_0F_0'v^{(j)} + F_0'^2v_\theta^{(j)} - F_0^2F_0'v_r^{(j)} + F_0'^2u^{(j)} - F_0'F_0u_\theta^{(j)} \\ &\quad +F_0^3u_r^{(j)} + ikafa_5\Big),\end{aligned} \tag{3.25}$$

$$a_1 = (F_0'^2 - F_0^2), \quad a_2 = (F_0'^2 + F_0^2), \quad a_3 = F_0^3\left(W_{0\theta} + F_0'W_{0r}\right), \tag{3.26}$$

$$a_4 = a_2\left(F_0'W_{0\theta} - F_0F_0'W_{0r\theta} + F_0^3W_{0rr}\right), \quad a_5 = F_0^2\left(F_0'W_{0\theta} - F_0^2W_{0r}\right), \tag{3.27}$$

$$\begin{aligned}\nabla\cdot\mathbf{n}^* &= -\frac{f}{F_0aa_2}\left(2F_0'^2 + F_0^2 - a_2F_0^2k^2 - F_0F_0''\right) - \frac{f'}{aa_2^2F_0}\left(F_0^3F_0' + 4F_0'^3F_0\right) \\ &\quad -3F_0^2F_0'F_0'' - \frac{f''F_0}{aa_2}.\end{aligned} \tag{3.28}$$

At the solid walls and the edge of the hydrophilic/hydrophobic strip, no-slip $u^{(j)} = v^{(j)} = w^{(j)} = 0$ and anchorage $f = 0$ conditions are imposed, respectively. Finally, all the fields are symmetric functions with respect to the mid-plane $\theta = \pi/2$.

3.1.4 Temporal stability analysis

The solution of the temporal linear stability analysis is obtained in terms of the set of parameters $\{L, \theta_{s0}, \rho, \mu, Re, We\}$. First, the basic flow is calculated by solving the Poisson equations (3.10) with the corresponding boundary conditions. This solution is used in the linear problem (3.16)-(3.22) to get a homogeneous system of equations whose solvability condition leads to the dispersion relation $D(k, \Omega) = 0$.

Both the basic flow and linear perturbations are calculated numerically. The rivulet and coflowing stream domains are mapped onto fixed quadrangular domains through a coordinate transformation. The equations are discretized in the radial direction by expanding the fields in terms of truncated Chebyshev series [55, 60]. The angular derivatives were calculated with fourth-order central finite differences using uniformly distributed points. Both the fluid domain mapping and the spectral discretization accumulate the grid points in the vicinity of the free surface and solid walls, where larger gradients of the hydrodynamic fields are expected. This discretization method allows one to get very accurate results with a reduced number of grid points. Use is made of the MATLAB subroutine EIGS to calculate the eigenvalues corresponding of the resulting system of linear equations.

3.1.5 Results

In this section, we present the values of the growth factor Ω_i obtained for two fluid configurations: an air rivulet surrounded by ethanol ($\rho = 650$ and $\mu = 83.8$) and an ethanol rivulet surrounded by air ($\rho = 1.54 \times 10^{-3}$ and $\mu = 1.19 \times 10^{-2}$). We considered $L = 10$ (a value close to that of the experimental analysis that is currently underway) and three values of the unperturbed contact angle: $\theta_{s0} = 80°$, $89°$, and

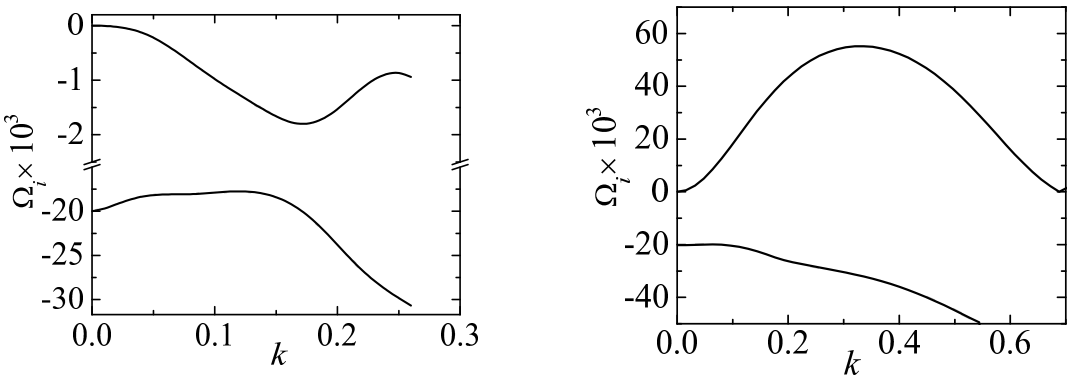

Figure 3.3: Growth factor Ω_i for an air rivulet surrounded by ethanol with $Re = 3$, $We = 0.04$, and $\theta_{s0} = 89°$ (left) and 120° (right).

120°. The Weber number was $We = 0.04$, 1, and 5, while the Reynolds number was varied over several orders of magnitude.

Figure 3.3 illustrates the dependence of the growth factor Ω_i with respect to the wavenumber for two air rivulets. In both cases, two capillary modes can be found within the range of wavenumbers and growth factors analyzed. The dominant mode, i.e., that for which the growth factor takes the maximum value, Ω_i^{max}, determines the system stability. If $\Omega_i^{max} < 0$, then the rivulet is stable under the perturbations considered, while it becomes unstable otherwise. As can be observed, the rivulet with $\theta_{s0} = 89°$ (left-hand graph) is stable because all the perturbations are damped by viscous stresses. On the contrary, the case $\theta_{s0} = 120°$ (right-hand graph) corresponds to an unstable configuration because the growth factor characterizing one of the modes becomes positive as θ_{s0} increases, and thus that mode grows driven by the surface tension force. We have verified that $\Omega_r \neq 0$ in all the cases analyzed, which means that the perturbation possesses an oscillating character.

Figure 3.4 shows the isolines of the magnitude of the velocity field perturbation

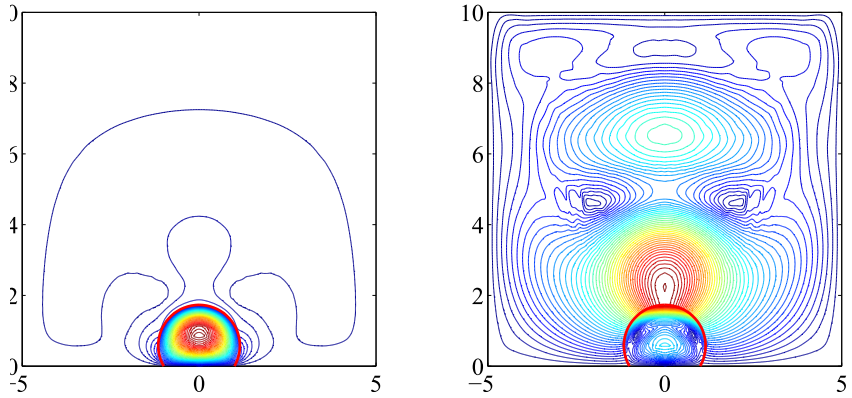

Figure 3.4: Isolines of the magnitude of the velocity field perturbation corresponding to the unstable (left) and stable (right) capillary modes obtained for $k = 0.4$ in an air rivulet surrounded by ethanol with $Re = 3$, $We = 0.04$, and $\theta_{s0} = 120°$. The red (blue) lines correspond to the higher (lower) values. The results are normalized with the maximum value in each case.

corresponding to the two capillary modes with $k = 0.4$ in Fig. 3.3-right. The left and right graphs correspond to the unstable and stable modes, respectively. The kinetic energy associated with the unstable perturbation concentrates in the gaseous rivulets, while the opposite occurs in the stable situation.

The size of the bubbles resulting from the rivulet breakup is essentially determined by the wavenumber k_{max} corresponding to the maximum value Ω_i^{max} of the growth factor (Fig. 3.5). In all the cases considered, k_{max} was at most of order unity, which means that the bubble radius was at least on the order of the strip width R. The quantity k_{max} (and therefore the bubble radius) was a monotonic function of neither the Weber nor the Reynolds number. In what follows, we will pay attention

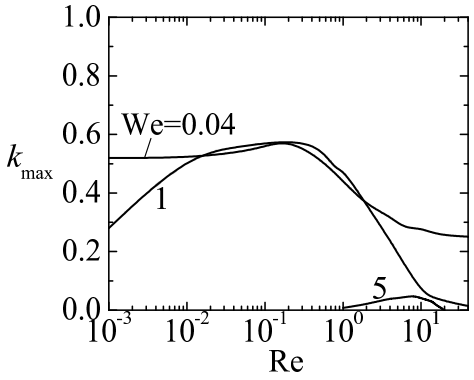

Figure 3.5: Wave number k_{max} corresponding to the maximum value of the growth factor, Ω_i^{max}, for an air rivulet surrounded by ethanol with $\theta_{s0} = 120°$.

to the dominant mode, and plot the maximum value Ω_i^{max} of the growth factor for unstable systems.

Figure 3.6 shows the values of Ω_i^{max} for an air rivulet surrounded by ethanol. The rivulet is unconditionally unstable for $\theta_{s0} = 120°$. For $\theta_{s0} = 80°$ and 89°, there is a critical Reynolds number below which the rivulet becomes unstable. This instability transition is analyzed in Fig. 3.7, which shows the growth factor Ω_i as a function of the wavenumber just above and below the critical Reynolds number. Figure 3.6 also indicates that the gaseous rivulet does not stabilize as the Reynolds number decreases, which means that this fluid configuration is unstable even for $\theta_{s0} < 90°$ and in the Stokes limit.

The above results can also be interpreted in the following way. As explained in Sec. 3.1.2, the Reynolds number does not affect the (dimensionless) zeroth-order solution. Thus, if the rest of the governing parameters remain constant, then so does the basic flow. One can vary the Reynolds number while keeping the rest of the governing parameters constant by changing just the two viscosities. Therefore, the same

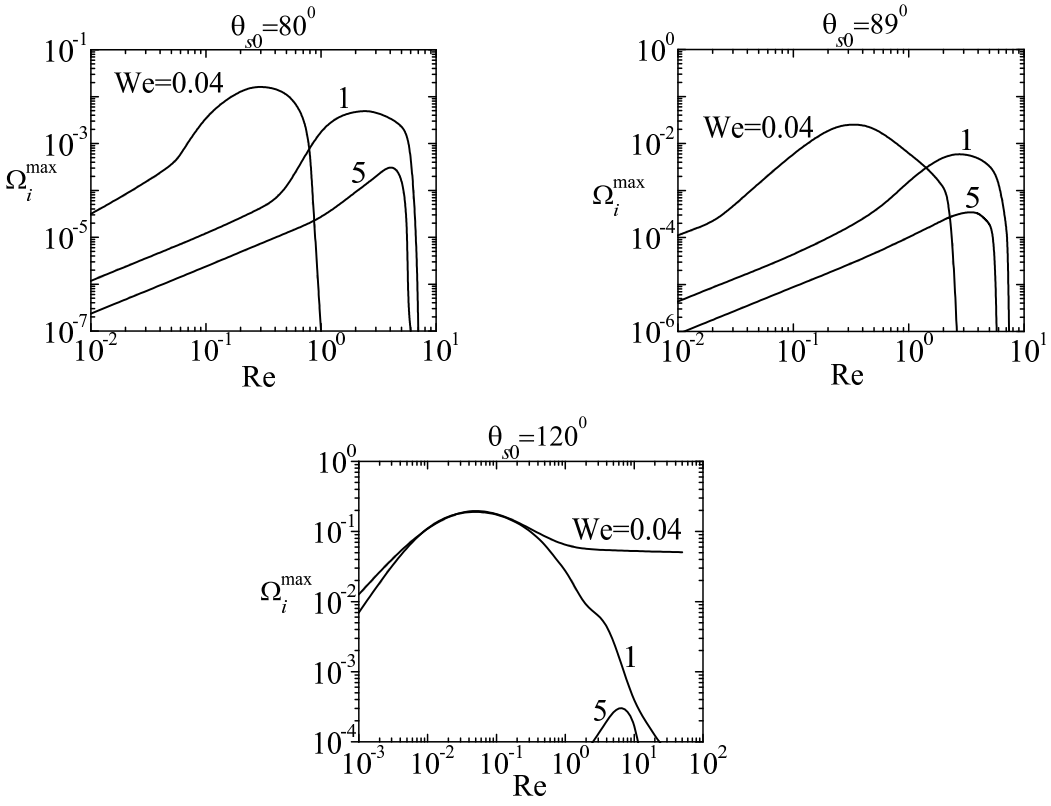

Figure 3.6: Maximum value of the growth factor, Ω_i^{max}, for an air rivulet surrounded by ethanol.

basic flow becomes unstable when the gas rivulet (and the coflowing stream) viscosity exceeds a certain critical value. The conclusion is somewhat counterintuitive: despite its dissipative character, viscosity can destabilize the fluid configuration. The fact that the growth rate (damping rate) can increase (decrease) as viscosity increases (while both the basic flow and the rest of parameters remain constant) resembles to a certain extent what happens in other systems. In axisymmetric liquid bridges, the damping rate that characterizes the dominant mode appearing after the eigenfrequency bifurcation also decreases as viscosity increases [87, 88]. In Blasius' velocity profile over a flat plate, the viscosity effects on the perturbations are neces-

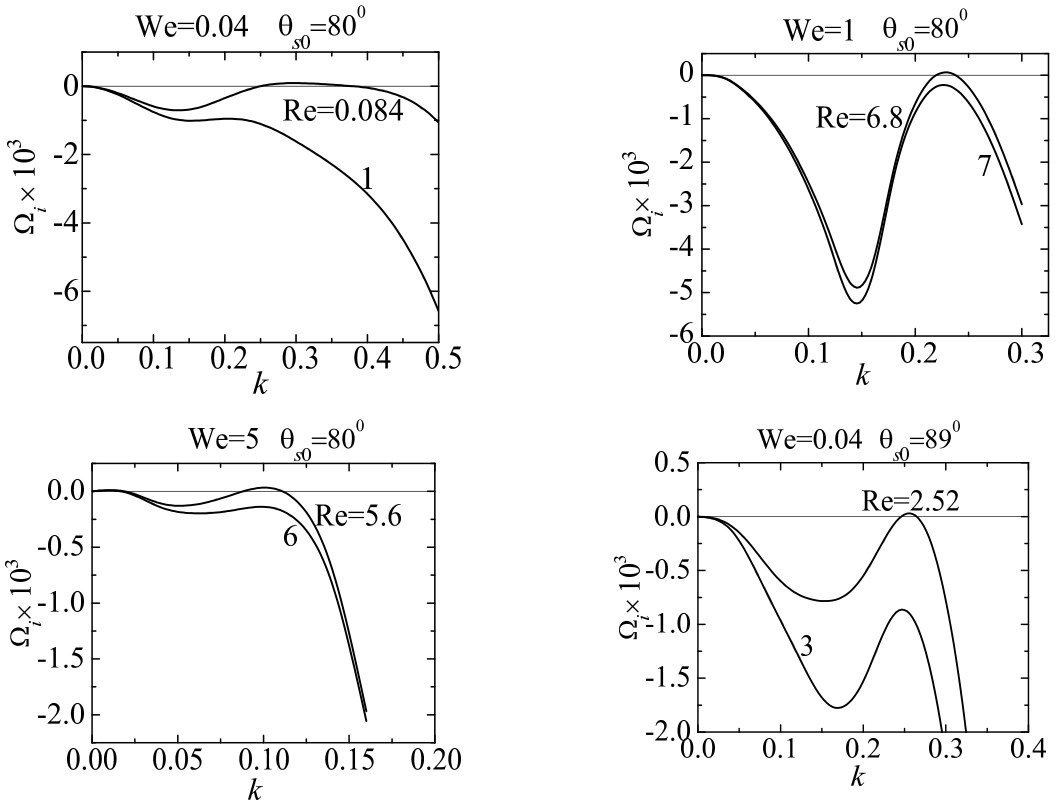

Figure 3.7: Growth factor Ω_i for an air rivulet surrounded by ethanol.

sary to explain the existence of growing modes in a convex velocity distribution [89]. As also occurs in our problem, the maximum value of the growth factor exhibits a non-monotonic dependence with respect to the viscosity for a given base flow. In fact, there is a minimum value of the Reynolds number below which the base flow recovers the stability that characterizes the inviscid case. In all these cases, viscosity appears to produce an extraction of energy from the basic motion in favor of the disturbance.

Figure 3.8 shows the maximum value of the growth factor for an ethanol rivulet surrounded by air. The results for $\theta_{s0} = 80°$ are not presented because they corre-

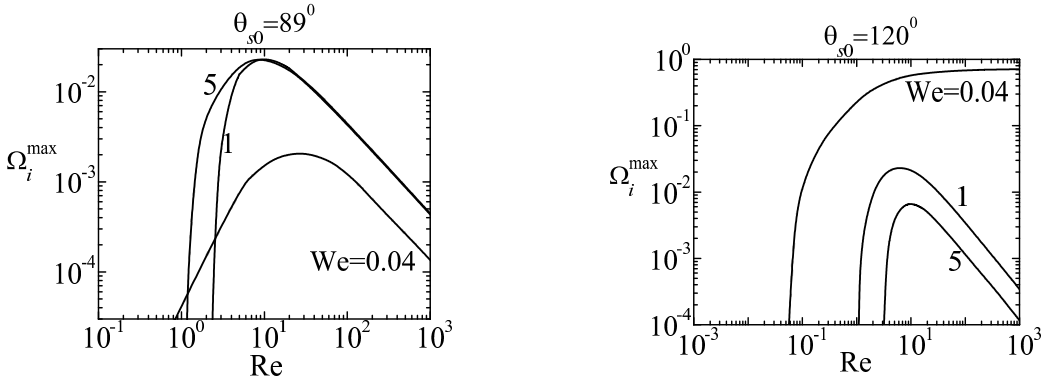

Figure 3.8: Maximum value of the growth factor, Ω_i^{max}, for a ethanol rivulet surrounded by air.

spond to stable configurations. Interestingly, the stability condition for $\theta_{s0} = 89°$ and 120° is the opposite to that of gaseous rivulets: there is a critical Reynolds number above which the rivulet becomes unstable. The system stabilizes for sufficiently low values of the Reynolds number, which is compatible with the predictions obtained from the lubrication theory for liquid rivulets [79, 77, 78]. This conclusion does not apply to the case $\theta_{s0} = 89°$ and $We = 0.04$, where the rivulet was unstable for all the Reynolds numbers considered.

3.2 Conclusions

To summarize, we have shown in this chapter the rich topology of the stability map of a rivulet coflowing with a current in a quadrangular channel. The results are qualitatively different from those of similar capillary systems, like cylindrical jets. The contact-line-anchorage condition influences fundamentally the rivulet's stability. The most noticeable results were obtained for gaseous rivulets. In spite of the dissipative character of viscosity, a basic flow can become unstable when

that quantity exceeds a certain critical value, while the rest of governing parameters remain constant. In fact, gaseous rivulets can be unstable even for $\theta_{s0} < 90^\circ$ in the Stokes limit. Contrarily to what occurs in the static case, the stability of a flowing liquid rivulet is not determined by its contact angle θ_{s0} exclusively. The Reynolds number plays a critical role too. Thus, unstable liquid rivulets with $\theta_{s0} < 90^\circ$ can be found for large enough Reynolds numbers.

A novel microfluidic technique has been recently proposed to produce microbubbles from a gaseous rivulet injected through a T-junction into a microchannel transporting a liquid current [10]. The rivulet breaks up downstream due to a capillary pearling instability, which leads to a quasi-monodisperse collection of microbubbles with diameters on the order of the width of the strip over which the rivulet formed. Decreasing the bubble diameter well below that size would imply the production of unstable rivulets with contact angles well below 90°. This is an unrealistic task because that occurs within a small parameter region.

Chapter 4

Dissolution of Micro-bubbles

4.1 Introduction

The transport in either closed channels[90] or in an open environment present radical differences not only in the obvious mechanical aspects, but most importantly –in the context of our work– in the mass exchange processes between the bubble and the environment. The dissolution of a gas bubble containing a single or multicomponent mixture has been investigated by Chain-Nan Yung et al [91]. They assumed that the gasses inside the bubble are uniform and ideal. Therefore, it will not be necessary to solve coupled equations of Navier-Stokes inside and outside the bubble. They integrated the continuity equation inside the bubble to get the velocity of the interface. Chain solved Navier-Stokes equations and the convection-diffusion equation by using finite difference procedure. Forward difference procedure was used for the time march, while central difference method was used for the space discretization. Up-wind difference was used for the convective term to overcome the problems of nonlinearity. Fumio Takemura et al [15] studied the gas dissolution of a

single rising bubble, they estimated numerically the drag coefficients and Sherwood number. In the analysis, they considered that the flow effect inside the bubble is negligible during the dissolution process, so that it is only needed to solve Navier-Stokes equation and the convection-diffusion in surrounding atmosphere to model the problem. They neglected the unsteady term and they used a K-K scheme which is a third-order upwind scheme to differentiate the equations. Then, the set of linear discretized equations, that were resulted, was solved using the SOR method.

Figure 1 shows a sketch of the fluid configuration considered in this work. A spherical gas bubble with initial radius R_o is released in a still liquid bath of density ρ and viscosity μ from the bottom of a tube filled with liquid (water). the height of the liquid column is H_o and its free surface is open to air at atmospheric pressure p_a. The mass concentration of gas dissolved in the liquid bulk, c_∞, is assumed to be homogeneous. Denoting by χ the molar fraction of oxygen of the atmosphere at the upper free surface of the liquid, the partial pressure of O_2 in that location is given by Dalton's law, χp_a and, consequently, the concentration c_∞ is given by the Henry's law, $c_\infty = \chi p_a / K_H$. K_H is the Henry constant. Due to the buoyancy force, the bubble rises at velocity $V(t)$. Simultaneously, the bubble exchanges gas with the liquid, and its radius $R(t)$ varies on its way to the surface due to either the change of liquid hydrostatic pressure and the dissolution of the gas in the surrounding liquid. We assume that the surface tension γ between the gas and the liquid is large enough to ensure that the bubble remains spherical during its ascent. i. e. $\gamma >> \rho g R_o^2$, where g is the acceleration of gravity. The bubble radius for which buoyancy and surface tension forces become comparable is $R_c = \left(\frac{\gamma}{4\rho g}\right)^{1/2}$. For an air bubble in water, that gives $R_c = 1.35$ mm. In this work, we will always consider sub-millimeter bubbles. Thus, the pressure inside the bubble, $p_g(t)$, is assumed nearly

homogeneous, being its value given by the external liquid hydrostatic pressure and the surface tension force, $p_g(t) = p_a + \rho g H(t) + 2\gamma/R(t) - p_v(t) \equiv p_b(t) - p_v(t)$, where $p_v(t)$ is the liquid vapor pressure at the local liquid temperature, assuming that the kinetics of evaporation into the small bubble has characteristic times much smaller than the hydrodynamic times (i.e., assuming that the gas in the bubble is saturated with water vapor). $p_v(t)$ is given by:

$$p_v(t) = (p_a + \rho g H(t) + 2\gamma/R(t)) \exp\left[\int_{T_o}^{T} L_w(T) \Re^{-1} T^{-2} dT\right] \tag{4.1}$$

where $\Re$ is the universal gas constant, T_o the boiling temperature of the liquid at $p_g(t)$, and T its local temperature. L_w is the latent heat of vaporization. The specific systems onto which we will apply our model work at room temperature and thus, for the case of water, one has that the molar fraction of liquid vapor in the bubble is

$$p_v(t)/(p_a + \rho g H(t) + 2\gamma/R(t)) \sim \exp\left[L_w \Re^{-1} T^{-2}(T - T_o)\right] \lesssim O(10^{-2}). \tag{4.2}$$

Assuming that the gas in the bubble has a dominant constituent, and that $p_a \gg \rho g H$, one may compare surface tension overpressure and vapor pressure through the non-dimensional number

$$\xi_1 = \frac{p_a \exp\left[L_w \Re^{-1} T^{-2} \Delta T\right]}{\gamma/R_o} \tag{4.3}$$

where $\Delta T = T_o - T$. This number defines a critical bubble radius R_o^*, sufficiently below (above) which surface tension overpressure (vapor pressure) dominates. For water in atmospheric conditions, $R_o^* \simeq 0.05$ mm. Next, the relative weight of the

hydrostatic overpressure and the vapor pressure of the liquid can be expressed by the non dimensional number

$$\xi_2 = \frac{\rho g H_o}{p_a \exp\left[L_w \Re^{-1} T^{-2} \Delta T\right]} \tag{4.4}$$

The critical height sufficiently above (below) which hydrostatic pressure (vapor pressure) dominates is given by $H_o^* = \frac{p_a \exp\left[L_w \Re^{-1} T^{-2} \Delta T\right]}{\rho g}$. Our working conditions (air in water, atmospheric pressure) provide $H_o^* \simeq 150$mm. Thus, both the liquid surface tension and vapor pressures can be neglected in the analysis for bubble sizes larger than R_o^*, and rising bubble columns sufficiently larger than H_o^*.

We use spherical coordinates (r, θ, φ) centered in the bubble and aligned with the vertical tube (see Fig.4.1 (b)) to analyze the problem. In this frame of reference the liquid far-velocity field corresponds to a uniformly descending velocity $V(t)$. Moreover, since we consider relatively small bubbles, in principle we assume dominance of viscous forces, although we will not dismiss inertia. Thus, the problem is axisymmetric as far as the Reynolds number $Re_o = 2\left(\frac{2\rho^2 g R_o^3}{\mu^2}\right)^{1/2}$ remains smaller than about 10^2, and henceforth we drop the coordinate φ.

In this chapter, we propose a model made of a set of relatively general equations and boundary conditions that are resolved by an efficient pseudospectral technique. Then the experimental validation of our results is performed by the use of a setup inspired in the previous mentioned Rising Bubble Apparatus without resorting to pressurization. Finally, gathers results from both simulation and experiments to show a satisfactory agreement, thus validating our approach.

4.2 Problem formulation

4.2.1 Governing equations

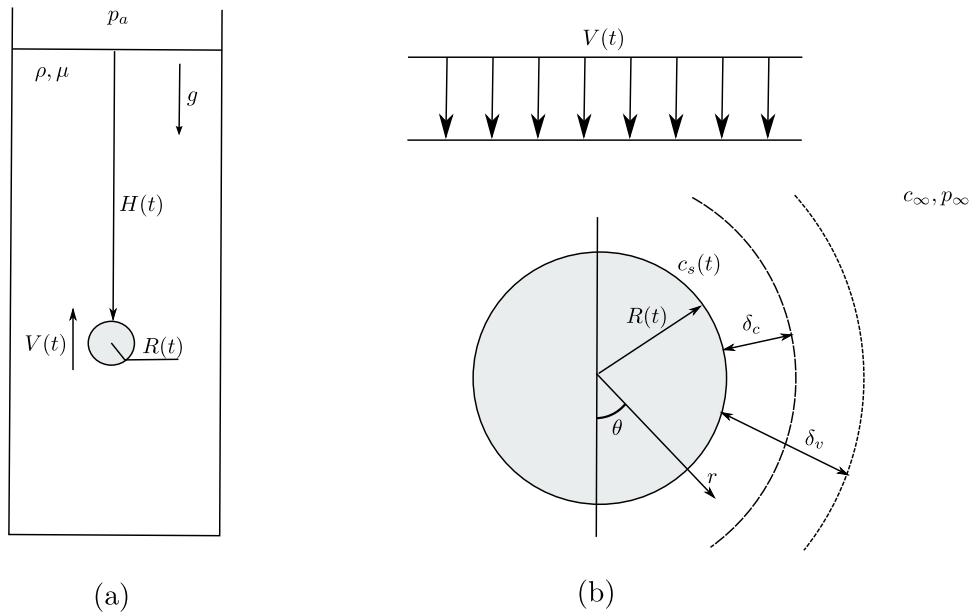

Figure 4.1: Scheme of the problem.

To study the problem of the dissolved bubble rising in a still liquid, a derivation of the differential form of continuity equation and momentum equation has been made to get the final form of incompressible axisymmetric Navier-Stokes equations for the liquid velocity $\mathbf{v}(r, \theta; t)$ and dynamic pressure $p_d(r, \theta; t)$ fields as follow:

The differential form of the continuity equation, for incompressible flow

$$\nabla \cdot \mathbf{v} = 0, \tag{4.5}$$

That writes in spherical coordinate as,

$$u_r + \frac{2u}{r} + \frac{w_\theta}{r} + \frac{w\cot\theta}{r} = 0, \tag{4.6}$$

where subscripts r and θ denote the spatial derivatives with respect to r and with respect to θ. The differential form of the momentum equation taking into account the incompressible assumption and assuming constant viscosity is

$$\rho\left(\mathbf{v}_t + \mathbf{v}\cdot\nabla\mathbf{v}\right) = -\nabla p_d + \mu\nabla^2\mathbf{v}, \tag{4.7}$$

In spherical coordinate for r-direction writes

$$\rho\left(u_t + uu_r + \frac{wu_\theta}{r} - \frac{w^2}{r}\right) = -p_{d_r} + \mu\left(u_{rr} + \frac{2u_r}{r} + \frac{u_{\theta\theta}}{r^2} + \frac{u_\theta\cot\theta}{r^2} - \frac{2u}{r^2} - \frac{2w_\theta}{r^2} - \frac{2w\cot\theta}{r^2}\right), \tag{4.8}$$

For θ-direction writes,

$$\rho\left(w_t + uw_r + \frac{ww_\theta}{r} + \frac{wu}{r}\right) = -\frac{1}{r}p_{d\theta} + \mu\left(w_{rr} + \frac{2w_r}{r} + \frac{w_{\theta\theta}}{r^2} + \frac{w_\theta\cot\theta}{r^2} + \frac{2u_\theta}{r^2} - \frac{w}{r^2\sin^2\theta}\right), \tag{4.9}$$

where subscript t denote the derivative with respect to the time. The incompressible axisymmetric Navier-Stokes equations for the liquid velocity $\mathbf{v}(r,\theta;t)$ and dynamic pressure $p_d(r,\theta;t)$ fields, are made dimensionless by using as characteristic quantities $R_o = R(0)$, and the terminal velocity for a bubble of radius R_o in the Stokes limit, $U_c = \rho g R_o^2/(3\mu)$ are

$$u_r + \frac{2u}{r} + \frac{w_\theta}{r} + \frac{w\cot\theta}{r} = 0, \tag{4.10}$$

$$u_t+uu_r+\frac{wu_\theta}{r}-\frac{w^2}{r}=-p_{d_r}+\frac{1}{Re}\left[u_{rr}+\frac{2u_r}{r}+\frac{u_{\theta\theta}}{r^2}+\frac{u_\theta\cot\theta}{r^2}-2\left(\frac{u}{r^2}+\frac{w_\theta}{r^2}+\frac{w\cot\theta}{r^2}\right)\right], \tag{4.11}$$

$$w_t+uw_r+\frac{ww_\theta}{r}-\frac{wu}{r}=-\frac{p_{d\theta}}{r}+\frac{1}{Re}\left[w_{rr}+\frac{2w_r}{r}+\frac{w_{\theta\theta}}{r^2}+\frac{w_\theta\cot\theta}{r^2}-\frac{w}{r^2\sin^2\theta}+\frac{2u_\theta}{r^2}\right], \tag{4.12}$$

where u/w is the radial/meridional velocity component and $Re=\rho U_c R_o/\mu$ is the Reynolds number. Note that the Stokes limit underestimates drag above $Re\sim 10$, and thus one should switch to a more realistic Reynolds as defined above, Re_o, to estimate the drag forces, where $Re_o=24^{1/2}Re^{1/2}$. When $Re_o\sim Re$, both viscous and inertia drag forces become comparable. The critical radius for which $Re_o=Re$ is $R_o^{**}=\left(\frac{72\mu}{\rho g}\right)^{1/3}$. For an air bubble in water, this gives $R^{**}=0.194$ mm. Note that the total pressure field, p, is the sum of the dynamic pressure and an hydrostatic part, $p=p_d+p_h$, being

$$-\nabla p_h+\rho g-\rho\dot{V}=0, \tag{4.13}$$

$$p_h=\int\left(\rho g-\rho\dot{V}\right)dz, \tag{4.14}$$

Thus, the dimensionless hydrostatic pressure is,

$$p_h=C+\frac{z}{Fr}-\dot{V}z, \tag{4.15}$$

where C is a constant, z the vertical coordinate, $Fr = U_c^2/gR_o$ the Froude number and the symbol $\dot{}$ denotes time derivative. The last term in (4.15) is due to the use of a non-inertial frame of reference.

We impose the equilibrium of tangential stress and the kinematic condition,

$$r\left(\frac{w}{r}\right)_r + \frac{u_\theta}{r} = 0, \tag{4.16}$$

$$w_r - \frac{w}{r} + \frac{u_\theta}{r} = 0, \tag{4.17}$$

where $u_\theta = 0$ and the velocity in r-direction is constant with respect to θ

As a consequences, the boundary condition at the bubble surface, $r = R(t)$,

$$u = \dot{R}, \quad \text{and} \quad w_r - w/r = 0. \tag{4.18}$$

Additionally, it has to be considered the convection-diffusion equation to get $c(r, \theta, t)$ which is the volume fraction of dissolved gas around the bubble,

The differential form of the convection-diffusion equation,

$$c_t + \mathbf{v} \cdot \nabla c = D\nabla^2 c, \tag{4.19}$$

being each term,

$$\mathbf{v} \cdot \nabla c = uc_r + \frac{wc_\theta}{r}, \tag{4.20}$$

$$\nabla^2 c = \frac{2c_r}{r} + c_{rr} + \frac{c_\theta \cot\theta}{r^2} + \frac{c_{\theta\theta}}{r^2}, \tag{4.21}$$

So that,

$$c_t + uc_r + w\frac{c_\theta}{r} = D\left(c_{rr} + \frac{2c_r}{r} + \frac{c_{\theta\theta}}{r^2} + \frac{\cot\theta c_\theta}{r^2}\right), \tag{4.22}$$

The dimensionless convection-difussion equation for the volume concentration in dimensionless form has is,

$$\Phi_t + u\Phi_r + w\frac{\Phi_\theta}{r} = \frac{1}{Pe}\left(\Phi_{rr} + \frac{2\Phi_r}{r} + \frac{\Phi_{\theta\theta}}{r^2} + \frac{\cot\theta\Phi_\theta}{r^2}\right), \tag{4.23}$$

where the dimensionless concentration of dissolved gas, Φ, is given by,

$$\Phi = \frac{c - c_\infty}{c_{so} - c_\infty}, \tag{4.24}$$

being $c(r,\theta,t)$ the mass fraction of gas inside the liquid, $c_{so} = c_s(0)$ the initial mass concentration at the surface of the bubble, c_∞ the initial volume concentration of gas dissolved in the liquid and $Pe = R_o U_c/D$ the Peclet number, where D is the gas-liquid molecular diffusivity.

The Henry's law yields the partial pressure of the gas in the liquid $p(r,\theta,t)$ as a function of the concentration of gas $c(r,\theta,t)$, $p_p = K_H c$, where K_H is the Henry's constant. Depending on the definition of the concentration used (i.e.mass concentration, molar concentration, mass fraction, etc.), the physical dimensions of the proportionality constant K_H would vary accordingly. In the present work K_H has dimensions of pressure since the concentration is defined as the mass fraction. The mass fraction of gas in the liquid at the bubble surface, $c_s(t)$, can be related to the gas pressure inside the bubble as $c_s(t) = p_g(t)/K_H$, and, in the liquid bulk, it can be written $\chi p_a = K_H c_\infty$. Therefore, the surface condition for Φ can be written

as,

$$\Phi_s = \frac{c_s - c_\infty}{c_{so} - c_\infty} = \frac{p_g(t) - \chi p_a}{p_g(0) - \chi p_a} = \alpha_1 + \alpha_2 H(t), \tag{4.25}$$

where

$$\alpha_1 = \frac{p_a - \chi p_a}{p_{ref}} \quad \text{and} \quad \alpha_2 = \frac{\rho g R_o}{p_{ref}}, \tag{4.26}$$

being $p_{ref} = p_g(0) - \chi p_a$.

Away from the bubble, $r \to \infty$, the velocity matches the external field and the volume fraction the bulk volume fraction,

$$\lim_{r\to\infty} u = V(t)\cos\theta, \quad \lim_{r\to\infty} w = -V(t)\sin\theta \quad \text{and} \quad \lim_{r\to\infty} \Phi = 0. \tag{4.27}$$

At any time,$V(t)$, is computed by the integration of the equation of motion for the spherical bubble, which neglecting the mass of the gas inside the bubble writes as follow,

$$\frac{4}{3}\pi R^3 \rho_g \dot{V} = -\frac{4}{3}\pi R^3 \rho_g g - D_h - Drag, \tag{4.28}$$

where ρ_g is the density of the gas inside the bubble, D_h is the static part of the drag and $Drag$ it's dynamic part,

$$Drag = 2\pi R^2 \int_0^\pi (-p_d Re + 2u_r)\cos\theta \sin\theta d\theta \,. \tag{4.29}$$

The static part is,

$$D_h = \int_\Sigma p_h \vec{n} d\sigma = \int_\Omega \nabla p_h d\Omega, \tag{4.30}$$

$$D_h = \int_\Omega \left(-\rho g + \rho \dot{V}\right) d\Omega = \frac{4}{3}\pi R^3 \left(-\rho g + \rho \dot{V}\right), \tag{4.31}$$

So,

$$\frac{4}{3}\pi R^3 \rho_g \dot{V} = \frac{4}{3}\pi R^3 \left(\rho g - \rho_g g - \rho \dot{V}\right) - Drag, \tag{4.32}$$

$$\frac{4}{3}\pi R^3 \left(\rho + \rho_g\right) \dot{V} = \frac{4}{3}\pi R^3 \left(\rho - \rho_g\right) g - Drag, \tag{4.33}$$

ρ_g is neglected since $\rho_g \ll \rho$, resulting,

$$\frac{4}{3}\pi R^3 \rho \dot{V} = \frac{4}{3}\pi R^3 \rho g - Drag, \tag{4.34}$$

Finally, the above equation in dimensionless form is,

$$\dot{V} = \frac{1}{Fr}\left(1 - \frac{Drag}{4\pi R^3}\right). \tag{4.35}$$

By applying the mass balance relationship at the bubble-liquid interface[15],

$$\frac{d}{dt}\left(\frac{4}{3}\pi R^3 \rho_g\right) = 2\pi R^2 \rho_l D \int_0^\pi c_r \sin\theta d\theta, \tag{4.36}$$

The dimensionless form of the previous equation is

$$\frac{2}{3}\frac{R_o}{t_o \Re T}\left(3\dot{R}\left(\Phi_s p_{ref} + p_\infty\right) + R\dot{\Phi}_s p_{ref}\right) = \frac{c_{so} - c_\infty}{R_o}\rho_l D \int_0^\pi \Phi_r(r = R, \theta) \sin\theta d\theta, \tag{4.37}$$

Or,

$$\frac{2}{3p_{ref}}\frac{R_o K_H U_c}{\rho_l D \Re T}\left(3\dot{R}\left(\Phi_s p_{ref}+p_\infty\right)+R\dot{\Phi}_s p_{ref}\right)=\int_0^\pi \Phi_r(r=R,\theta)\sin\theta d\theta, \quad (4.38)$$

finally, the above equation writes in dimensionless form as,

$$\frac{2}{3}\lambda[3\dot{R}(\Phi_s+\alpha_3)+R\dot{\Phi}_s]=-S_h, \quad (4.39)$$

where $\lambda = R_o B U_c/D$, being $B = K_H/(\rho_l \Re T)$ and $\alpha_3 = \frac{p_{p\infty}}{p_{ref}}$. At each time the Smith' number S_h is computed numerically as

$$S_h = -\int_0^\pi \Phi_r(r=R,\theta)\sin\theta d\theta. \quad (4.40)$$

The derivative of the pressure with respect to time $\dot{\Phi}_s = \alpha_2 \dot{H}$ results in,

$$3\dot{R}(\Phi_s+\alpha_3)+\alpha_2 R\dot{H}=-\frac{3S_h}{2\lambda}, \quad (4.41)$$

Taking into account equation (4.25) and the equation for the evolution of H,

$$\dot{H}=-V, \quad (4.42)$$

it is obtained the equation for the time evolution of the radius of the bubble

$$\dot{R}=\frac{-3/2\lambda^{-1}S_h+\alpha_2 RV}{3(\Phi_s+\alpha_3)}. \quad (4.43)$$

Present problem must to be closed by the appropriate value of the partial pressure of O_2 at the upper water-air interface in the tube or, in other words, by the proper

value of the molar fraction of oxygen at the upper interface, χ. If the surrounding atmosphere is renovated with pure air,the value of χ should be close to 0.21 (i.e., $p_{p_\infty} = 0.21 p_a$). However, if the atmosphere is locally enriched by the liberation of oxygen and the renovation is hampered, this value can easily raise, reaching nearly pure oxygen atmosphere concentrations. Thus, when air renovation is not dominated by horizontal convection or mixing, which is the case in the tube over the water-air interface, the proper value would come by imposing a global mass balance between the injected oxygen in the bath and that released by diffusion and convection in vertical direction over the upper free surface.

4.2.2 Numerical procedure

Since the size of the bubble is changing with time, the following mapping was made from the physical plane (r, θ, t) to the computational plane (η, ζ, τ),

$$\eta = \frac{r}{R(t)}, \quad \zeta = \theta, \quad \tau = t. \tag{4.44}$$

Due to the large differences between the Re and Pe numbers present in the experiments ($Re \sim 50$ and $Pe \sim 30000$) two different computational domains will be used to solve the velocity and pressure fields and the gas concentration in the liquid at the corresponding boundary layers of characteristic width δ_c and δ_v, respectively (see figure 4.1.b). For the mechanical problem it is sufficient to truncate the radial domain to an external radius, $R_V(t) = 30R(t)$ ($\eta_v = 30$), while for solving the concentration boundary layer the domain is truncated at a much closer external radius, $R_c(t) = 200Pe^{-0.5}R(t)$ ($\eta_c = 200Pe^{-0.5}$).

The time procedure is described next. The time domain is discretized using a

fixed time step $d\tau$. At given time, $\tau^N = Nd\tau$, the terminal velocity, V^N, the height of the bubble, H^N and the radius of the bubble, R^N are obtained from previous times, τ^{N-1} and τ^{N-2}, by discretizing in time equations (4.35), (4.42) and (4.43) at time τ^{N-1}, using 2^{nd} order central finite differences

$$V^N = V^{N-2} + 2d\tau \frac{1}{Fr}\left(1 - \frac{Drag^{N-1}}{4\pi(R^{N-1})^3}\right), \tag{4.45}$$

$$H^N = H^{N-2} - 2d\tau V^{N-1}, \tag{4.46}$$

$$R^N = R^{N-2} + 2d\tau \frac{-3/2\lambda^{-1}Sh^{N-1} - \alpha_2 R V^{N-1}}{3(\Phi_s^{N-1} + \alpha_4) - \alpha_3/R^{N-1}}. \tag{4.47}$$

By the other hand, for the computation of the time evolution of Navier-Stokes equations (4.10)-(4.12) and the convection-diffusion equation (4.23), a mixed implicit-explicit second order projection scheme based on backwards differentiation is employed.[92] Spatial discretization in the (η, ζ) semiplanes employs n_η Chebyshev spectral collocation points in η, and n_ζ points in the ζ direction.

These schemes lead to the following set of Helmholtz-type equations:

$$\left(\frac{3Re}{2d\tau} - \frac{1}{R^2}\frac{\partial^2}{\partial\eta^2} - \frac{2}{\eta R^2}\frac{\partial}{\partial\eta} + \frac{2}{\eta^2 R^2}\right)\tilde{u}^N - \frac{1}{\eta^2 R^2}\left(\frac{\partial^2}{\partial\zeta^2} + cot\theta\frac{\partial}{\partial\zeta}\right)\tilde{u}^N = fu \tag{4.48}$$

$$\left(\frac{3Re}{2d\tau} - \frac{1}{R^2}\frac{\partial^2}{\partial\eta^2} - \frac{2}{\eta R^2}\frac{\partial}{\partial\eta}\right)\tilde{w}^N - \frac{1}{\eta^2 R^2}\left(\frac{\partial^2}{\partial\zeta^2} + cot\zeta\frac{\partial}{\partial\zeta} + \frac{1}{sin^2\zeta}\right)\tilde{w}^N = fw \tag{4.49}$$

$$\left(\frac{3Pe}{2d\tau} - \frac{1}{R^2}\frac{\partial^2}{\partial\eta^2} - \frac{2}{\eta R^2}\frac{\partial}{\partial\eta}\right)\tilde{c}^N - \frac{1}{\eta^2 R^2}\left(\frac{\partial^2}{\partial\zeta^2} + cot\zeta\frac{\partial}{\partial\zeta}\right)\tilde{c}^N = fc \tag{4.50}$$

where,

$$fu = Re\left(-2convu^{N-1} + convu^{N-2} - \frac{1}{R}\frac{\partial p}{\partial \eta} + \frac{4u^{N-1} - u^{N-2}}{2d\tau}\right), \quad (4.51)$$

$$fw = Re\left(-2convw^{N-1} + convw^{N-2} - \frac{1}{\eta R}\frac{\partial p}{\partial \zeta} + \frac{4w^{N-1} - w^{N-2}}{2d\tau}\right), \quad (4.52)$$

$$fc = Pe\left(-2convc^{N-1} + convc^{N-2} + \frac{4c^{N-1} - c^{N-2}}{2d\tau}\right), \quad (4.53)$$

and,

$$convu = \frac{1}{R}\left(u - \eta\dot{R}\right)\frac{\partial u}{\partial \eta} + \frac{w}{\eta R}\left(\frac{\partial u}{\partial \zeta} - w\right) + \frac{2}{\eta^2 R^2 Re}\left(\frac{\partial w}{\partial \zeta} + wcot\zeta\right) \quad (4.54)$$

$$convw = \frac{1}{R}\left(u - \eta\dot{R}\right)\frac{\partial w}{\partial \eta} + \frac{w}{\eta R}\left(\frac{\partial w}{\partial \zeta} + u\right) - \frac{2}{\eta^2 R^2 Re}\frac{\partial u}{\partial \zeta}. \quad (4.55)$$

$$convc = \frac{1}{R}\left(u - \eta\dot{R}\right)\frac{\partial c}{\partial \eta} + \frac{w}{\eta R}\frac{\partial c}{\partial \zeta}. \quad (4.56)$$

The previous equations is used to get the predicted values of velocity components and concentration, where the symbol ˜ denotes predicted value, while to get the pressure corrections, the poisson equation is discretized as follows:

$$\left(\frac{1}{R^2}\frac{\partial^2}{\partial \eta^2} + \frac{2}{\eta R^2}\frac{\partial}{\partial \eta}\right)\tilde{p}^N + \frac{1}{\eta^2 R^2}\left(\frac{\partial^2}{\partial \zeta^2} + cot\zeta\frac{\partial}{\partial \zeta}\right)\tilde{p}^N = \frac{1}{2d\tau}\left(\frac{1}{\eta R}\frac{\partial \tilde{w}^N}{\partial \zeta} + \frac{1}{R}\frac{\partial \tilde{u}^N}{\partial \eta} + \frac{2}{\eta R}\tilde{u}^N + \frac{\tilde{w}^N}{\eta R}cot\zeta\right). \quad (4.57)$$

This approach allows to use the matrix diagonalization method [93], whose computational cost is of order $n_\eta \times n_\zeta \times \min(n_\eta, n_\zeta)$, to solve the four Helmholtz-type equations (4.48), (4.49), (4.50) and (4.57) resulting from the momentum and concentration equations and the Poisson equation needed to calculate the pressure cor-

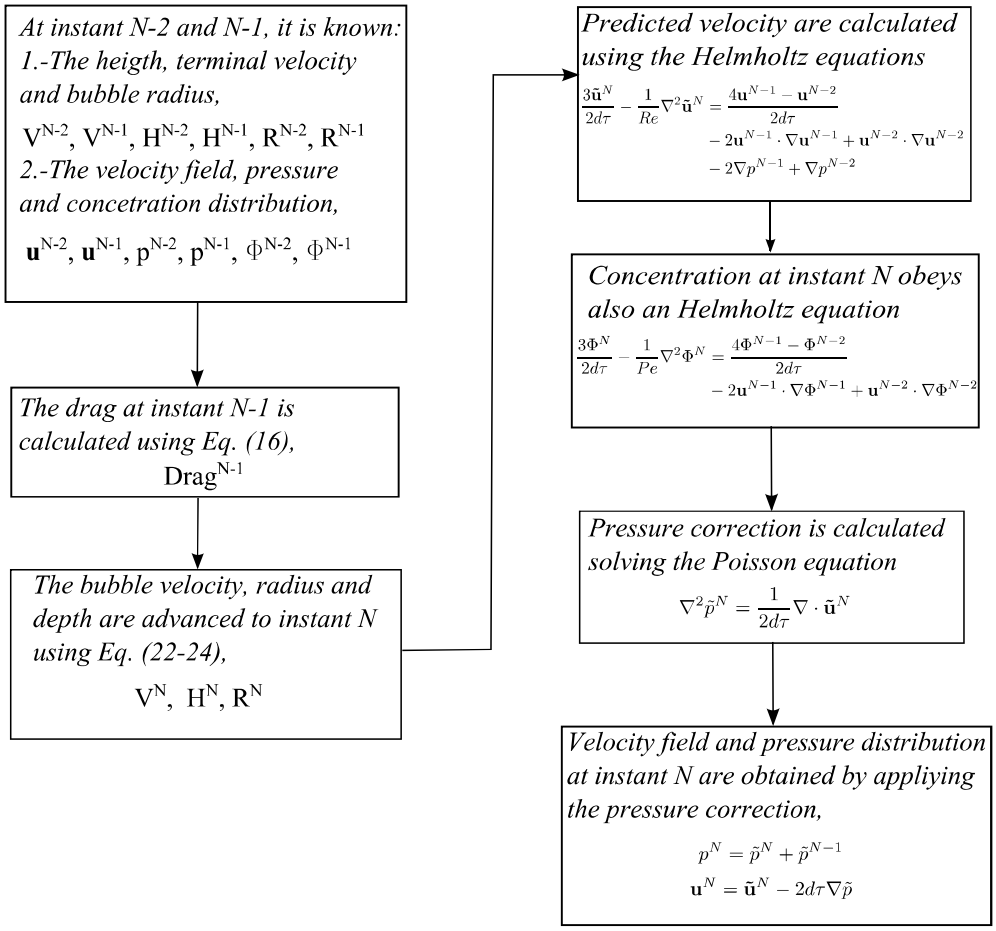

Figure 4.2: Flow chart of the numerical scheme.

rections. The nonlinear terms are evaluated using a pseudospectral method.[94] At any time, the required velocity field in the convective term of the discretized concentration equation, is obtained by interpolating the velocity field from the mechanical domain to the concentration domain using a second order interpolation operator along the η coordinate.

After getting the predicted values, the real value of $(u^{t+1}, w^{t+1}, c^{t+1}, p^{t+1})$ can be obtained by solving the additional following equations:

$$p^N = \tilde{p}^N + p^{N-1}. \tag{4.58}$$

$$u^N = \tilde{u}^N - \frac{2d\tau}{R}\frac{\partial \tilde{p}^N}{\partial \eta}. \tag{4.59}$$

$$w^N = \tilde{w}^N - \frac{2d\tau}{\eta R}\frac{\partial \tilde{p}^N}{\partial \zeta}. \tag{4.60}$$

$$c^N = \tilde{c}^N. \tag{4.61}$$

A flow chart of the numerical scheme used in the present work is depicted in Fig.4.2.

Note that both the spectral resolution used and the two different computational domains considered, allow us to use a much less number of grid points that using standards finite-differences in a single mesh. Therefore, we have carried out the numerical simulations in a grid with $n_\eta = 60$ and $n_\zeta = 25$ for the cases presented in this study. The time step employed in the simulations was $\Delta\tau = 0.005$, since no significant differences in the temporal evolution of the flow were found by using smaller time steps.

4.3 Experimental setup

4.3.1 Apparatus Configuration

It has been prepared an experimental setup in order to validate the numerical code. The experimental setup is sketched in figure 4.3. Bubbles of oxygen, liberated at the bottom of a test section filled with quiescent distilled water, ascends freely through the test section. The test section consists in a tube of 9 mm diameter and 116 cm

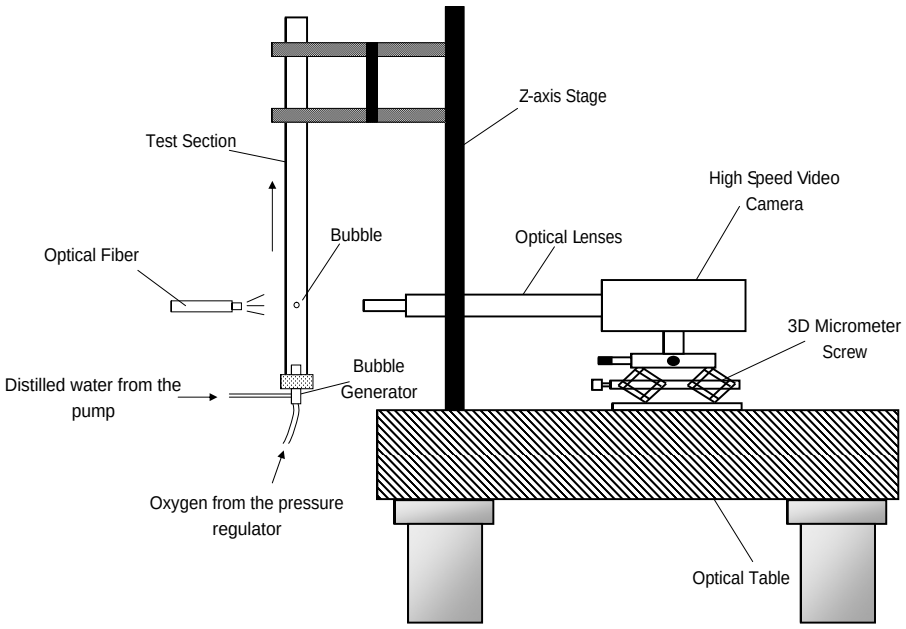

Figure 4.3: Configuration of the experiment.

long being the upper extreme of the tube open to the air. The bubble generator is a microfluidic flow-focusing device (Ingeniatrics Technologies). In the present flow focusing configuration (shown in figure 4.4), a focusing stream of distilled water is created by means a syringe pump (Harvard Apparatus PHD4400). The focusing stream pinches off the gas meniscus giving up to the oxygen bubbles. The size of the bubbles and its frequency of formation is controlled by a proper combination of the flowrate of the focusing water and pressure of the gas in the meniscus. To this end, the pressure of the gas is controlled by means of a pressure regulator (Swagelok KLF) and a digital manometer (Digitron 2003P).

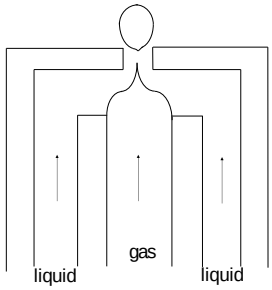

Figure 4.4: The microfluidic flow-focusing device.

The size of the bubbles is determined by analyzing its digital images. To this end, images of the bubbles are acquired using a high-speed video camera (Redlake MotionPro X4) equipped with a magnification zoom lens. The camera could be displaced both horizontally and vertically using a triaxial translation stage to focus the bubbles being them illuminated from the back by a cool white light provided by an optical fiber (Schott KL2500 LCD). The test section is supported by a z-axis stage in order to select the height's position of recording. Typical images of the bubbles at different height are shown in figure 4.5. The bubbles, although spherical, appears elliptical in the images due to the distortion created by the cylindrical geometry of the test section. So, the radius of the droplet is determined by measuring in the vertical direction. Pictures of 512x512 pixels at a rate of 5130 frames per second are recorded. This rate of recording suffices to avoid blurring images of the bubbles. Since the bubble generator does not produce perfectly monodisperse bubbles, for each height a calibration process has been made and 20 measurements of the bubble's diameter has been taken for each test section and operating conditions. We have assessed the spherical character of the bubbles in the present experimental conditions by using a square glass test chamber for some experimental runs under the same

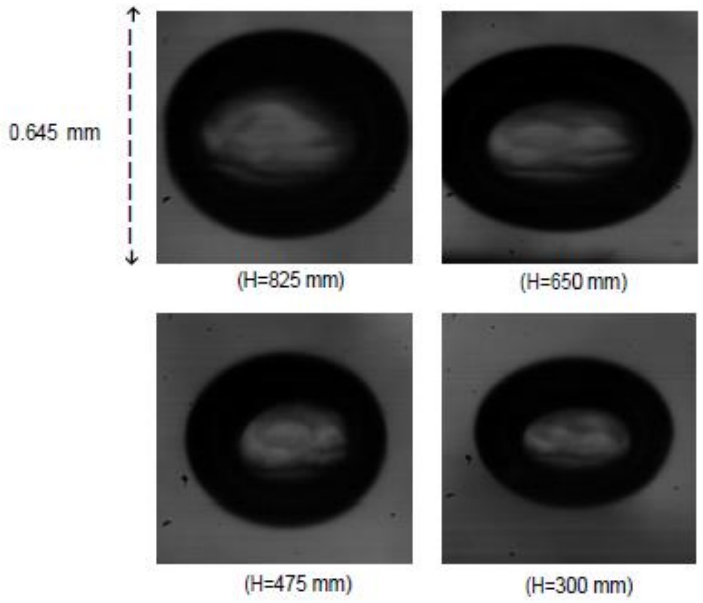

Figure 4.5: Pictures of the bubbles at different height.

operating conditions as those of the more systematic study. In these selected runs, in which any optical distortion is avoided, the maximum discrepancy between the height and the width of the bubble as measured was 3.96 μm for a diameter of 468 μm.

4.3.2 Objective and Procedures

The objective of the experiment is to relate the size of the bubble with the distance to the the free surface,i.e. the height. This relationship depends on the properties of the quiescent liquid bath. So the fist step of the experiment is to characterize the distilled water bath. To this end, prior to refill the test section, the water is agitated (with an agitator SBS ACS-161) to degas. Then, using oxygen concentration meter (A.Lab 821), it is measured the amount of dissolved oxygen in the the

water. Additionally, viscosity and surface tension are measured by means of a rotating viscometer (Brookfield DV-E) and a plate tensiometer (Krüss), respectively. Two different series has been experimented being the concentrations of oxygen of 6.15 mg/L and 8.13 mg/L, respectively. In table 4.1 are summarized the conditions and the relevant physical parameters of the two series. Table 4.1 shows the value B which is $K_H/(\rho R^* T)$, where K_H is Henry's constant and R^* is the gas constant.

Table 4.1: Experimental conditions

Experiments	I	II
$H_o\ (mm)$	825	825
$p_\infty\ (KPa)$	25	37.3
$p_a\ (KPa)$	101.3	101.3
$R_o\ (mm)$	0.269	0.21
$\mu\ (cP)$	1.1	1.1
$\rho\ (kg/m^3)$	997	997
$\gamma\ (mN/m)$	0.072	0.07
B	52.3	53.2
T (K)	297.15	298.15

4.3.3 Diffusivity, Henry's constant and the Partial pressure

To calculate the diffusivity we used the following correlation[95] based on Stokes-Einsten equation,

$$D_{O_2-H_2O} = 7.4\,10^{-8}\frac{T(\Psi_{H_2O}M_{H_2O})^{0.5}}{\mu(V_{O_2})^{0.6}}\,, \tag{4.62}$$

where T is the temperature in Kelvin, Ψ_{H_2O} is an association parameter equal to 2.26 for water [96], M_{H_2O} is the molecular weight of water, μ is the viscosity in

centipoise and V_{O_2} is the molar volume of the oxygen. The Henry's constant is determined by means of the Van't Hoff equation,

$$K_H(T) = K_H(298) \exp\left[-A\left(\frac{1}{T} - \frac{1}{298}\right)\right] \tag{4.63}$$

where Henry's constant for oxygen in water at 298 K is equal to $2.43x10^9 Pa$ (equivalent to 769.23 $\frac{L.atm}{mole}$) and A is a constant equal to 1700 for oxygen. Finally, to set the value of χ we have to realize that the upper interface is inside the test tube, and that an open gas column about $26cm$ height in the tube stands over that interface,the distribution of the partial pressure of oxygen in that column is not given by its value in the open atmosphere(i.e., $p_{p_\infty}(0) = 0.21p_a$). The reason is that a continuous flow rate Q_{O_2} of oxygen is fed through the water-air interface and discharged at the upper open end of the test tube. From a global balance(see Appendix A) we have calculated that the value of χ is approximately 0.5 with errors smaller than about 20%.

4.4 Results and conclusions

The dimensionless parameters required to carry out the numerical simulations for both series of experiments are summarized in table 4.2. It can be seen from the values in the table that in both cases the Reynolds numbers is too large to fit well the Stokes law for the drag of a sphere, (what would avoid the numerical resolution of equations (4.10), (4.11), (4.12) and (4.23)). However, the Re numbers are small enough to ensure that the fluid motion remains axisymmetric for both experiments. By the other hand, the large value of the Peclet numbers justify the employ of two

different meshes for the mechanical and the concentration problem. Note that in both experimental series, the Weber number ,$We = \rho_l U_c^2 R_o/\gamma$, is sufficiently small ($We < 1$) to assume that the bubble remains perfectly spherical.

Table 4.2: Dimensionless parameters

Experiment	Re	Pe	Fr	λ	α_1	α_2	α_3	H_o/R_o
I	52.3	$2.9\,10^4$	17.4	$1.52\,10^6$	0.90	$3.1\,10^{-5}$	0.294	3070
II	25	$1.4\,10^4$	8.34	$7.36\,10^5$	0.88	$2.8\,10^{-5}$	0.514	3930

Numerical simulations are started at the first position in the tank where we are able to measure the bubble radius R_o. In that starting point it is assumed that the velocity of the bubble is zero. However, in that position, which is about 20 cm above the position where the bubble is released, the bubble has already reached a non-zero terminal velocity which changes slowly as the radius of the bubble decreases. In our problem there are two different characteristic time scales, the time required for the bubble to reach a quasi terminal velocity, t_T, and the time required to appreciate changes in the bubble radius, t_R, being very dissimilar, $t_R \gg t_T$. Therefore, the value of the initial velocity of the bubble is not critical for the simulations. That both times are quite different for the conditions considered here it is illustrated in figure (4.6) where the numerical time evolution of the velocity of the bubble for the experimental case I is plotted. In figure (4.6a) it can be seen that the bubble starting from the rest reaches a cuasi-terminal velocity for $t = t_T \sim 0.1s$ being negligible the change of the radius of the bubble in that period, $R(t_T) \sim R_o$. In figure (4.6b) it can be seen the latter slowly evolution of the velocity once the radius of the bubble start to decreases. The numerical simulations allow to investigate in great detail how is the evolution of the flow and the concentration around the sphere at the beginning

of the process before the bubble reaches the quasi-terminal velocity. For example, figure (4.7) show contours of the dynamic pressure of the liquid around the bubble at different times. It can be seen how during this short period of time the change in the bubble radius is negligible. On the other hand, the contour of the concentration depicted in figure (4.8) show the development of a quite thin concentration boundary layer around the sphere with its corresponding wake. The correct computation of this boundary layer is critical to get an accurate value of the Smith' number S_h (equation 4.39) and, consequently, to get a good estimation of the change of the bubble radius with time (equation 4.43).

In our experimental setup the positions at which the radius of the bubble are measured are fixed. Therefore, in other to compare the experimental results and the numerical ones, it is better to plot the radius of the bubble as a function of the bubble's deep instead of plotting the radius versus the time. Note that from a numerical point of view, the time and the bubble's deep are relate through equation (4.42). The results for both case are shown in in figure (4.9). The solid lines correspond to the numerical prediction while the solid (open) symbols correspond to the experimental mean (standard deviation) values of the 20 series of experimental measurements.

To conclude, a tracking-interface numerical method was used to achieve this work. The method has been applied to study the isothermal dissolution of small single rising bubble. The key elements of the method are the use of a frame of reference moving with the bubble and the application of different meshes to solve the mechanical and mass-diffusion problems. An experiment of a small oxygen bubble rising in water has been carried out with remarkable agreement to the numerical model.

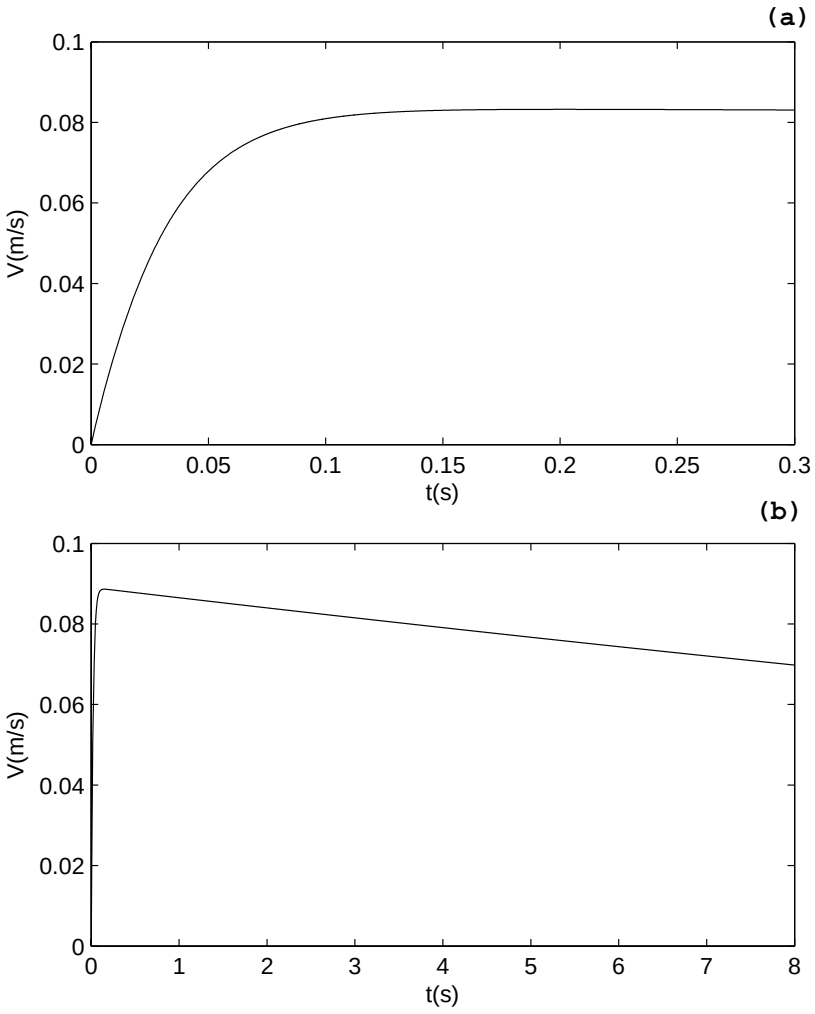

Figure 4.6: Time evolution of the velocity of the bubble for experimental series I: a) Short time evolution (time scale to reach a quasi-terminal velocity t_T); b) Long time evolution (time scale t_R)

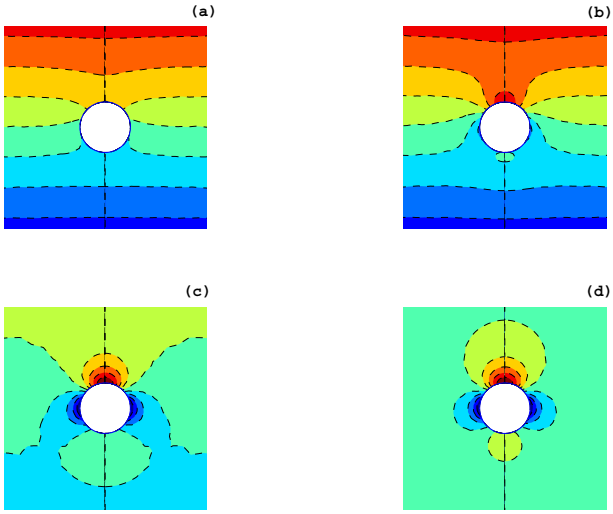

Figure 4.7: Pressure distribution around the bubble for case I at different times; a) t=0.0122 s, b) t=0.0245 s, c) t=0.0612 s and d) t=0.1224 s.

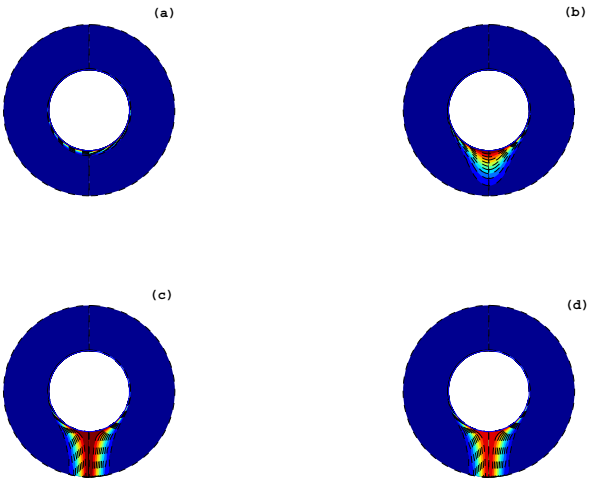

Figure 4.8: Concentration contours around the bubble for case I at different times; a) t=0.0122 s, b) t=0.0245 s, c) t=0.0612 s and d) t=0.1224 s.

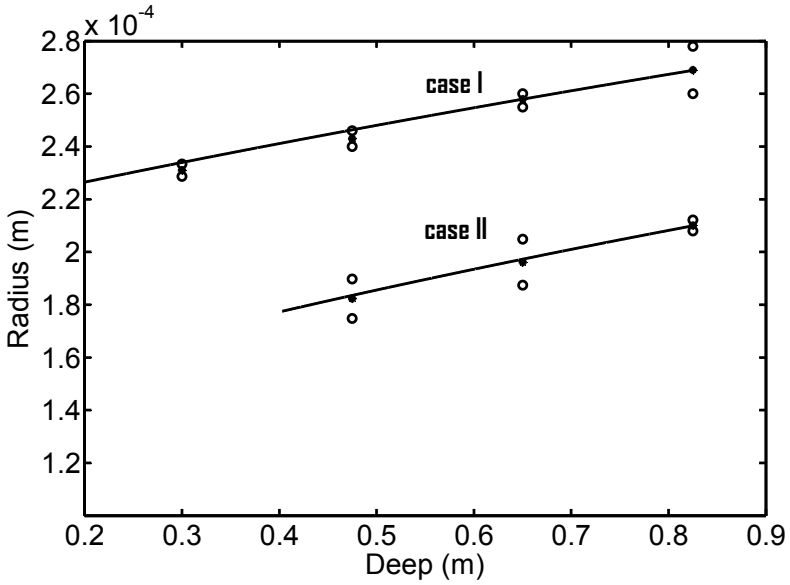

Figure 4.9: Radius of the bubble as a function of the deep for the two experiments, the solid lines correspond to the simulations results while the closed (open) circles correspond with the mean (standard deviation) experimental values.

Chapter 5

Electrical disruption of pendant liquid drops

5.1 Introduction

The study of steady cone-jets of liquids in air re-emerged vigorously in the decade of the 90 as a result of the important findings of Fenn *et al*[97]. In the wake of this impulse, Barrero *et al.* [98] showed experimentally that, the electrodispersion of conducting liquids into non-conducting liquids in the steady cone-jet mode is possible. The cone-jet, understood as a technique to produce a continuous stream of monodisperse micro(nano) droplet, broaden ,therefore, its use to new fields of interest[99]. For example, liquid-liquid cone-jet electrospraying, in accordance to low surface tension values in liquid-liquid interfaces, requires lower states of electrification to be formed being, therefore, less hazardous the handling of biological or biomedical agents[100].

Recent advances in analytical chemistry pursue minimal sample consumption by restricting the analysis to just the first droplets (or droplets) selectively withdrawn by electrical means[101]. The same selective and precise "on-demand" manipulation by electrical means is also an objective in microfluidic liquid-liquid devices[102]. It is worth, therefore, to gain a deeper insight on the physic of formation of this primary electrically generated droplet. Previous works has been conducted to study related issues. The tip streaming arising in low-conductivity drops after a step change in the electric field magnitude in a dynamically neutral atmosphere has been examined both numerically[103] and experimentally [104, 105, 106, 107, 103]. The size and charge of this primary droplet generated in air has been also object of interest. Numerical[108, 109] and experimental[109] studies have been used to derive scaling laws for this primary electrified droplet.

In the present chapter we aim to study both numerically and experimentally the dynamic of suddenly electrified droplets focusing in the dynamical role played by an non-negligible outer incompressible atmosphere. It is well known that the applied electric field plays a major role in the dynamics[110]. Not surprisingly, after the sudden onset of a subcritical electric field the more elongated equilibrium position is reached after the oscillations have died out. The supercritical dynamic is more rich and varied. Beside to the well-known tip streaming mode appears others modes shown in figure 5.3 like the *splitting* mode and the *splashing* mode. The transition from the *splitting* mode to the *tip streaming* in the case of a conducting droplet of lower viscosity than the outer dielectric medium was analyzed in previous works[111, 112]. In the present chapter we will focus in characterizing the *splashing* mode.

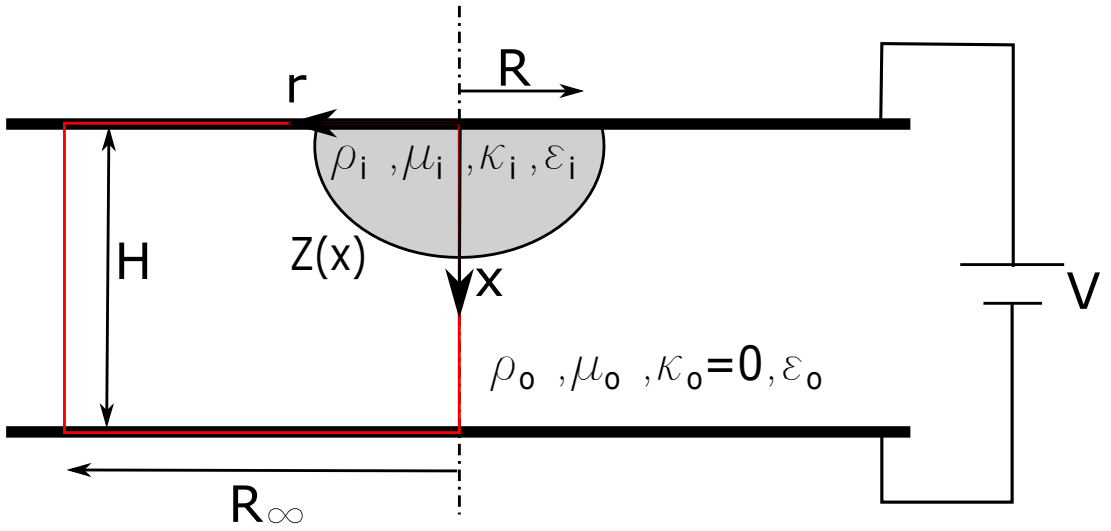

Figure 5.1: Sketch of the problem. The red box shows the computational domain.

5.2 Formulation of the problem

The geometrical and electrical configuration considered in this work is sketched in Fig. 5.1. A certain liquid droplet of volume Ω pends of a infinity plate being the rim of the droplet anchored at a distant R of the axis of symmetry. A second infinity plate is faced in parallel at the distance H. The gap between these parallel plates is filled with a second fluid immiscible with the droplet. The droplet fluid properties are the density, ρ_i, viscosity μ_i, electrical conductivity κ_i and permittivity ε_i while the corresponding properties for the surrounding phase are formed by substituting the subscript "i" by "o". Both fluids are assumed to be incompressible but the surrounding fluid is not conducting ($\kappa_o = 0$). The surface tension between fluids is denoted by γ.

At a certain instant a drop of voltage, V, (or, equivalently, an electric field $E_o = V/H$) is onset between the plates. The dynamical behaviour of the droplet

after the sudden electrification is determined by the magnitude of E_o.

5.2.1 Numerical model

5.2.1.1 Governing equations

Equations of the model below are written in dimensionless form using as characteristic quantities the outer permittivity ε_o, the rim radius R, the surface tension γ and the inner density, ρ_i. We use the EHD-Volume of Fluid (VoF) solver developed by Lopez-Herrera *et al.*[113] for the GERRIS platform[114]. This solver has been thoroughly tested in previous works[115, 103, 109]. Since VoF method treats immiscible fluids as a single one with spatially varying properties through the interface, the governing equations for both fluids writes,

$$\nabla \cdot \mathbf{v} = 0\,, \tag{5.1}$$

$$\tilde{\rho}\left(\frac{\mathbf{v}}{t} + \mathbf{v}\cdot\nabla\mathbf{v}\right) = -\nabla p + \nabla\cdot\left[\tilde{\mu}\left(\nabla\mathbf{v} + \nabla\mathbf{v}^T\right)\right] + \nabla\cdot\left[\tilde{\varepsilon}\left(\mathbf{E}\mathbf{E} - \frac{\mathbf{E}\cdot\mathbf{E}}{2}\mathbb{I}\right)\right] + Bo\,x + \delta_s\zeta\mathbf{n} \tag{5.2}$$

and

$$\nabla\cdot(\tilde{\varepsilon}\nabla\varphi) = -q \quad \text{with} \quad \mathbf{E} = -\nabla\varphi\,, \tag{5.3}$$

where $\mathbf{v}(\mathbf{x},t)$, $p(\mathbf{x},t)$ and $\varphi(\mathbf{x},t)$ are the velocity field, pressure distribution and electric potential in the computational domain, respectively. $\mathbf{E}$ is naturally the electric field. The gravitational forces, orientated in direction x, results, after non-adimensionalization, in the Bond number $Bo = \rho_i g R^2/\gamma$. The third term in the r.h.s of Eq. (5.2) corresponds to the electric stresses and results of applying the divergence of the Maxwell stress tensor where $\mathbb{I}$ denotes the unity tensor.

The last term in the momentum equation (5.2) corresponds to the surface tension term that acts only at the interface (δ_s is the Dirac delta). $\mathbf{n}$ denotes the unitary vector normal to the interface being ζ the interface curvature. $q(\mathbf{x},t)$ is the dimensionless volume charge density that obeys to the conservation equation,

$$\frac{q}{t} + \nabla \cdot (q\mathbf{v}) = \nabla \cdot (-\tilde{\kappa}\mathbf{E}) \,. \tag{5.4}$$

Observe that q has only sense in the inner conducting fluid phase being strictly zero in the outer fluid phase given its dielectric (non-conducting) nature.

$\tilde{\rho}(\mathbf{x},t)$, $\tilde{\mu}(\mathbf{x},t)$, $\tilde{\varepsilon}(\mathbf{x},t)$ and $\tilde{\kappa}(\mathbf{x},t)$ stand for the spatial varying dimensionless fluid properties, density, viscosity, electrical permittivity and conductivity, respectively,

$$\tilde{\rho} = \Psi + \rho_r(1-\Psi) \,, \tag{5.5}$$

$$\tilde{\mu} = C_\mu(\Psi + \mu_r(1-\Psi)) \,, \tag{5.6}$$

$$\frac{1}{\tilde{\varepsilon}} = \frac{1}{\beta\Psi} + \frac{1}{1-\Psi} \,, \tag{5.7}$$

and

$$\tilde{\kappa} = \alpha\,\beta\,\Psi \,. \tag{5.8}$$

being ρ_r and μ_r the outer to inner ratio of densities and viscosities, respectively, $\rho_r = \rho_o/\rho_i$ and $\mu_r = \mu_o/\mu_i$. C_μ is the Ohnesorge number based on the inner fluid properties, $C_\mu = \mu_i/(\rho_i R\gamma)^{1/2}$. β is the relative permittivity, $\beta = \varepsilon_i/\varepsilon_o$. α is the relaxation parameter[116], $\alpha = (\kappa^2 R^3\rho_i/\gamma\varepsilon_i^2)^{1/2}$. Note that α coincides with the ratio of the capillary time $t_c = (R^3\rho_i/\gamma)^{1/2}$ to the electrical relaxation time $t_e = \varepsilon_i/\kappa_i$. Finally, $\Psi(\mathbf{x},t)$ is the volume fraction that serves to track the interface position.

$\Psi(\mathbf{x}, t)$ is governed by the equation,

$$\frac{\Psi}{t} + \nabla \cdot (\Psi \mathbf{v}) = 0\,. \tag{5.9}$$

5.2.1.2 Computational domain and boundary conditions

Profiting of the axisymmetric character of the problem, the computational domain has been restricted to the red rectangle $(H/R) \times (R_\infty/R)$ shown in Fig. 5.1. Trying to reproduce as much as possible the experimental setup described below we have set H/R to 4.29 and R_∞/R has been fixed to 8.6. We have checked that the enlargement of the computational domain ($R_\infty > 8.6R$) does not have sense since the dynamic of the droplet is unaffected. The degree of the electrification level is measured by the dimensionless electric field, χ given by,

$$\chi = \left(\frac{R\varepsilon_o E_o^2}{\gamma}\right)^{1/2}, \tag{5.10}$$

Therefore, this electrification level is obtained by imposing a constant dimensionless voltage to the upper plate equal to $\varphi(0, r; t) = H\chi/R$ while the downstream plate is kept grounded.

Far away of the droplet, at the boundary $r = R_\infty/R$, the voltage drop is assumed to be linear and the fluid velocity is considered negligible.

Known the density of the fluids, ρ_o and ρ_i, and the volume of the inner fluid Ω, it is calculated the dimensionless position of the interface, $r = Z(x)$, imposing equilibrium between gravitational/buoyacy forces and surface tension forces and the

conservation of the liquid volume,i. e.

$$Bo^{rel}\, x + \frac{1}{\sqrt{1+Z'^2}}\left(\frac{1}{Z} - \frac{Z''}{1+Z'^2}\right) = cte \quad \text{together with} \quad \frac{3}{2}\int Z^2(x)\, dx = \frac{\Omega}{(2\pi R^3/3)} = \vartheta \tag{5.11}$$

where the prime denotes differentiation respect x and Bo_r is the reduced Bond number $Bo^{rel} = (\rho_i - \rho_o)gR^2/\gamma$ and ϑ is the dimensionless volume. This calculated dimensionless interface position, $Z(x)$ is used as initial condition for the VoF calculations.

5.2.2 Experimental setup

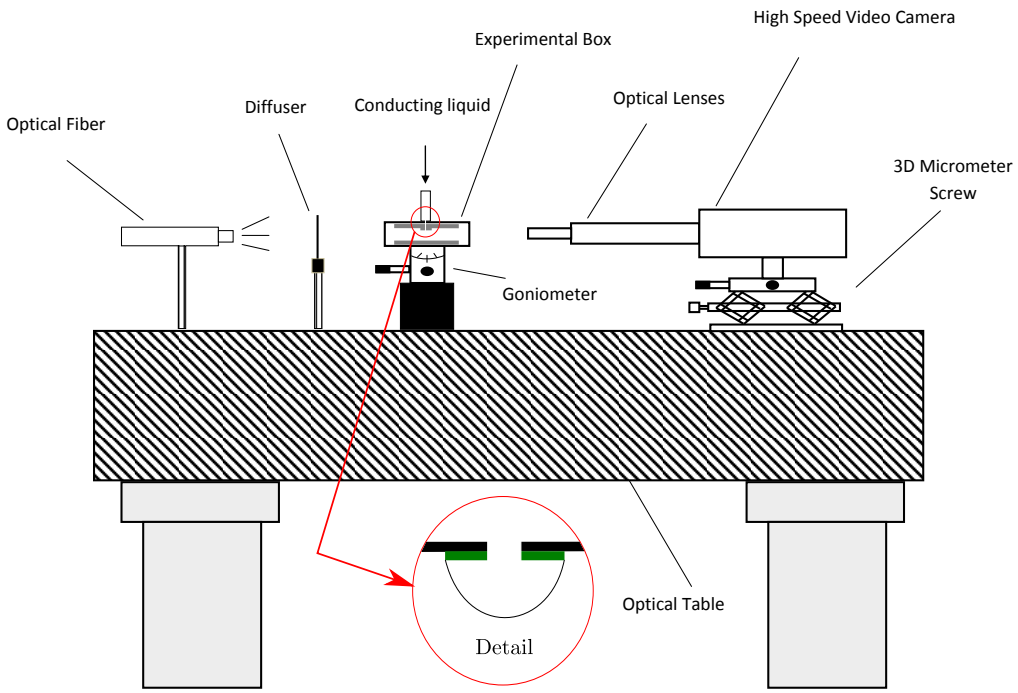

Figure 5.2: Experimental setup with detail of the fluid box.

A series of experiments were done by using the apparatus illustrated in figure

5.2. The setup consists of a polymethyl methacrylate box with glass windows at sides. Two parallel circular electrodes of radius $R_{plate} = 4.5cm$, made of brass, were placed at the top and the bottom inside the box. The distance between the parallel plates is $H = 10.3mm$. At the center of the upper electrode, a brass disk of radius $R = 2.4mm$ and thickness $h = 0.8mm$ was attached (depicted in green in the detail of figure 5.2). This brass disk serves to provide a cleared edge where the triple contact line could anchor. A circular orifice of radius $r = 0.1mm$ was made at the center of the disk and the upper electrode. A syringe pump (Harvard Apparatus PHD4400) was used to introduce the conducting liquid through the orifice. The upper electrode was connected to DC high voltage power supply (Bertan 205A-10R) and the lower electrode was connected to the ground. The power supply can apply a voltage difference of 10 kVolts. Images were captured at 16000 frame per second by using high speed video camera (Shimadzu HPV-2) with an optical magnification lens (Optem 301200). Another camera (Redlake MotionPro X4), perpendicular to the first camera, with an optical magnification lens (Navitar 1-60123), was used also to acquire images at 5130 frame per second from another direction (not shown in figure 5.2). Double on/off switch was used to synchronize between applying the voltage and recording the images. The complete droplet ejection lasts for about 10 microseconds since the onset of the voltage. Both cameras could be displaced both horizontally and vertically using a triaxial translation stage to focus on the drop. These are back-illuminated by a cool white light provided by an optical fiber (Schott KL2500 LCD) and a light source (WalimexPro VC-600) for both cameras respectively. A diffuser was placed between the optical fiber and the box to provide uniform lighting. All the equipment described was mounted on an optical table.

In each experiment, the conducting liquid was injected through the orifice to

form the pendant drop with the desired volume. The dielectric liquid was poured into the box to surround the pendent drop. Both cameras were used in order to make sure that the drop anchored ideally with the disk edge. We wait for 2 min. to let the drop relax. Then, after switching on the power supply, the double on/off switch was turned on to apply the desired voltage and to acquire images at the same time. The first camera (Shimadzu HPV-2) was used to acquire images of the jet neck with a frame covering an area of about $3.9 \times 3.25\, mm^2$. The second camera (Redlake MotionPro X4) was used to capture images of the jet nucleation position with a frame covering an area of about $5.88 \times 5.88\, mm^2$. To calculate the initial volume of the drop, jet neck and the jet nucleation position, the images was processed to detect the free surface contour by using a commercial program (ImageJ). In this study, pure water, a mixture of methanol+ 5% wt pure water and ethylene glycol were used as conducting liquids. While, Silicone oils of 5, 20, 100 and 10000 cSt were used as Dielectric liquids. The interfacial tension between liquids that were used in the different experiments with their corresponding temperature are indicated in table 5.1. The rest of physical properties are listed in table 5.2.

Table 5.1: Interfacial tension

Conducting Liquid	Dielectric Liquid	$\gamma\ (mN/m)$	T (K)
Methanol+5% wt water mix.	Silicone oil(5cSt)	2.69	292
Pure water	Silicone oil(5cSt)	46	289
Pure water	Silicone oil(20cSt)	46	289
Pure water	Silicone oil(100cSt)	46.2	289.4

The position of the interface has been determined with an subpixel image processing technique[117, 118]. Briefly, the technique consists in two-stage procedure;

in the first stage, a set of pixels probably pertaining to the contour are selected. In the second stage, the accuracy of the detected contours was improved to the sub-pixel level by analyzing the gray intensity profile along the direction normal to the contour.

Table 5.2: Physical properties

Liquid	$\rho\ (kg/m^3)$	$\mu\ (cP)$	$K\ (S/m)$	β
Methanol+5% wt water mix.	804	1.038	$9.05x\,10^{-5}$	–
Pure water	997	1.33	$1.8x\,10^{-5}$	–
Ethylene glycol	1110	21	$3.1x\,10^{-5}$	–
Silicone oil(5cSt)	905.2	5.37	–	2.59
Silicone oil(20cSt)	947.15	18.9	–	2.68
Silicone oil(100cSt)	957.12	95.7	–	2.8
Silicone oil(10000cSt)	973.9	9739.2	–	2.8

5.3 Results and discussion

Basaran & Scriven[110] determined that only below a certain threshold value of the electric field an equilibrium position is possible. In effect, subcritical value of electric field results in more elongated equilibrium position that it is reached after a damped oscillation[119, 120]. On the other hand, in air, with supercritical values, the droplet goes unstable in a two stages process[103]: (i) a quasi-equilibrium slow stretching of the droplet in which electric force barely overcome capillary forces (ii) a very fast jetting stage where a microjet is emitted. However, if the outer medium is not, from the dynamic point of view, negligible, the droplet dynamic can be more complex. Beside to the tip streaming mode appears others modes shown in figure

5.3 like the *splitting* mode and the *splashing* mode. We have not pursued in the present work an exhaustive parametrical mapping of the different modes. We have observed, however, that the onset of the different breakup modes depends mainly on the viscosity of the outer medium. Tip streaming regime typically appears if the viscosity of outer medium is low. It will appear with whipping if the inner medium is very viscous. The splashing mode is predominant for moderate outer viscosity (for the oils tested: 5 and 20 cSt). The splitting mode is characteristic of very high viscosity (10000 cSt). Interestingly, for intermediate viscosities (100 cSt in our case), the observed mode is, often, neither a pure splitting mode nor the splashing mode but a mix of both. The droplet seems to break in the splitting mode but before the pinching were completed, the daughter drop breaks in a splashing mode.

We will focus in next sections first, briefly, in the subcritical regime and later, in the *splashing* mode.

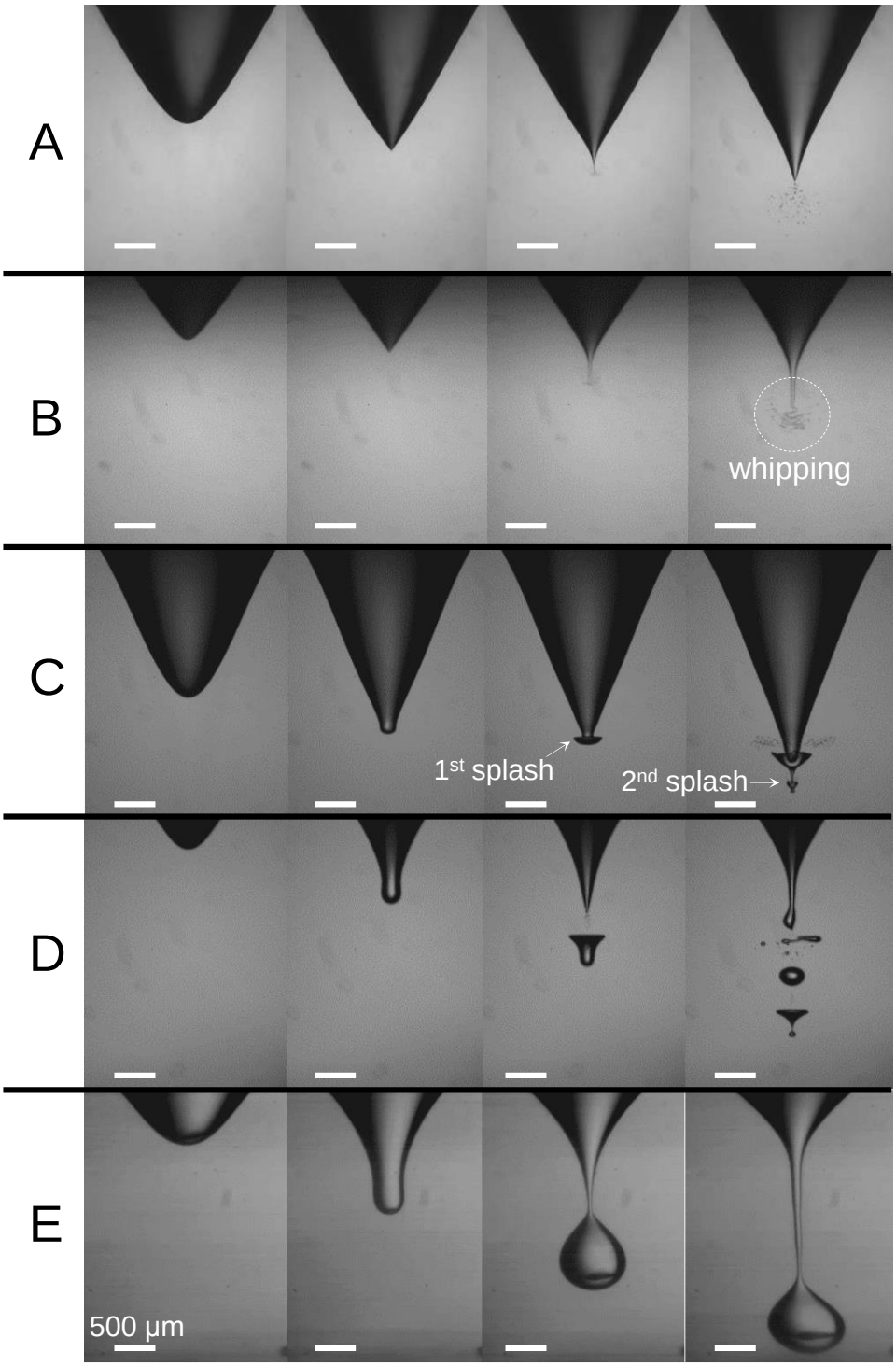

Figure 5.3: Different modes of droplet disruption: (A) and (B) tip streaming mode without and with whipping instability. respectively; (C) splashing mode, (D) split-splashing mode and (E) splitting mode.

5.3.1 Subcritical regime

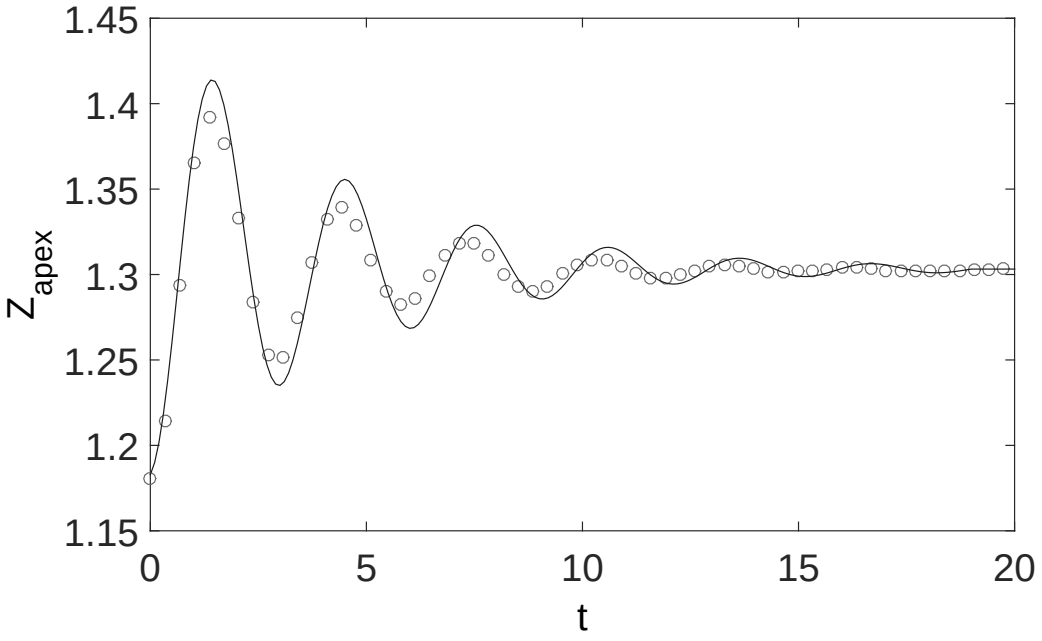

Figure 5.4: Temporal evolution of the dimensionless apex position $Z(t)$ for $\vartheta = 1.26$, $C_\mu = 4.1 \times 10^{-3}$, $Bo^{rel} = 2.254$, $\chi = 1.46$, $\rho_r = 0.912$, $\mu_r = 4.54$. The symbols and solid line are the experimental and the numerical results, respectively.

The liquid flow in the equipotential drop is originated by the appearance of electric stresses at the free surface. Both the electric charge density and the electric stress reach their maximum values at the apex. The electric stress is balanced by the hydrostatic and capillary pressures (viscous stresses normal to the free surface can be generally neglected). Therefore, the reduced pressure decreases at the apex,

and the liquid is suctioned towards that region. This liquid motion stretches the drop, increasing the free surface curvature at the apex. Consequently, a restoring capillary force appears in that region. If the electric stresses are not high enough to overcome the surface tension force, then the drop reaches a new equilibrium state. In principle, the new equilibrium shape could be reached through either an overdamped extensional deformation or the damping of free surface oscillations. Figure 5.4 shows the temporal evolution of the apex position, Z_{apex}, of a subcritical drop.

5.3.2 Supercritical regime: The *splashing* mode

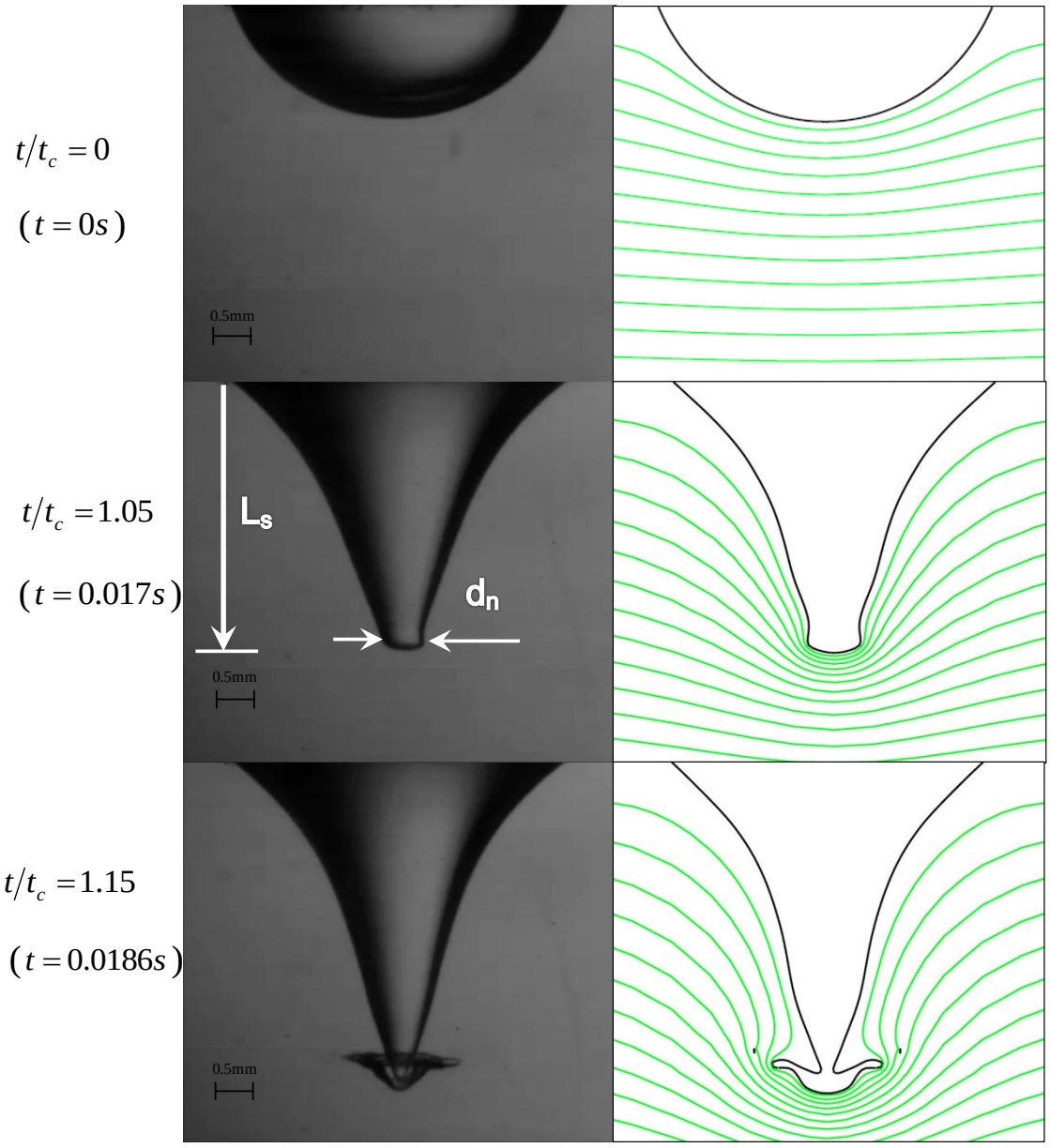

Figure 5.5: The droplet splashing at different stages. The right column shows the numerical predictions. Green lines correspond to electric isopotential lines. Dimensionless values for this case are: $\vartheta = 0.64$, $C_\mu = 4.1 \times 10^{-3}$, $\chi = 0.39$, $\rho_r = 0.908$ and $\mu_r = 4.04$.

Different instants of a droplet breaking in the splashing mode are shown in figure 5.5. The splashing mode is characterized by two stages: (i) the droplet is slowly stretched in axial direction up to a certain neck radius, d_n (and length, L_s) is reached (ii) the front of the droplet, then, expands faster in radial direction that in axial direction forming a jellyfish splashing structure. The characteristic time for both stage is similar. Interestingly, in some cases this "jellyfish" splashing structure is repeated in cascade (see figure 5.3, C).

At first glance, the early stage of axial stretching is common in all modes. This first stage is essentially the result of the competition between the electric pressure and surface tension being the drop regarded as equipotential. However, the second stage is radically different in tip-streaming mode and splashing mode from the electrical point of view. While the jetting in the tip streaming can be seen as a consequence of the finite conductivity of the fluid[121, 103], the splashing occurs in times of the order of the capillary time behaving the fluid as equipotential since electric relaxation time is much shorter. Consequently, the conductivity and permittivity of the inner fluid are unimportant in the splashing mode. We have assessed the conducting character of the fluid by means of the numerical computations (see electric isopotential lines in figure 5.5).

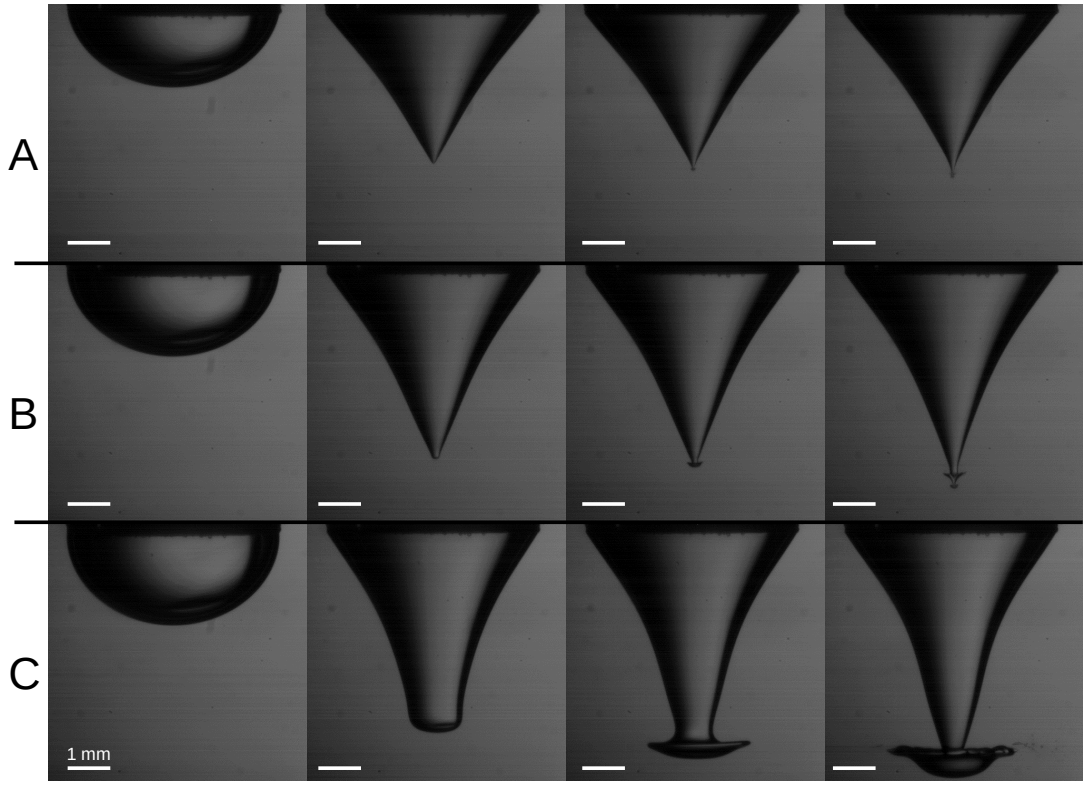

Figure 5.6: Effect of droplet volume on splashing size: (A) $\Omega = 17.77mm^3$ (B) $\Omega = 21.28mm^3$ (C) $\Omega = 25.35mm^3$.

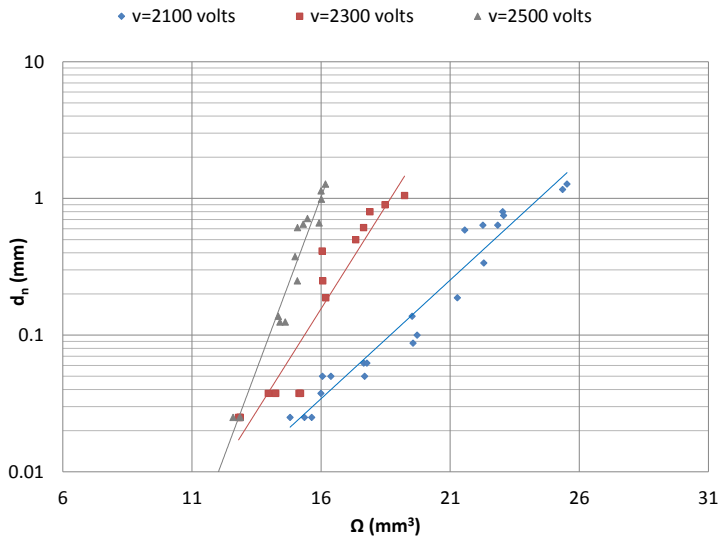

Figure 5.7: Neck diameter Vs. droplet volume for voltage $2100, 2300$ and 2500.

Some other differences can be pointed out between the modes tip-streaming and splashing. Tip streaming is of local (and universal) nature. The ejected jet obeys to universal scaling laws based on the liquid properties[108, 103, 109] being independent of large scale variables as the applied voltage, the droplet radius or the particular geometrical configuration used (pendant from a plate, levitating or pending from a needle, for example). On the contrary we found that either the applied voltage and the droplet volume affect the form of the splashing. This effect can be seen clearly in figure 5.6. Also, figure 5.7 shows the change of the neck diameter d_n with the droplet volume Ω and the applied voltage V. These large scale variables have the same effect on other modes (Split-Splashing and Splitting).

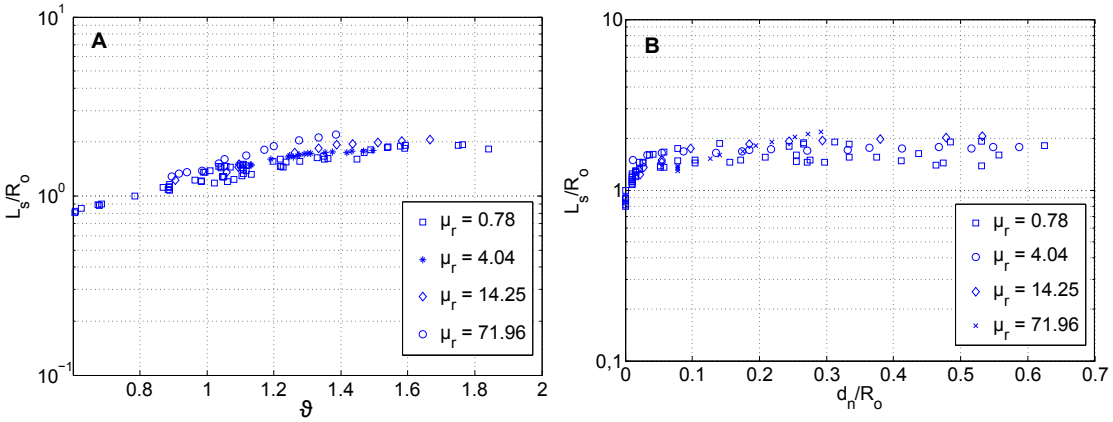

Figure 5.8: Non dimensional splash length, L_s/R, versus: (A) The dimensionless volume, ϑ, (B) the dimensionless neck diameter, d_n/R. Experiments shown cover two orders of magnitude of the viscosity ratio, $\mu_r \in [0.78, 71.96]$.

Moreover some interesting remarks arise from experimental data. In figure 5.8 we plot the dimensionless splash length, L_s/R, as a function of the dimensionless volume ϑ (subplot A). In subplot B it is explored the relationship between the splash length and the neck radius. A first aspect worth to be noted is the negligible influence of the outer viscosity in the splashing process. The reason for this negligible effect of the viscosity ratio can be attributed to the relatively large characteristic hydrodynamic time of the process. Despite the high values of the outer viscosity the splashing developing is slow enough to have unimportant outer viscosity forces compared to electric or capillary ones. The effect of the outer medium is, some how, paradoxical, the splashing mode develops because the outer medium is not negligible from the dynamic point of view, but experiments shows that the outer viscosity is trivial in the formation of the splashing. On the contrary, it would expect that the density ratio ρ_r were significant in the process. However, it is difficult to verify this point

experimentally since the density ratio can not be varied too much with the present experimental setup. It seems also to exist a decoupling between the splashing length and the neck radius (see figure 5.8, subplot B). Summarizing, experiments suggest that the splash length is an only function of the dimensionless volume ϑ.

The dimensionless neck radius has to be, necessarily, a function of all the dimensionless parameters governing the problem,

$$\frac{d_n}{R} = f(\vartheta, \chi, C_\mu, \rho_r, \mu_r, \beta, \alpha, H/R), \quad \text{i.e.} \tag{5.12}$$

the dimensionless volume, electrification level, inner viscosity; relative density, viscosity and permittivity; electrical conductivity and distance between plates, respectively. Since we claim (supported by the numerical simulations) that the droplet can be assumed equipotential along the first stages of the splashing, either the relative electrical permittivity β and dimensionless conductivity, α, are irrelevant. Also, since the experimental setup is fixed and the ratio of densities in our experiments are very close to the unity either the width of the gap H/R and the relative density can be also safely dismissed in relation (5.12). Finally, we assume that the relative viscosity μ_r, as in the case of the splash length, is negligible. Thus, the relation (5.12) reduces to,

$$\frac{d_n}{R} \simeq f(\vartheta, \chi, C_\mu) = f(\vartheta^{1/3}\chi^{2/3}C_\mu^{-1/5}). \tag{5.13}$$

In the above functional relationship (5.13) we have assumed that the dimensionless neck radius scales with the single parameter, $\vartheta^{1/3}\chi^{2/3}C_\mu^{-1/5}$ being the exponent those that better suited the experiments. In figure 5.9 we plot the dimensionless neck radius as a function of the scaling proposed in relation (5.13) using the same data

of figure 5.8.

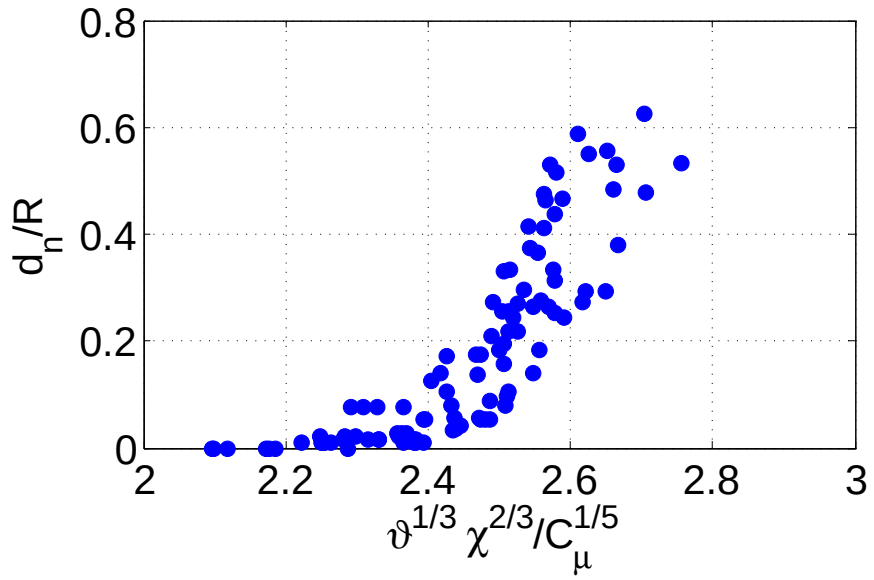

Figure 5.9: Non dimensional splash neck radius, d_n/R, versus the scaling $\vartheta^{1/3}\chi^{2/3}C_\mu^{-1/5}$.

5.4 Conclusions

To conclude, intensive experiments have been carried out in order to study all parameters that could affect on the electrical disruption of pendant conducting liquid drop in a dielectric liquid. Various conducting and dielectric liquids have been used to study the inner and outer, liquid medium properties, effect on our drop dispersion. Experiments have showed two regime; subcritical regime, when the drop oscillate to a stable equilibrium position just like in the case of surrounding air atmosphere. The second one is a supercritical regime, when the electrical force overcome cap-

illary forces and a very fast microjet is emitted. The last behaviour is known as tip streaming mode. But, our results show that this is not the only mode in the super-critical regime. We have found out that other modes are exist. With changing the outer medium viscosity three more modes have been revealed. With low outer medium viscosity appears tip streaming mode. Splashing mode is shown when the outer viscosity is moderate (5 and 20 cSt). Split-Splashing is observed with high viscosity (100 cSt). While, with very high viscosity (10000 cSt) appears the splitting mode. Numerical model has been made to simulate the behavior of the electrified pendant drop. A great agreement was observed between the experimental and numerical results. Depending on massive experimental results, a scaling law has been obtained to characterize the neck diameter in the splashing mode. It was found that the neck diameter in the split-splashing mode also obey the scaling law. This study has a great importance. It is not only helping to get a better understanding of an interesting topic like liquid-liquid dispersion, but also it estimates the threshold limitation of producing micro-droplets in another liquid considering the conducting and the dielectric liquid properties. Estimating such limitation has a great impact on application like micro-encapsulation.

Chapter 6

Small drops from large nozzles

6.1 Introduction

In this chapter, we present experimental and numerical study on a novel technique to produce drops smaller than the nozzle from which they are produced. In drop on demand (DOD) technology, it has been a major limitation to generate small drops. The only way known was to reduce the radii of the nozzle [122, 123, 124, 125, 126, 127, 128]. Many problems arise in commercial systems that depend on this method. Beside complexity of fabricating such small nozzles, the nozzle could be subjected to clogging. Alvin U. Chen and Osman A. Basaran [129] were managed to produce drops 50% smaller in radii than those of nozzles. This could be achieved by carefully controlling capillary, viscous and inertial time scale. They produced such drop's size by using squeeze mode DoD glass nozzle (see figure 6.1). The main idea is to introduce pull-push-pull waveform pulse (see figure 6.2) in order to suppress the formation of the large primary drop that could be produced by using only pull-push waveform pulse. This technique is limited. It is not able to form small drops if the

viscosity is too small or too large.

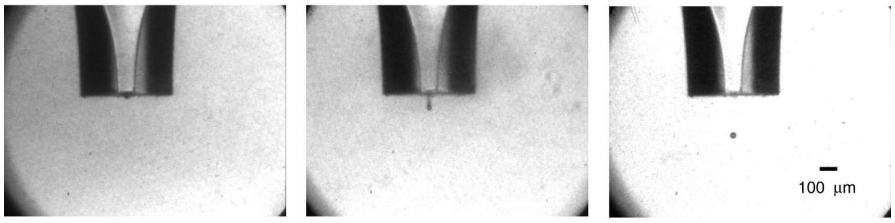

Figure 6.1: Squeeze mode DoD nozzle [129]

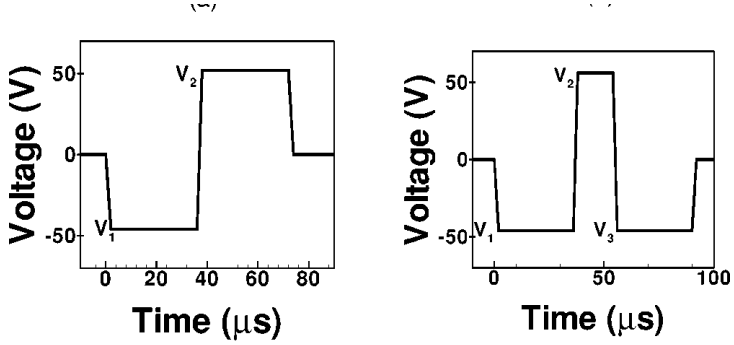

Figure 6.2: pull-push and pull-push-pull waveform pulse [129]

A.A. Castrejón-pita *et al.* [130] have presented another method to produce drops smaller than the nozzle. Rather than using squeeze made glass nozzle, they used another configuration called Large-Scale system (LS). The system consists of a cylindrical reservoir and two endplates. One plate is a thin metal sheet with a small orifice in the center, which acts as the nozzle. The other end consists of a piston which act as the driving inertial force (see figure 6.3-up). The key in this system is to apply a negative pulse which forms a cavity near to the nozzle. Then, the cavity collapse forming a thin and fast jet. Later a small drop as the same size of the jet separates and the jet go back to the reservoir (see figure 6.3-down). This system is able to

produce droplets loaded with particles. Also, it has a wider region, in which droplets can be generated, than other conventional methods (see figure 6.4). In this chapter, series of experiments and numerical simulation have been carried out on the later system (LS) in order to study the effect that the pulse amplitude, pulse width and liquid properties have on the final droplet size.

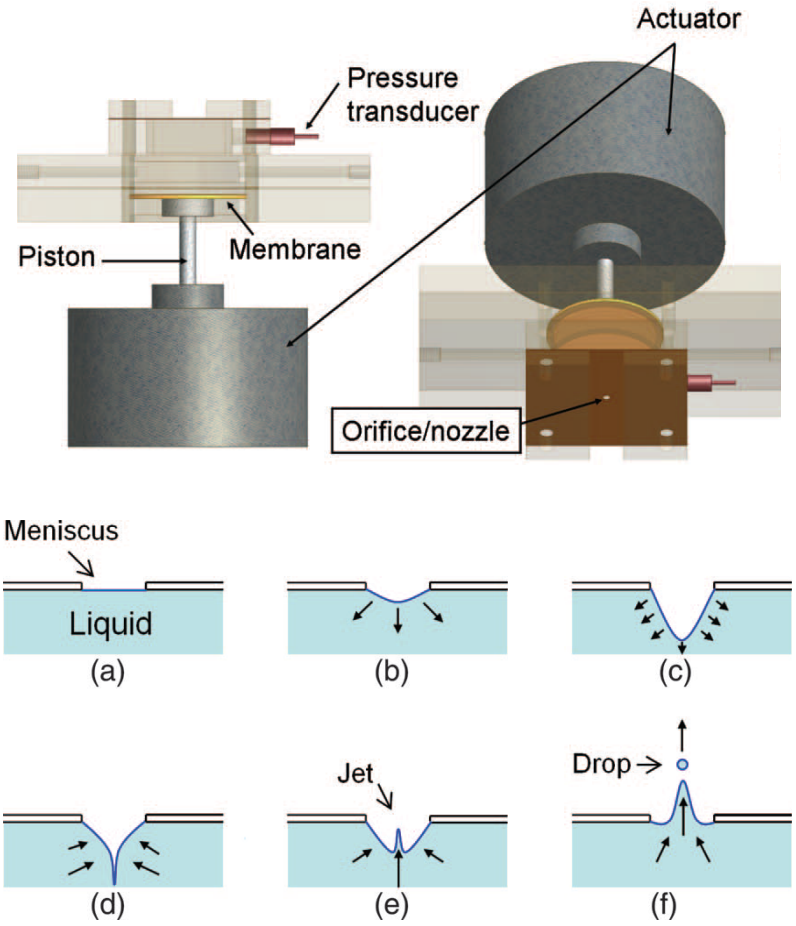

Figure 6.3: Configuration of (LS) prototype and it's jetting process [130]

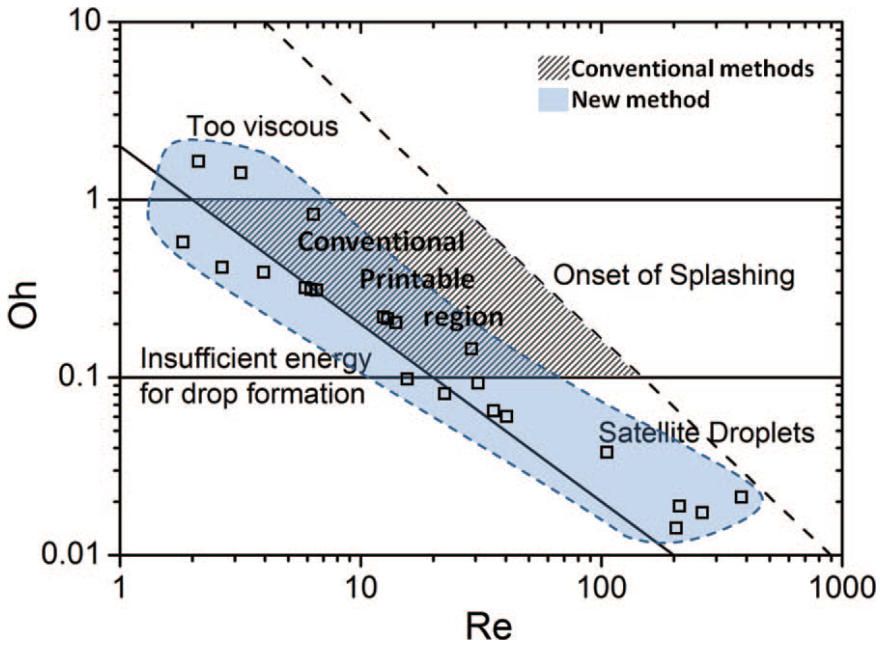

Figure 6.4: Region in which droplers can be generated [130]

6.2 Experimental setup

In order to study the effect that the pulse amplitude, pulse width and liquid properties have on the final droplet size (d), generated by the novel method, series of experiments were carried out on print-head prototype "large-scale system" (LS) [130]. It consists of a cylindrical reservoir made from polymethyl methacrylate with a diameter $D = 30mm$ and two endplates with a distance in between $H = 20mm$. One plate is a thin brass sheet of thickness $t = 0.25mm$ with an orifice in the center of radius $R_0 = 1mm$. The other end consists of a piston which moves by the action of an elecromechanical actuator (YMC MS-20) which in turn is driven by simple pull-mode sine pulses. The working liquid is introduced into the reservoir through a tube connected to a syringe exposed to the atmosphere. The syringe can

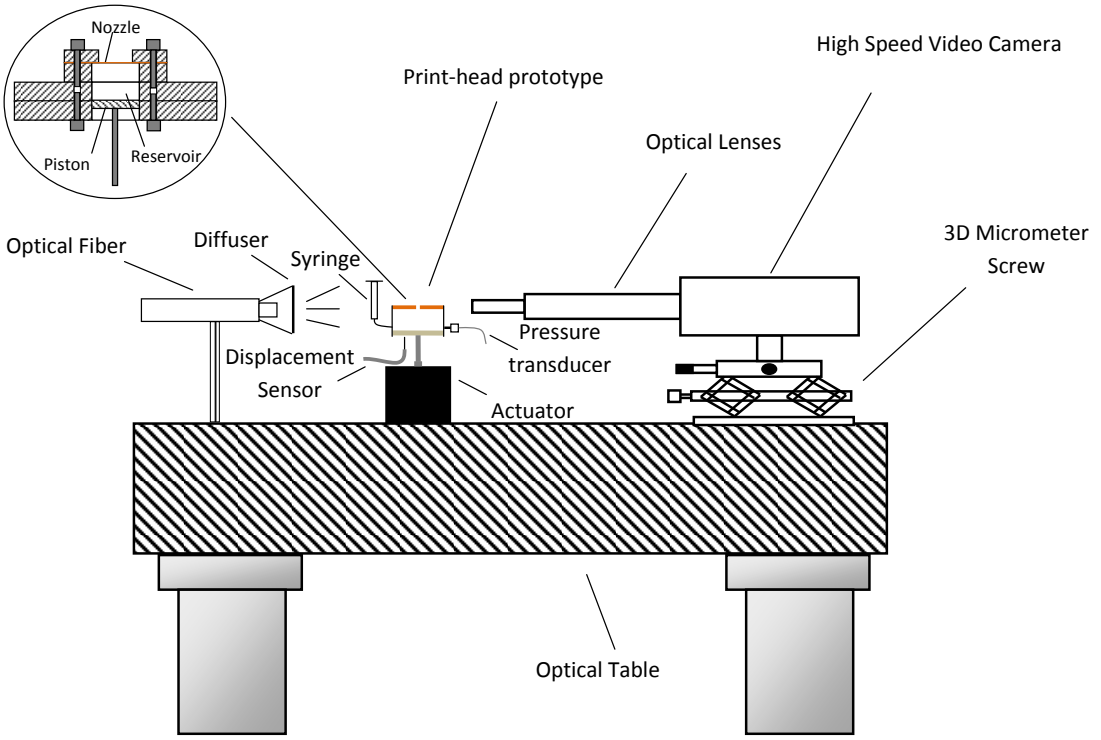

Figure 6.5: Experimental setup

move up and down in order to fill the reservoir and attach the interface meniscus to the orifice border. To provide the actuator with the signal pulse, data acquisition card (National Instrument USB X Series) connected to PC and integrated amplifier (ROTEL RA-921) were used. In order to control our experiment, fiber optic displacement sensor (D6-C1H1) and pressure transducer (Honeywell 40PC001B) were used to measure the displacement of the piston and the pressure inside the reservoir respectively. They were both connected to the data acquisition card in order to visualize the displacement and the pressure with the time on LabView program. Images were captured at 50000 frame per second by using high speed video camera (Phantom V12.1) with an optical lenses (Navitar 1-62922). The high speed video

camera was used to acquire images of the cavity collapse, the jetting and the droplet separation with a frame covering an area of about $5.12 \times 8\,mm^2$. To calculate the diameter of the drop, the images were processed to detect the free surface contour by using a commercial program (ImageJ). The camera could be displaced both horizontally and vertically using a triaxial translation stage to focus on the drop. It is back-illuminated by a cool white light provided by an optical fiber (PhotoFluor II). A diffuser was placed between the optical fiber and the prototype to provide uniform lighting. All the equipment described was mounted on an optical table (see experimental setup in figure 5.2).

6.3 Numerical simulations

Numerical simulations of the print-head configuration illustrated in figure 6.6 have been performed. The mass continuity, momentum conservation, and liquid volume fraction equations for the incompressible regime were resolved by the finite-volume scheme implemented in the commercial solver FLUENT14.0. It was assumed a uniform velocity distribution at the inlet which corresponds to the velocity of the piston v_p. A uniform pressure distribution was prescribed over the outlet section, which was located sufficiently far away from the nozzle. Also, Nonslip boundary conditions were imposed at the solid walls.

To reduce the computing time, axisymmetric plane of the fluid configuration was simulated. It was used mesh consisting of 286 792 rectangular cells with different side lengths from 500 to $5\mu m$ to spatially discretize the equations. The fine mesh has been used in the interface region to avoid numerical diffusion of the interface.We checked that with this refinement our results become practically independent of the

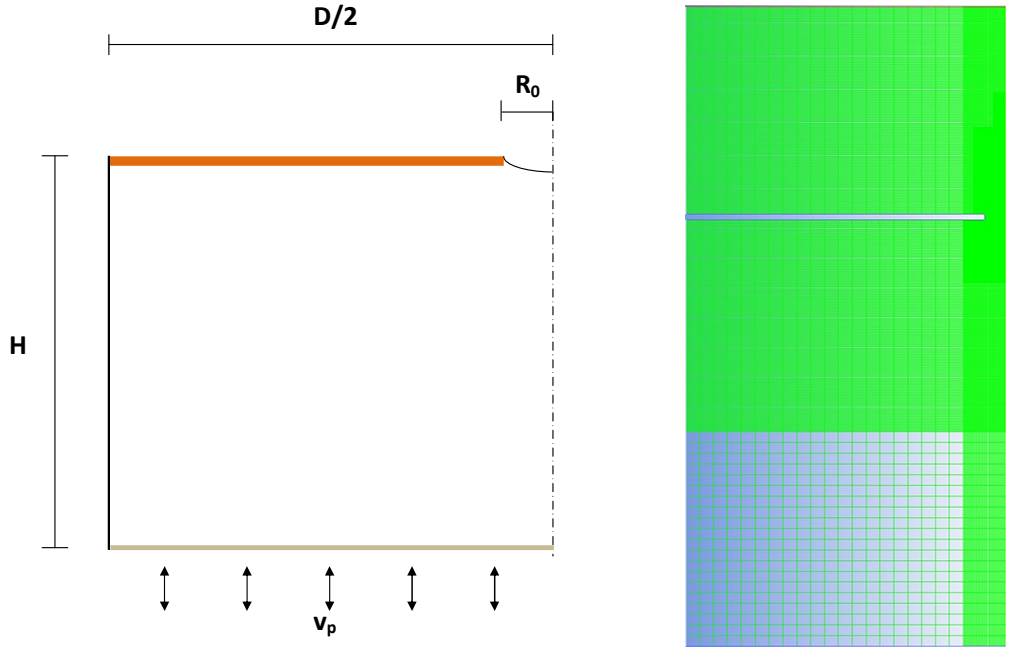

Figure 6.6: Simulation domain and numerical mesh

mesh size. The interface between the two phases was tracked by solving a continuity equation for the volume fraction of one of the phases.

This calculation was performed by using an explicit time-marching scheme, while the rest of the equations were solved implicitly. The time step Δt was sufficiently small to ensure that the global Courant number $Co = v_m \Delta t / \Delta y$ based on the mean velocity v_m in the cell and the cell size Δy was much less than unity. Regarding the spatial discretization of the equations, the third-order modified MUSCL scheme [131] was used to obtain the face fluxes whenever a cell was completely immersed in a single phase. When the cell was near the interface, the GEO-RECONSTRUCTION algorithm was used. The pressure corrections were computed with the bodyforce-weighted scheme, and the pressure-velocity coupling in a segregated solver was treated with the PISO method [132]. All the simulations were conducted with

$D = 30mm$, $H = 20mm$ and $R_0 = 1mm$.

It was noticed from experiments that the size of the drops generated is very sensitive to the interface meniscus. Also, we can see in figure 6.7, numerical simulation of the evolution of the interface for plan meniscus (left) and concave meniscus (right) with a produced droplet of $116\mu m$ and $126\mu m$ respectively. It is obvious that the meniscus form is an important parameter, therefore, the profile of the meniscus was modified to be as in the experiment.

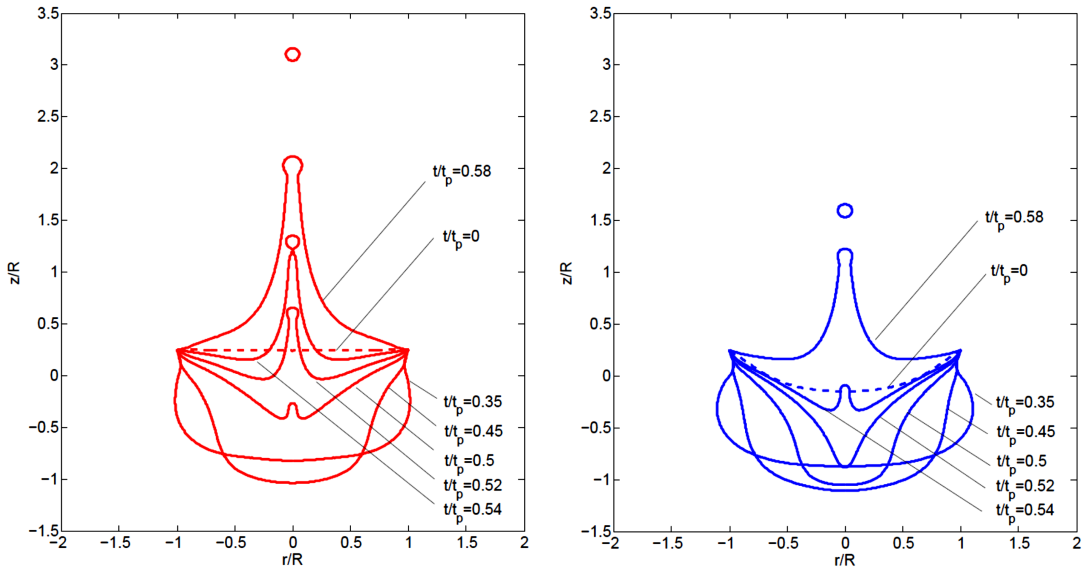

Figure 6.7: Simulation showing the influence of the initial meniscus form. At left (plane meniscus) and at right (concave meniscus).

6.4 Results and discussion

6.4.1 Experimental jetting process

In this study, a mixture of water+ 60% wt glycerol and Silicone oils of 5 and 10 cSt were used as working liquids. The physical properties are listed in table 5.1. The input pulse width were set to be $t_{pw} = 3$ and $4ms$.

Table 6.1: Physical properties of working liquids

Liquid	$\rho\ (kg/m^3)$	$\mu\ (cP)$	$\gamma\ (mN/m)$
water+ 60% wt glycerol mix. (5cSt)	1116	5	61.9
Silicone oil(5cSt)	912	4.2	21.9
Silicone oil(10cSt)	936	8.7	23.1

In each experiment, the sine pulse amplitude and width were introduced by LabView program. The input pulse and the measured displacement of the piston are illustrated in figure 6.8(a). While the corresponding velocity and pressure inside the reservoir are shown in figure 6.8(b). When the negative pulse is applied, the free surface of the meniscus is pulled back into the reservoir forming a cavity. Then, the piston moves into the other direction making a positive pressure a round the cavity. The cavity collapses forming a very thin jet smaller than the orifice. Finally, a drop as the same order of the jet separates and the meniscus returns back to the equilibrium. Figure 6.9 shows Experimental observation of the jetting process of silicone oil (10 cSt).

Experimental results shows that many parameters affect on the produced drop size. In figure 6.10 the effect of the pulse amplitude can be seen. Increasing the velocity amplitude of the piston makes the cavity collapse faster as the kinetic energy

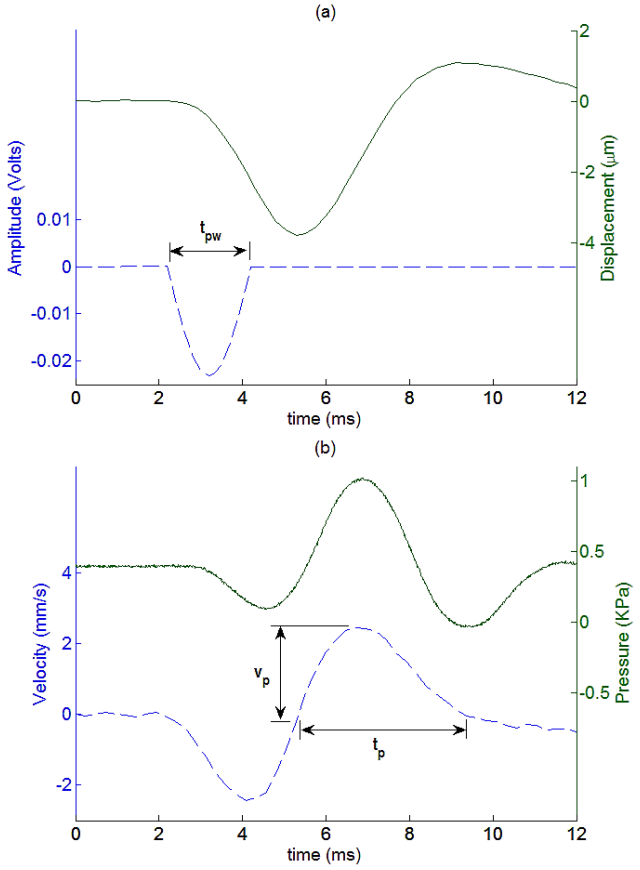

Figure 6.8: (a) The input pulse (dashed line) and the measured displacement of the piston (solid line). (b) The pressure inside the reservoir(solid line) and the velocity of the piston (dashed line).

that transfers to the fluid around the nozzle increases which leads to a thinner jet and a smaller droplet. Also, the speed of of the jet (and the drop) increase at faster collapse.

The introduced kinetic energy to the system does not affect only on the droplet size and it's speed, but also it characterizes the mode where only one droplet could be produced. Beside the piston velocity, there are other important parameters. At figure 6.11, we plot the generated drop diameter versus the velocity of the piston

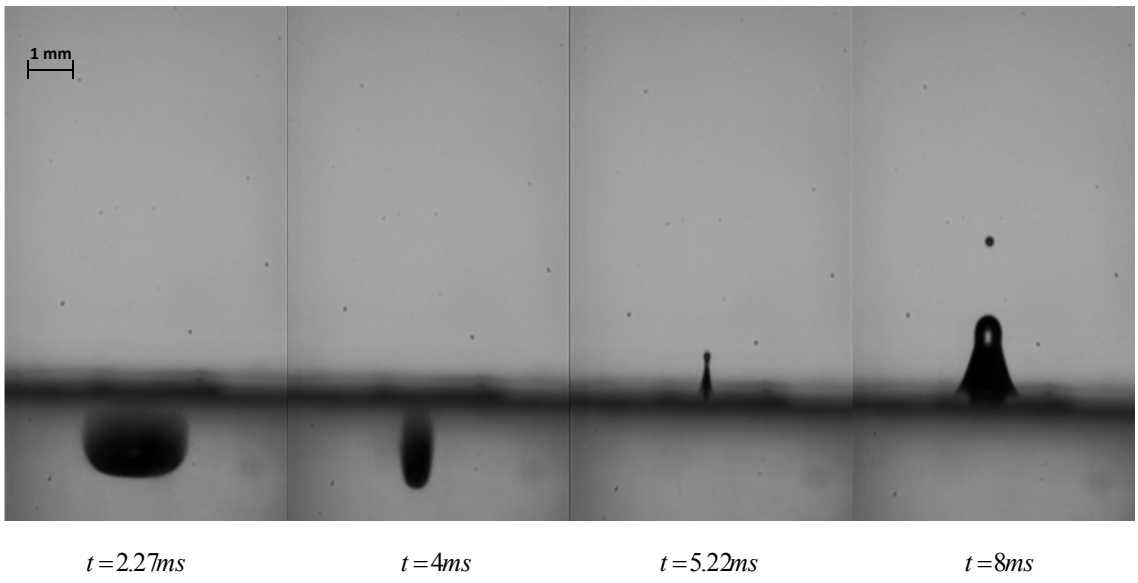

Figure 6.9: Jetting process of Silicone oil 10cSt from a 2 mm diameter nozzle

for various working liquids in order to study the effect of the velocity amplitude, pulse width and liquid properties on the final droplet size. And also to identify the range of velocity where we can produce only one droplet for each working liquid. It is obvious that the drop size decreases with the increasing of the velocity amplitude. After a certain amplitude, more than one drop are generated. A wider rang of drop size was achieved with lower viscosity. Also, it was observed that a lower surface tension helps to generate smaller drop. It was managed to generate a drop of silicon oil (5cSt) with a radius of $27\mu m$, being the surface tension $21.9mN/m$. Also it was noticed that the pulse width t_{pw} does not have a great influence if we have used the positive velocity amplitude v_p to be the piston velocity parameter.

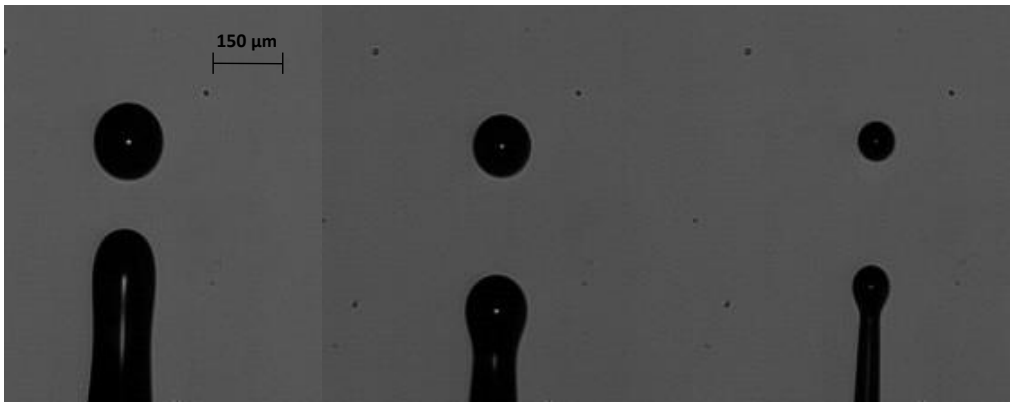

Figure 6.10: Images of Drops generated with different piston velocity

6.4.2 Numerical to experimental results

In our numerical model, we assumed that the reservoir has only one inlet/exit to the fluid which is the nozzle, while in the experiment we have also the syringe that is connected to the reservoir and exposed to the atmosphere. So, we assumed in the simulation that the volume of the formed cavity (V_{cavity}) is equal to the volume of liquid moved by the piston (V_{piston}), while in the experiment (V_{piston}) equal to (V_{cavity}) and the volume displaced inside the syringe. Also, in the simulation the nozzle is a rigid solid that does not deform and as it was mentioned before, the upper plate of the print-head prototype in the experiment has a thickness of $0.25mm$. So, there is a chance that the plate deforms with the movement of the piston. Therefore, to make sure that our model simulate the same condition of the experiment, we had compared (V_{piston}) with (V_{cavity}) of the experiment during the pulse period. V_{piston} was calculated by multiply the displacement of the piston by the area of the reservoir. While, V_{cavity} was measured by detecting the border of the cavity from the images using an image processing program (ImageJ).

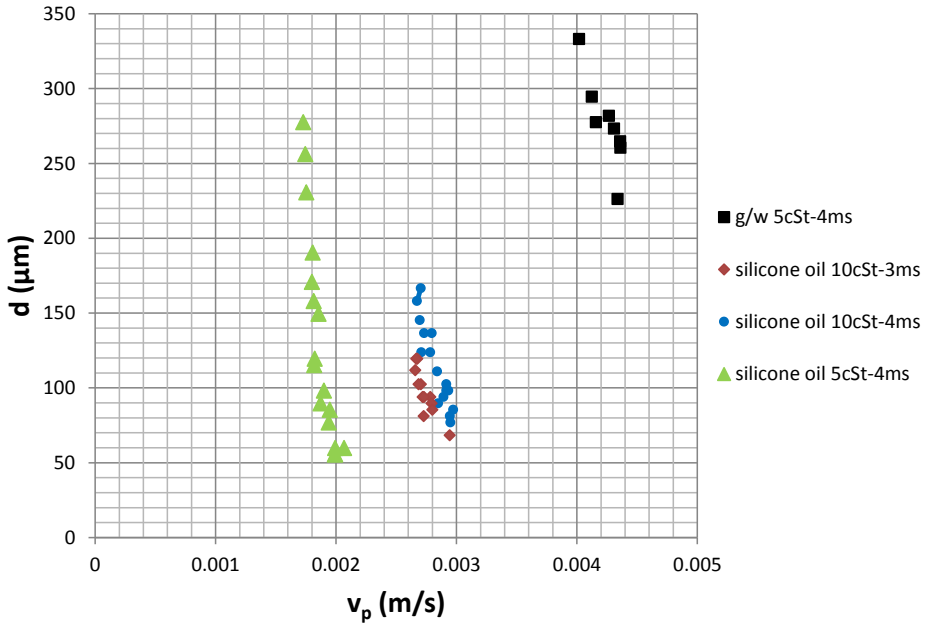

Figure 6.11: Drop size versus piston velocity with different governing parameters

It is clear from figure 6.12 that there is discrepancy between the volume of the cavity and the volume moved by the piston. So, if we have used in the simulation the same piston velocity that is in the experiment, we will have a higher kinetic energy around the nozzle. So, the droplet size in the simulation will be smaller than the one in the experiment.

The cavity volume in the experiment $\simeq 0.67V_{piston}$. So, depending on this result the piston velocity could be correlated in our simulation to give the same cavity volume as follow:

$$0.67V_{piston} = A \int v_p dt. \tag{6.1}$$

$$v_p = 0.67\frac{dh}{dt}. \tag{6.2}$$

being, A is the reservoir cross sectional area and h is the piston displacement.

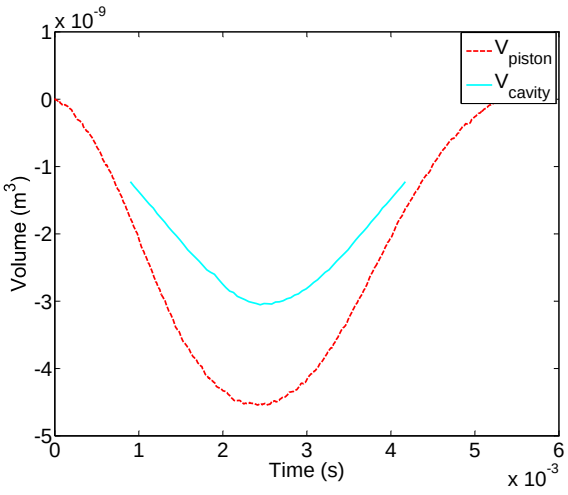

Figure 6.12: Comparison between (V_{piston}) and (V_{cavity})

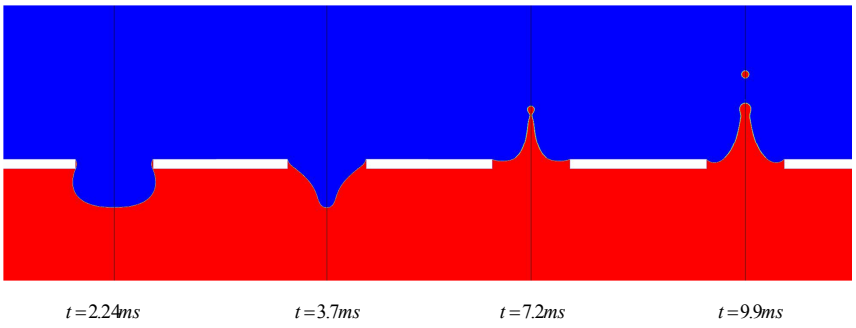

Figure 6.13: Numerical simulation of Jetting process for Silicone oil 10cSt at pressure amplitude 232 Pascal and pulse width 4 ms

Figure 6.13 shows numerical simulation of the jetting process of silicone oil (10cSt) at pressure amplitude 232 Pascal and pulse width 4 ms. The numerical

simulation has a good agreement with the experiment.

In figure 6.14, we plot experimental and numerical results of the droplet diameter front the velocity amplitude. The results illustrate the efficiency of our numerical model and the reliability of the piston velocity correlation.

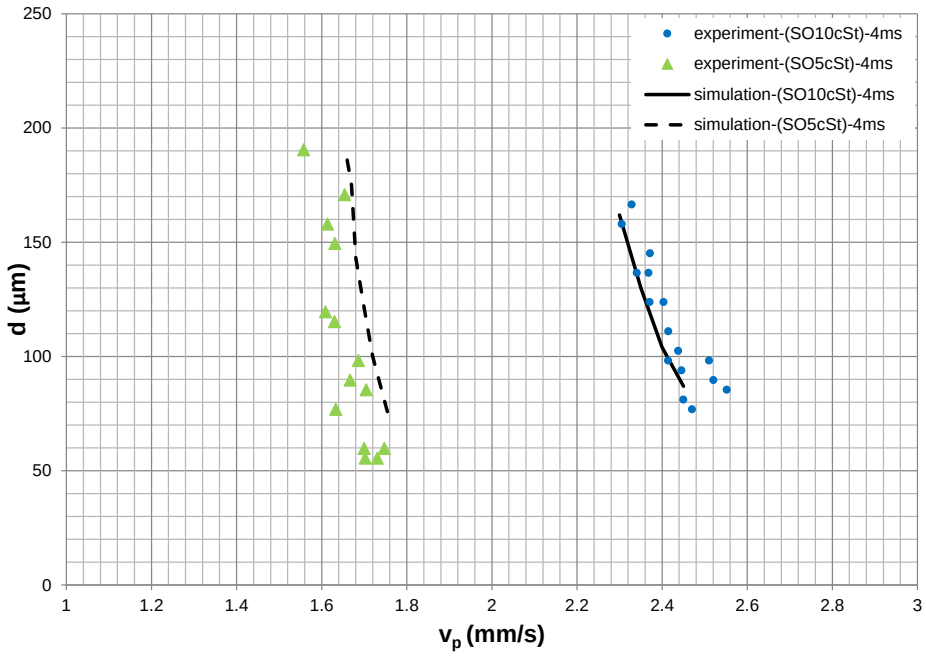

Figure 6.14: Comparison between experimental and numerical results

6.4.3 Scaling analysis

In this section, an analysis has been made to obtain scaling law for the drop size generated by (LS) print-head prototype. From the previous results we can say that the dimensionless droplet diameter is a function of the following dimensionless parameters,

$$\frac{d}{R_0} = f(v_p/v_c, oh, t_p/t_c, H/R_0, D/R_0), \quad \text{i.e.} \tag{6.3}$$

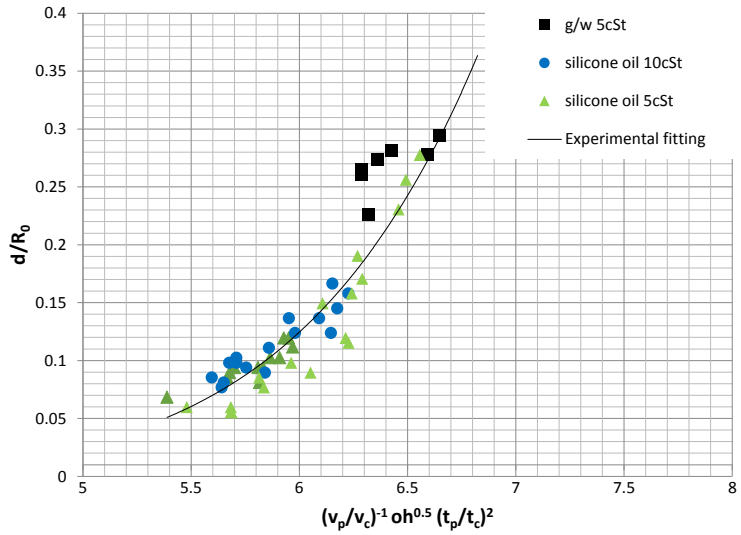

Figure 6.15: Dimensionless diameter of the drop d/R_0 versus the scaling groups $(v_p/v_c)^{-1}oh^{0.5}(t_p/t_c)^2$

Being, capillary velocity $v_c = (\sigma/\rho R_0)^{1/2}$, ohnesorge number $oh = \mu/\sqrt{\rho g R_0 \sigma}$ and capillary time $t_c = (\rho R_0^3/\sigma)^{1/2}$. In relation (6.3), beside positive velocity amplitude, liquid properties and geometrical parameters, we have introduced a new parameter which is (t_p) the width of the positive part in the velocity pulse (see figure 6.8(b)). Although we have seen in section (6.4.1) that the pulse width t_{pw} does not have significant effect on the droplet size, we found that t_p have a great influence. It was shown from the piston velocity measurement for each experimental point, that t_p is directly related to liquid properties as the positive part of the pulse is considered to be the system response to the negative applied part. Our numerical simulation showed that H and D do not have influence on the drop size which make sense as $H, D \ggg R_0$. So, H/R_0 and D/R_0 can be omitted and the relation (6.3) reduces to,

$$\frac{d}{R_0} \simeq f(v_p/v_c, oh, t_p/t_c) = f((v_p/v_c)^{-1}, oh^{0.5}, (t_p/t_c)^2), \quad \text{i.e.} \tag{6.4}$$

We have used the exponents illustrated in relation (6.4) in order to collapse all experimental series of data. Finally, the droplet size can be expressed in the following form,

$$d = C_1 R_0 \left((v_p/v_c)^{-1} oh^{0.5} (t_p/t_c)^2 \right)^{C_2} . \tag{6.5}$$

In figure 6.15 many experimental measurements are plotted for various t_p, working liquid silicone oil (5-10cSt) and 60% glycerol in water. The best fit within experimental uncertainty is reduced to $C_1 = 4e-8$ and $C_2 = 8$.

6.5 Conclusions

We report experimental and numerical results of the generation of drops significantly smaller than the nozzle from which they are generated. Briefly, the system consists of a cylindrical reservoir and two endplates. One plate is a thin metal sheet with a small orifice in the center, which acts as the nozzle. The other end consists of a piston which moves by the action of an electromechanical actuator which in turn is driven by simple pull-mode sine pulses. The meniscus (formed at the nozzle) is first overturned, forming a cavity. This cavity collapses and a thin and fast jet emerges from its center. Under appropriate conditions the tip of this jet breaks up to produce a single diminutive drop. A good agreement between the experimental and numerical results was found. Also, it was found that the initial interface meniscus profile is another parameter that could affect on the produced droplet size. Series of experiments have been carried out in order to study the effect that the pulse amplitude, pulse width and liquid properties have on the final droplet size. Based

on these experiments, a predictive scaling law for the droplet size has been obtained. The initial interface meniscus profile was the same at the numerical simulation and the experiments that have been carried out.

List of Figures

List of Tables

Bibliography

[1] M. M. Denn. Continuous drawing of liquids to form fibers. *Ann. Rev. Fluid Mech.*, 12:365–387, 1980.

[2] Saeid Vafaei and Dongsheng Wen. Bubble formation on a submerged micronozzle. *Colloid and Interface Science*, 343:291–297, 2010.

[3] C. S. Smith. On blowing bubbles for bragg's dynamic crystal model. *J. Appl. Phys.*, 20:631–632, 1949.

[4] A. M. Gañán-Calvo and J. M. Gordillo. Perfectly monodisperse microbubbling by capillary flow focusing. *Phys. Rev. Lett.*, 87:274501, 2001.

[5] A. M. Gañán-Calvo. Perfectly monodisperse microbubbling by capillary flow focusing: An alternate physical description and universal scaling. *Phys. Rev. E*, 69:027301, 2004.

[6] P. Garstecki, I. Gitlin, W. DiLuzio, G. M. Whitesides, E. Kumacheva, and H. A. Stone. Formation of monodisperse bubbles in a microfluidic flow-focusing device. *Appl. Phys. Lett.*, 85:2649–2651, 2004.

[7] T. Thorsen, R.W. Roberts, F. H. Arnold, and S. R. Quake. Dynamic pattern

formation in a vesicle-generating microfluidic device. *Phys. Rev. Lett.*, 86:4163, 2001.

[8] A. Gunther, S. A. Khan, M. Thalmann, F. Trachsel, and K. F. Jensen. Transport and reaction in microscale segmented gas–liquid flow. *Lab Chip*, 4:278, 2004.

[9] M. A. Herrada, A. M. Gañán-Calvo, and J. M. López-Herrera. Generation of small mono-disperse bubbles in axisymmetric t-junction: The role of swirl. *Phys. Fluids*, 23:072004, 2011.

[10] M. A. Herrada, A. M. Gañán-Calvo, and J. M. Montanero. Theoretical investigation of a technique to produce microbubbles by a microfluidic t junction. *Phys. Rev. E*, 88:033027, 2013.

[11] D. W. Moore. The velocity of rise of distorted gas bubbles in a liquid of small viscosity. *J. Fluid Mech.*, 23:749–766, 1965.

[12] P. C. Duineveld. Rise velocity and shape of bubbles in pure water at high reynolds number. *Journal of Fluid Mechanics*, 292:325–332, 1995.

[13] G. Mougin and J. Magnaudet. Path instability of a rising bubble. *Physical Review Letters*, 88:145021–145024, 2002.

[14] C. Martínez-Bazán, J. L. Montañés, and J. C. Lasheras. Statistical description of the bubble cloud resulting from the injection of air into a turbulent water jet. *International Journal of Multiphase Flow*, 28:597–615, 2002.

[15] Fumio Takemura and Akira Yabe. Gas dissolution process of spherical rising gas bubble. *Chemical Engineering Science*, 53(15):2691–2699, 1998.

[16] F. Takemura and A. Yabe. Rising speed and dissolution rate of a carbon dioxide bubble in slightly contaminated water. *Journal of Fluid Mechanics*, 378:319–334, 1999.

[17] D.F. McGinnis, J. Greinert, Y. Artemov, S.E. Beaubien, and A. Wüest. Fate of rising methane bubbles in stratified waters: How much methane reaches the atmosphere? *Journal of Geophysical Research C: Oceans*, 111:C09007, 2006.

[18] H. Ding, P. D. M. Spelt, and C. Shu. Diffuse interface model for incompressible two-phase flows with large density ratios. *Journal of Computational Physics*, 226:2078–2095, 2007.

[19] M.G. Gerritsen and L.J. Durlofsky. Modeling fluid flow in oil reservoirs. *Annual Review of Fluid Mechanics*, 37:211–238, 2005.

[20] A. Shokrollahi, M. Arabloo, F. Gharagheizi, and A.H. Mohammadi. Intelligent model for prediction of co2 - reservoir oil minimum miscibility pressure. *Fuel*, 112:375–384, 2013.

[21] V.L. Singleton and J.C. Little. Designing hypolimnetic aeration and oxygenation systems - a review. *Environmental Science and Technology*, 40:7512–7520, 2006.

[22] D.N. Rao and J.I. Lee. Determination of gas-oil miscibility conditions by interfacial tension measurements. *Journal of Colloid and Interface Science*, 262:474–482, 2003.

[23] A. M. Gañán-Calvo. Enhanced liquid atomization: From flow-focusing to flow-blurring. *Appl. Phys. Lett.*, 86:214101, 2005.

[24] J. Zeleny. Instability of electrified liquid surfaces. *Phys. Rev.*, 10:1–6, 1917.

[25] G. Taylor. Disintegration of water drops in electric field. *Proc. R. Soc. Lond. A*, 280:383–397, 1964.

[26] A. Watanabe, K. Higashitsuji, and K. Nishizawa. Studies on electrocapillary emulsification. *J. Colloid Interf. Sci.*, 64:278–289, 1978.

[27] M. Sato, M. Saito, and T. Hatori. Emulsification and size control of insulating and/or viscous liquids in liquid-liquid systems by electrostatic dispersion. *Journal of Colloid And Interface Science*, 156(2):504–507, 1993.

[28] C. Tsouris, D. W. DePaoli, J. Q. Feng, 0. A. Basaran, and T. C. Scott. Electrostatic spraying of nonconductive fluids into conductive fluids. *AIChE J.*, 40:1920–1923, 1994.

[29] Masayuki Sato, Toshihiro Hatori, and Masahiro Saito. Experimental investigation of droplet formation mechanisms by electrostatic dispersion in a liquid–liquid system. *IEEE Transactions on Industrial Applications*, 33:1527–1534, 1997.

[30] Costas Tsouris, Won-Tae Shin, and Sotira Yiacoumi. Pumping, spraying, and mixing of fluids by electric fields. *The Canadian Journal of Chemical Eng.*, 76:589–599, 1998.

[31] G. Gneist and H.-J. Bart. Electrostatic drop formation in liquid/liquid systems. *Chemical Engineering and Technology*, 25:899–904, 2002.

[32] J. M. Grace and J. C. M. Marijnissen. A review of liquid atomization by electrical means. *J. Aerosol Sci.*, 25(6):1005–1019, 1994.

[33] M. Doring. Ink-jet printing. *Philips Tech. Rev.*, 40:192, 1982.

[34] B. Nivi B. A. Ridley and J. M. Jacobson. All-inorganic field effect transistors fabricated by printing. *Science*, 286:746, 1999.

[35] T. P. Theriault K. Konrad E. Lachenmeier M. Schena, R. A. Heller and R. W. Davis. Microarrays: Biotechnology's discovery platform for functional genomics. *Trends Biotechnol*, 16:301, 1998.

[36] S. I. Zoltan. Pulsed droplet ejection system. *U. S. Patent No. 3,683,212*, 1972.

[37] E. L. Kyser and S. B. Sears. Method and apparatus for recording with writing fluids and drop projection means therefore. *U. S. Patent No. 3,946,398*, 1976.

[38] K. Noboru Kobayashi, H. and S. Ohno. Liquid recording medium. *U. S. Patent No. 4,243,994*.

[39] F. L. Cloutier D. K. Donald J. D. Meyer C. A. Tacklind Vaught, J. L. and H. H. Taub. Thermal ink jet printer. *U. S. Patent No. 4,490,728*, 1984.

[40] A. M. Gañán-Calvo and J. M. Montanero. Revision of capillary cone-jet physics: Electrospray and flow focusing. *Phys. Rev. E*, 79:066305, 2009.

[41] S. Goren and M. Gottlieb. Surface-tension-driven breakup of viscoelastic liquid threads. *J . Fluid Mech.*, 120:245–266, 1982.

[42] A.-C. Ruo, F. Chen, C.-A. Chung, and M.-H. Chang. Three-dimensional response of unrelaxed tension to instability of viscoelastic jets. *J . Fluid Mech.*, 682:558–576, 2011.

[43] C. Clasen, J. Bico, V. M. Entov, and G. H. McKinley. ?gobbling drops?: the jetting-dripping transition in flows of polymer solutions. *J. Fluid Mech*, 636:5–40, 2009.

[44] J. G. Oldroyd. On the formulation of rheological equations of state. *Proc. Roy. Soc. Lond.*, 200:523–541, 1950.

[45] D. F. James. Boger fluids. *Annu. Rev. Fluid Mech.*, 41:129–142, 2009.

[46] L.-J. Yang, M.-X. Tong, and Q.-F. Fu. Instability of viscoelastic annular liquid sheets subjected to unrelaxed axial elastic tension. *J. Non-Newtonian Fluid Mech.*, 198:31–38, 2013.

[47] P. Huerre and P. A. Monkewitz. Local and global instabilites in spatially developing flows. *Annu. Rev. Fluid Mech.*, 22:473–537, 1990.

[48] J. M. Montanero and A. M. Gañán-Calvo. Viscoelastic effects on the jetting-dripping transition in co-flowing capillary jets. *J. Fluid Mech.*, 610:249–260, 2008.

[49] F. Li, A. M. Gañán-Calvo, J. M. López-Herrera, X.-Y. Yin, and X.-Z. Yin. Absolute and convective instability of a charged viscoelastic liquid jet. *J. Non-Newtonian Fluid Mech.*, 196:58–69, 2013.

[50] S. Middlema. Stability of a viscoelastic jet. *Chem. Eng. Sci.*, 20:1037–1040, 1965.

[51] Z. Liu and Z. Liu. Linear analysis of three-dimensional instability of non-newtonian liquid jets. *J. Fluid Mech.*, 559:451–459, 2006.

[52] M. Goldin, J. Yerushalmi, R. Pfeffer, and R. Shinnar. Breakup of a laminar capillary jet of a viscoelastic fluid. *J. Fluid Mech.*, 38:689–711, 1969.

[53] J. Eggers and E. Villermaux. Physics of liquid jets. *Rep. Prog. Phys.*, 71:036601, 2008.

[54] D. D. Joseph. *Fluid dynamics of viscoelastic liquids*. Springer-Verlag, 1990.

[55] M. R. Khorrami, M. R. Malik, and R. L. Ash. Application of spectral collocation techniques to the stability of swirling flows. *J. Comput. Phys.*, 81:206–229, 1989.

[56] R. J. Briggs. *Electron-Stream Interaction with Plasmas*. MIT Press, Cambridge, 1964.

[57] M. R. Khorrami. Chebyshev spectral collocation method using a staggered grid for the stability of cylindrical flows. *Int. J. Numer. Methods Fluids*, 12:825–833, 1991.

[58] M. Gaster. A note on the relation between temporally-increasing and spatially-increasing disturbances in hydrodynamic stability. *J. Fluid Mech.*, 14:222–224, 1962.

[59] S. J. Leib and M. E. Goldstein. Convective and absolute instability of a viscous liquid jet. *Phys. Fluids*, 29:952–954, 1986.

[60] M. A. Herrada, J. M. Montanero, C. Ferrera, and A. M. Gañán-Calvo. Analysis of the dripping-jetting transition in compound capillary jets. *J. Fluid Mech.*, 649:523–536, 2010.

[61] S. J. Gill and J. Gavis. Tensile stress in jets of viscoelastic fluids. I. *J. Polym. Sci.*, 20:287–298, 1956.

[62] P. Guillot, A. Colin, A. S. Utada, and A. Ajdari. Stability of a jet in confined pressure-driven biphasic flows at low Reynolds numbers. *Phys. Rev. Lett.*, 99:104502, 2007.

[63] T. Si, F. Li, X.-Y. Yin, and X.-Z. Yin. Modes in flow focusing and instability of coaxial liquid-gas jets. *J. Fluid Mech.*, 629:1–23, 2009.

[64] E. J. Vega, J. M. Montanero, M. A. Herrada, and A. M. Gañán-Calvo. Global and local instability of flow focusing: The influence of the geometry. *Phys. Fluids*, 22:064105, 2010.

[65] L. Rayleigh. On the instability of jets. *Proc. London Math. Soc.*, s1-10:4–13, 1878.

[66] A. M. Gañán-Calvo, J. M. Montanero, L. Martín-Banderas, and M. Flores-Mosquera. Building functional materials for health care and pharmacy from microfluidic principles and Flow Focusing. *Adv. Drug Delivery Rev.*, 65:1447–1469, 2013.

[67] J. Rosell-Llompart and A. M. Gañán-Calvo. Turbulence in pneumatic flow focusing and flow blurring regimes. *Phys. Rev. E*, 77:036321, 2008.

[68] M. Brinkmann and R. Lipowsky. Wetting morphologies on substrates with striped surface domains. *J. Appl. Phys.*, 92:4296, 2002.

[69] G. W. Young and S. H. Davis. Rivulet instabilities. *J. Fluid Mech.*, 176:1–31, 1987.

[70] S. H. Davis. Moving contact lines and rivulet instabilities. Part 1. The static rivulet. *J. Fluid Mech.*, 98:225–242, 1980.

[71] R. A. Brown and L. E. Scriven. On the multiple equilibrium shapes and stability of an interface pinned on a slot. *J. Colloid Interface Sci.*, 78:528–542, 1980.

[72] H. Gau, S. Herminghaus, P. Lenz, and R. Lipowsky. Liquid morphologies on structured surfaces: from microchannels to microchips. *Science*, 283:46–49, 1999.

[73] R. V. Roy and L. W. Schwartz. On the stability of liquid ridges. *J. Fluid Mech.*, 391:293–318, 1999.

[74] C. Perazzo and J. Gratton. Navier-Stokes solutions for parallel flow in rivulets on an inclined plane. *J. Fluid Mech.*, 507:367–379, 2004.

[75] C. Paterson, S. K. Wilson, and B. R. Duffy. Pinning, de-pinning and re-pinning of a slowly varying rivulet. *Eur. J. Mech./Fluids*, 41:94–108, 2013.

[76] J. M. Sullivan, C. Paterson, S. K. Wilson, and B. R. Duffy. A thin rivulet or ridge subject to a uniform transverse shear stress at its free surface due to an external airflow. *Phys. Fluids*, 24:082109, 2012.

[77] S. Mechkov, M. Rauscher, and S. Dietrich. Stability of liquid ridges on chemical micro- and nanostripes. *Phys. Rev. E*, 77:061605, 2008.

[78] E. S. Benilov. On the stability of shallow rivulets. *J. Fluid Mech.*, 636:455–474, 2009.

[79] R. H. Weiland and S. H. Davis. Moving contact lines and rivulet instabilities. Part 2. Long waves on flat rivulets. *J. Fluid Mech.*, 107:261–280, 1981.

[80] J. Koplik, T. S. Lo, M. Rauscher, and S. Dietrich. Pearling instability of nanoscale fluid flow confined to a chemical channel. *Phys. Fluids*, 18:032104, 2006.

[81] J. A. Diez, A. G. González, and L. Kondic. On the breakup of fluid rivulets. *Phys. Fluids*, 21:082105, 2009.

[82] P. Schmuki and M. Laso. On the stability of rivulet flow. *J. Fluid Mech.*, 215:125–143, 1990.

[83] T. G. Myers, H. X. Liang, and B. Wetton. The stability and flow of a rivulet driven by interfacial shear andgravity. *Int. J. Non-Linear Mech.*, 39:1239–1249, 2004.

[84] H. H. Saber and M. S. El-Genk. On the breakup of a thin liquid film subject to interfacial shear. *J. Fluid Mech.*, 500:113–133, 2004.

[85] S. K. Wilson and B. R. Duffy. When is it energetically favorable for a rivulet of perfectly wetting fluid to split? *Phys. Fluids*, 17:078104, 2005.

[86] S. K. Wilson, J. M. Sullivan, and B. R. Duffy. The energetics of the breakup of a sheet and of a rivulet on a vertical substrate in the presence of a uniform surface shear stress. *J. Fluid Mech.*, 674:281–306, 2011.

[87] J. A. Nicolás and J. M. Vega. Linear oscillations of axisymmetric viscous liquid bridges. *Z. angew. Math. Phys.*, 51:701–731, 2000.

[88] J. M. Montanero. Linear dynamics of axisymmetric liquid bridges. *Eur. J. Mech. B. Fluids*, 22:167–178, 2003.

[89] J. O. Hinze. *Turbulence*. McGraw-Hill, New York, USA, 1975.

[90] T. Cubaud and C.-M. Ho. Transport of bubbles in square microchannels. *Phys. Fluids*, 16:4575–4585, 2004.

[91] Chain-Nan Yung and Kenneth J De Witt. A numerical study of parameters affecting gas bubble dissolution. *Journal of Colloid and Interface Science*, 127:442–452, 1988.

[92] J.M.Lopez, F. Marques, and J. Shen. An eficient spectral-projection method for the navier-stokes equations in cylindrical geometries ii. three dimensional cases. *J. Comput. Phys.*, 176:401, 2002.

[93] R. E. Lynch, J. R. Rice, and D. H. Thomas. Direct solution of partial differential equations by tensor product methods. *Numer. Math.*, 6:85, 1964.

[94] C. Canuto, M.Y. Hussaini, A. Quarteroni, and T.A. Zang. *Spectral methods in fluid dynamics.* Springer-Verlag., 1988.

[95] P. Chang and C.R. Wilke. Some measurements of diffusion in liquids. *The Journal of Physical Chemistry*, 59(7):592–596, 1955.

[96] John M. Prausnitz Robert C. Reid and Thomas K. Sherwood. The properties of gases and liquids. *AIChE Journal*, 24:1142, 1978.

[97] J.B. Fenn, M. Mann, C.K. Meng, S.F. Wong, and C.M. Whitehouse. Electrospray ionization for mass spectrometry of large biomolecules. *Science*, 246(4926):64–71, 1989.

[98] A. Barrero, J.M. López-Herrera, A. Boucard, I.G. Loscertales, and M. Márquez. Steady cone-jet electrosprays in liquid insulator baths. *J. Colloid Interf. Sci.*, 272:104–108, 2004.

[99] A. Jaworek. Electrostatic micro- and nanoencapsulation and electroemulsification: A brief review. *Journal of Microencapsulation*, 25(7):443–468, 2008.

[100] A.G. Marin, I.G. Loscertales, and A. Barrero. Surface tension effects on submerged electrosprays. *Biomicrofluidics*, 6(4), 2012.

[101] T.P. Forbes. Rapid detection and isotopic measurement of discrete inorganic samples using acoustically actuated droplet ejection and extractive electrospray ionization mass spectrometry. *Rapid Communications in Mass Spectrometry*, 29(1):19–28, 2014.

[102] S. Coppola, V. Vespini, F. Merola, M. Paturzo, L. Miccio, O. Gennari, S. Grilli, and P. Ferraro. Electrohydrodynamic dispenser for delivering multiphase samples at nanoscale. *Springer Series in Surface Sciences*, 56:251–276, 2015.

[103] C. Ferrera, J. M. Lṕez-Herrera, M. A. Herrada, J. M. Montanero, and A. J. Acero. Dynamical behavior of electrified pendant drops. *Phys. Fluids*, 25:012104, 2013.

[104] L. Oddershede and S. R. Nagel. Singularity during the onset of an electrohydrodynamic spout. *Phys. Rev. Lett.*, 85:1234–1237, 2000.

[105] D. Duft, T. Achtzehn, R. M?ller, B. A. Huber, and T. Leisner. Coulomb fission: Rayleigh jets from levitated microdroplets. *Nature*, 421:128, 2003.

[106] U. Stachewicz, J. F. Dijksman, C. U. Yurteri, and J. C. Marijnissen. Experiments on single event electrospraying. *Appl. Phys. Lett.*, 91:254109, 2007.

[107] M. D. Paine. Transient electrospray behaviour following high voltage switching. *Microfluid Nanofluid*, 6:775–783, 2009.

[108] R.t T. Collins, K. Sambath, M. T. Harris, and O. A. Basaran. Universal scaling laws for the disintegration of electrified drops. *PNAS*, 110:4905–4910, 2013.

[109] A. M. Gañán-Calvo, J. M. López-Herrera, N. Rebollo-Muñoz, and J. M. Montanero. Electrical disintegration of liquid drops: universal scaling law for the size of ejecta from experimental, dimensional and numerical analysis. Subbmitted to PNAS, 2015.

[110] Osman A Basaran and L.E Scriven. Axisymmetric shapes and stability of pendant and sessile drops in an electric field. *Journal of Colloid and Interface Science*, 140(1):10 – 30, 1990.

[111] N. Dubash and A. J. Mestel. Behaviour of a conducting drop in a highly viscous fluid subject to an electric field. *Journal of Fluid Mechanics*, 581:469 – 493, 2007.

[112] R.B. Karyappa, S.D. Deshmukh, and R.M. Thaokar. Breakup of a conducting drop in a uniform electric field. *Journal of Fluid Mechanics*, 754(3):550–589, 2014.

[113] J. M. López-Herrera, S. Popinet, and M. A. Herrada. A charge-conservative

approach for simulating electrohydrodynamic two-phase flows using volume-of-fluid. *J. Comput. Phys.*, 230:1939–1955, 2011.

[114] S. Popinet. The Gerris flow solver. http://gfs.sourceforge.net.

[115] M. A. Herrada, J. M. López-Herrera, A. M. Gañán-Calvo, E. J. Vega, J. M. Montanero, and S. Popinet. Numerical simulation of electrospray in the cone-jet mode. *Phys. Rev. E*, 86:026305, 2012.

[116] J. M. López-Herrera, P. Riesco-Chueca, and A. M. Gañán-Calvo. Linear stability analysis of axisymmetric perturbations in imperfectly conducting liquid jets. *Phys. Fluids*, 17:034106, 2005.

[117] E. J. Vega, J. M. Montanero, and C. Ferrera. Exploring the precision of backlight optical imaging in microfluidics close to the diffraction limit. *Measurement*, 44:1300–1311, 2011.

[118] J. M. Montanero, C. Ferrera, and V. M. Shevtsova. Experimental study of the free surface deformation due to thermal convection in liquid bridges. *Exp. Fluids*, 45:1087–1101, 2008.

[119] Patrick K. Notz and Osman A. Basaran. Dynamics of drop formation in an electric field. *Journal of Colloid and Interface Science*, 213(1):218 – 237, 1999.

[120] A. J. Acero, C. Ferrera, J. M. Montanero, M. A. Herrada, and J. M. López-Herrera. Experimental analysis of the evolution of an electrified drop following high voltage switching. *Eur. J. Mech./Fluids*, 38:58–64, 2013.

[121] R. T. Collins, J. J. Jones, M. T. Harris, and O. A. Basaran. Electrohydrody-

namic tip streaming and emission of charged drops from liquid cones. *Nature Phys.*, 4:149–154, 2008.

[122] Y. Kawana J. Kimura and T. Kuriyama. An immobilized enzyme membrane fabrication method using an ink jet nozzle. *Biosensors*, 4:41, 1988.

[123] W. J. Lloyd and H. H. Taub. Ink jet printing. *Output Hardcopy Devices*, Chap. 13:p. 311, 1988.

[124] G. A. Howell D. J. Hayes G. L. Bernardini, B. A. Rampy and C. J.Frederickson. Applications of piezoelectric fluid jetting devices to neuroscience research. *J. Neurosci. Methods*, 38:81, 1991.

[125] T. M. Brennan. Method and apparatus for conducting an array of chemical reactions on a support surface. *U.S. Patent No. 5,474,796*, 1995.

[126] O. Br D. Sziele.

[127] H. P. Le. Progress and trends in ink-jet printing technology. *J. Imaging Sci. Technol*, 42:49, 1998.

[128] F. L. Degertekin G. Perçin, A. Atalar and B. T. Khuri-Yakub. Micromachined two-dimensional array piezoelectrically actuated transducers. *Appl. Phys*, 72:1397, 1998.

[129] Alvin U. Chen and Osman A. Basaran. A new method for significantly reducing drop radius without reducing nozzle radius in drop-on-demand drop production. *Physics of fluids*, 14:1, 2001.

[130] A. A. Castrejón-Pita, J. R. Castrejón-Pita, and G. D. Martin. A novel method to produce small droplets from large nozzles. *Review of Scientific Instruments*, 83:115105, 2012.

[131] R. I. Issa. Solution of the implicitly discretised fluid flow equations by operator-splitting. *Journal of Computational Physics*, 62:40–65, 1986.

[132] B. V. Leer. Towards the ultimate conservative difference scheme. v - a second-order sequel to godunov's method. *Journal of Computational Physics*, 32:101–136, 1979.